NEUTRONIC ANALYSIS OF STOCHASTIC DISTRIBUTION OF FUEL PARTICLES IN VERY HIGH TEMPERATURE GAS-COOLED REACTORS

by

Wei Ji

A dissertation submitted in partial fulfillment
of the requirements for the degree of
Doctor of Philosophy
(Nuclear Engineering and Radiological Sciences)
in The University of Michigan
2008

Doctoral Committee:

Professor William R. Martin, Chair
Emeritus Professor Ziyaeddin A. Akcasu
Professor Iain D. Boyd
Professor James Paul Holloway
Professor Edward W. Larsen

Dedication

To Mom and Dad

Acknowledgements

Table of Contents

List of Tables

Abstract

The Very High Temperature Gas-Cooled Reactor (VHTR) is a promising
candidate for Generation IV designs due to its inherent safety, efficiency, and its
proliferation-resistant and waste minimizing fuel cycle. A number of these advantages
stem from its unique fuel design, consisting of a stochastic mixture of tiny (0.78mm
diameter) microspheres with multiple coatings. However, the microsphere fuel regions
represent point absorbers for resonance energy neutrons, resulting in the "double
heterogeneity" for particle fuel. Special care must be taken to analyze this fuel in order to
predict the spatial and spectral dependence of the neutron population in a steady-state
reactor configuration. The challenges are considerable and resist brute force computation:
there are over 10^{10} microspheres in a typical reactor configuration, with no hope of
identifying individual microspheres in this stochastic mixture. Moreover, when individual
microspheres "deplete" (e.g., burn the fissile isotope U-235 or transmute the fertile
isotope U-238 (eventually) to Pu-239), the stochastic time-dependent nature of the
depletion compounds the difficulty posed by the stochastic spatial mixture of the fuel,
resulting in a prohibitive computational challenge. The goal of this research is to develop
a methodology to analyze particle fuel randomly distributed in the reactor, accounting for
the kernel absorptions as well as the stochastic depletion of the fuel mixture.

This Ph.D. dissertation will address these challenges by developing a
methodology for analyzing particle fuel that will be accurate enough to properly model

stochastic particle fuel in both static and time-dependent configurations and yet be efficient enough to be used for routine analyses. This effort includes creation of a new physical model, development of a simulation algorithm, and application to real reactor configurations.

CHAPTER 1

Introduction

1.1 VHTR Concept and Its Design and Development

The Very High Temperature Gas-cooled Reactor (VHTR) concept was proposed first by General Atomics based on its Gas Turbine-Modular Helium Reactor (GT-MHR) design. It was submitted to the Generation IV Roadmap technical group for consideration and accepted as the representative high-temperature gas-cooled reactor concept. The Generation IV Roadmap project aims at designing and developing reactor system concepts for producing electricity and meeting the goals of improved economics, passive safety, sustainability, proliferation resistance, and physical security. [1,2] The VHTR is a design that fulfills these requirements.

1.1.1 NGNP designs

Recently, in order to meet the global growing demands for electric power and transportation fuels, many countries have turned to nuclear power for producing both electricity and hydrogen without the consumption of fossil fuels. In the United States, the Department of Energy (DOE) has launched a new project, the Next Generation Nuclear Plant (NGNP) project, to demonstrate emissions-free nuclear-assisted electricity and hydrogen production by 2015 [2]. Because of excellent characteristics such as a core outlet coolant temperature of 1000 °C, inherent passive safety, and a total power output

consistent with that expected for commercial high-temperature gas-cooled reactors, the VHTR system was selected by DOE for the NGNP project.

The dissertation will address the neutronic analysis for the VHTR.

1.1.2 Prismatic and pebble-bed designs

There are two types of NGNP designs that are based on the VHTR concept: the prismatic fuel type and the pebble-bed fuel type. Both designs use Tristructural-isotropic (TRISO) fuel, which consists of coated microsphere fuel particles. The TRISO fuel particles, up to about 1mm in diameter, consist of a fuel kernel and four coating layers which prevent the leakage of fission products and provide structural integrity. These fuel particles are randomly distributed in the fuel compact for the prismatic design or in the fuel pebble for the pebble-bed design.

Figure 1.1 shows the fuel configurations at different dimensional levels in a typical prismatic reactor core. The TRISO fuel particles are manufactured and consolidated into graphite matrix powders. Under high pressure and high temperature, they are resin molded and carburized to form cylindrical fuel compacts about 5.08cm high. Fuel compacts are then inserted into hexagonal fuel blocks comprised of coolant holes and fuel compact holes. Each fuel block is 79.3cm high. The full core consists of 1020 fuel blocks, which are arranged in three annular fuel rings that are ten blocks high. The inner and outer reflector regions adjacent to the fuel blocks are hexagonal graphite blocks. In addition, single layers of reflector blocks comprise the top and bottom reflectors. Figure 1.2 shows an early version of the pebble-bed reactor design. It is a cylindrical core filled with two types of pebbles: graphite (moderator) pebbles and fuel pebbles with a specified moderator/fuel ratio. In the NGNP design for the pebble-bed

reactor, the core is an annular core, as with the prismatic design, and there is an inner solid reflector. Both the fuel and graphite pebbles have typical diameters of 6cm and are randomly mixed in the full core. Each fuel pebble consists of a spherical fuel zone with radius 2.5cm and an outer graphite shell with thickness 0.5cm. TRISO fuel particles are randomly distributed inside the fuel zone in the fuel pebbles. Such a design allows the pebbles to be dropped in at the top and removed at the bottom, providing a continuous online refueling mechanism. This is a unique advantage of the pebble bed design.
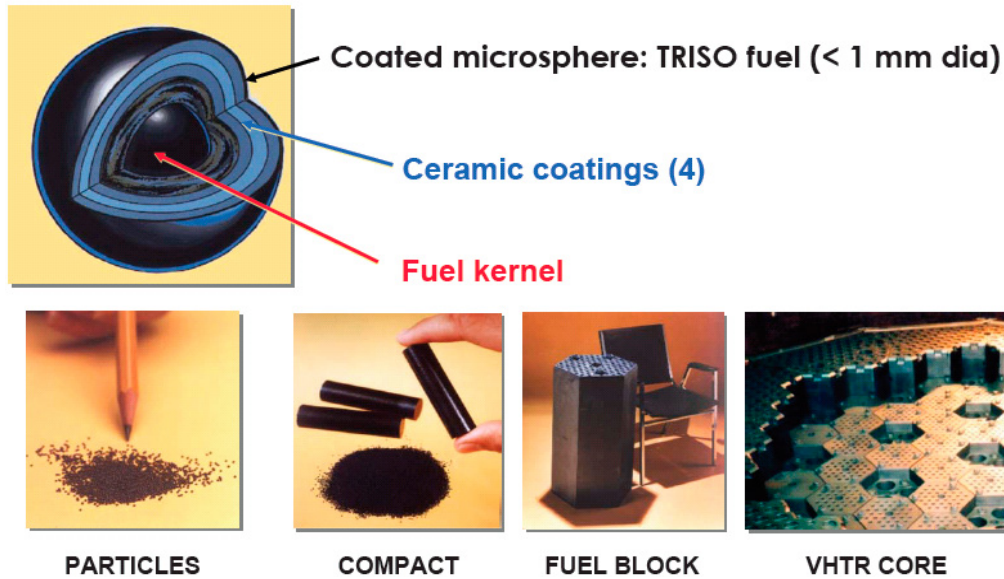
Figure 1.1 Prismatic design

Figure 1.2 Pebble-bed design

A more detailed description of the NGNP designs for the VHTR can be found in the Idaho National Engineering and Environmental Laboratory (INEEL) "NGNP Point Design" report [2].

1.2 Methods for Analysis of Gas-cooled Reactors

In the design of nuclear reactors, a neutronic analysis is needed to determine and optimize physics quantities such as reactivity, the spatial distribution of power and temperature, decay heat, depletion, and fuel burn-up. Many general routine analysis methods have been developed for obtaining these quantities in the past half century. [3,40,41,43] These include several classical approximation methods in solving the Boltzmann transport equation, such as multi-group diffusion theory, the S_n method, P_n/B_n approximations, collision probability methods, and the method of characteristics. Also, there are many classical approximations for treating resonance absorption in the spectrum

calculation, such as the narrow resonance approximation (NR), the narrow-resonance infinite-mass approximation (NRIM), and the intermediate resonance approximation (IR). In addition, there are a number of techniques and methods for treating a heterogeneous cell by transforming it into an equivalent homogenized cell, such as equivalence theory and energy-dependent self-shielding factors (i.e., disadvantage factors) [3,41]. Moreover, as alternative to deterministic methods, the Monte Carlo method has been used but has not gained wide use in practice due to its extensive computational time.

Most of these conventional methods used in the neutronic analysis for gas-cooled reactors were developed in the early years of gas-cooled reactor development. In general, reasonably good results were obtained. However, due to the unique design of the gas-cooled reactor with TRISO fuel, substantial challenges exist for traditional methods if more accurate predictions of neutronic behavior are needed, such as needed to analyze the "deep burn" concept that involves additional complexities in the fuel design [88].

1.2.1 Challenges for VHTR system analysis

In VHTR systems, the microsphere fuel particles represent effective point absorbers for resonance energy neutrons, combining with the usual fuel rod or fuel pebble heterogeneity to yield the "double heterogeneity" for particle fuel. Special care must be taken to analyze this fuel in order to predict the spatial and spectral dependence of the neutron population in a steady-state reactor configuration. The challenges are considerable and resist brute force computation: there are over 10^{10} microspheres in a typical reactor configuration, with no hope of identifying individual microspheres in this stochastic mixture. Moreover, when individual microspheres "deplete" (e.g., burn the fissile isotope U-235 or transmute the fertile isotope U-238 (eventually) to Pu-239), the

stochastic time-dependent nature of the depletion compounds the difficulty posed by the stochastic spatial mixture of the fuel, resulting in a prohibitive computational challenge.

The essential challenge consists in developing a methodology that can accurately and efficiently analyze the double heterogeneity configuration and predict the neutronic properties at both the microscopic and macroscopic levels in the global neutronic computation, as well as accounting for the nature of the stochastic distribution in the VHTR design.

1.2.2 Traditional methods for analysis of gas-cooled reactors

From a historical point of view, gas-cooled reactors appeared very early and are not a novel design. As early as about 1956, a prismatic design and a pebble-bed design were studied separately in the UK and Germany. Later from 1966 to 1968, the DRAGON reactor at Winfrith, the Peach Bottom reactor near Philadelphia, and the AVR pebble-bed reactor at Jülich were constructed and operated successfully. This experience led to the construction of the commercially operated high temperature gas-cooled reactor (HTGR) built by General Atomics (GA) at Fort St. Vrain in the U.S. and the THTR pebble bed reactor in Germany [3]. Nowadays, the technologies for gas-cooled reactors are being advanced in the GA Gas Turbine-Modular Helium Reactor (GT-MHR) Project and the South African Pebble Bed Modular Reactor (PBMR) Project, as well as the two currently operated experimental reactors: the Japanese HTTR and the Chinese HTR-10.

In the U.S., the design and development of gas-cooled reactors pushed the development of reactor analysis codes to predict the neutronic properties in a doubly heterogeneous system. Many conventional methodologies were investigated and used in these codes, as mentioned in the preceding section. The essential idea among these

methods was development of an efficient way to calculate the shielded group constants in doubly heterogeneous cells accounting for resonance absorption. These group constants were then used for the full core global calculation with homogenized fuel assemblies.

Two major methods were developed at Los Alamos [4]. The first method was a two-step method consisting of first applying Wälti's [5] grain shielding factor calculation to correct point-wise cross sections, and then applying Levine's [6] fuel pin cell space shielding computation to generate collapsed grain-shielded fine-group cross sections. In Wälti's method, the self-shielding factors were calculated in a fine-group structure for a two-region microscopic cell consisting of the fuel kernel and a homogenized region consisting of the coating regions and the graphite matrix, employing a method used by Sauer [7] for fuel lattice calculations. An earlier but more accurate method, the Nordheim integral method (NIH) [8], was used to calculate fine-group constants for a grain cell but was more time-consuming compared to Wälti's method. In Levine's method, equivalence theory was used to treat the fuel compact heterogeneity.

The second method to calculate group constants for a doubly heterogeneous cell utilized collision probabilities and rational approximations for escape probabilities and collision probabilities, resulting in an equivalence relation while accounting for both levels of heterogeneity for the generation of fine-group cross sections. This method avoids the time-consuming grain-shielding process and involves only one step to go from a doubly heterogeneous cell to an equivalent homogeneous cell.

Before these two methods were developed, similar methods had been implemented in the General Atomics MICROX code, [3] which uses the collision probability method to solve the neutron slowing down and thermalization equations in

200 energy groups for a two-region lattice cell. The fluxes in the two regions are coupled by collision probabilities computed with the flat flux approximation. The grain structure of the fuel particle is accounted for with the method developed by Wälti [5]. A related General Atomics code, GAROL, [3] also considers two space regions but takes into account overlapping and mutual shadowing of resonances in solving the slowing down equations based on the collision probability method.

Both codes are limited to two regions, but if more regions are used in the computation, a better approximation should be obtained because the collision probabilities are usually calculated assuming flat fluxes in each region. This would also make the Dancoff factors computation more complicated, since it requires considerable computational effort. However, with the increasing computing capability in modern computers, recent methods have included more resolution such as multiple regions and finer energy groups, which improve the accuracy of conventional methods for analyzing gas-cooled reactors. These more recent methods and associated codes are described in the next section.

1.2.3 More recent methods for analysis of gas-cooled reactors

We classify these more recent methods into two categories: Monte Carlo methods and deterministic methods.

- Monte Carlo methods

As a direct analog simulation method, the Monte Carlo method has the unique advantage of simulating neutron transport in complex geometries, including VHTR systems characterized by double heterogeneities and a stochastic distribution of fuel particles. Since many Monte Carlo methods utilize continuous energy cross sections,

resonance overlapping and mutual shadowing effects of resonances are automatically accounted for.

The MCNP5 Monte Carlo code [9] has been frequently used to model gas-cooled reactors with explicit geometric representation of fuel compacts or pebbles, including the microscopic fuel kernels within [10,11,12,13]. However, the random locations of the fuel kernels present difficulties. To date, four approaches have been tried for handling the randomness: (1) a regular lattice arrangement, ignoring any randomness [10,11,12,13], (2) the chord-length sampling approach in the MVP code based on NNDs (nearest neighbor distribution functions) [14,15,16] and recent research based on an empirical chord length PDF (probability density function) [17,18], (3) the explicit approach in MONK using "hole geometry" with a single realization of the entire random geometry [19], and in VHTR full core analysis using the random sequential addition (RSA) algorithm to generate multiple realizations of the entire random geometry [13,20], (4) the "on-the-fly" approach implemented in MCNP5 by randomly jiggling fuel kernels in regular lattice cells every time the neutron enters a cell [20,21].

- Deterministic methods

As routine analysis methods used widely in practice, deterministic methods for the analysis of gas-cooled reactors have been under continuous development, including efforts to improve the treatment of the double heterogeneity and stochastic geometry as well as the spectrum calculation in highly heterogeneous cells, especially in the resonance range. More recently, newer versions of codes such as WIMS and SCALES provide more powerful capability in modeling gas-cooled reactors, [22,23] generating space-dependent multi-group cross sections (few-group constants) and solving the transport equation in 1-D or 2-D geometries with methods including collision probability,

method of characteristics, S_n methods, and hybrid methods. In the WIMS code, an integrated Monte Carlo method (MONK) is embedded for the purpose of internal validation.

Both WIMS and SCALES can be used to analyze doubly heterogeneous configurations and generate shielded fine or broad group cell-homogenized cross sections at the fuel element level for prismatic reactors or the fuel pebble level for pebble-bed reactors. These cross sections can then be used in a global calculation code such as REBUS for global depletion calculations.

In an Argonne National Laboratory (ANL) report [22], the WIMS8 code was used to analyze a deep-burn gas-cooled reactor design based on the GT-MHR. A two-step scheme was utilized to homogenize the fuel assembly and obtain assembly-level shielded group cross sections. In the first step, the sequential use of the WPRES, WPROCOL and WRES modules performed a detailed analysis of the double heterogeneity at the compact-cell level. The compact-cell is composed of the fuel compact filled with coated fuel particles and an outer graphite region determined by the average share of the graphite in a fuel assembly for a fuel compact. Then shielded cell-homogenized group cross sections at the pin-cell level were obtained and provided to the next step of the calculation at the fuel element level. The CACTUS module was used to predict the fuel assembly group cross sections for subsequent global analysis. It should be noted that in the first step, before the use of the WPRES module, the shielded fine group cross sections for coated fuel particles in the fuel compact region had been obtained by using the WHEAD module based on equivalence theory. The treatment of the double heterogeneity in the WIMS code is quite similar to the GA MICROX code: at the grain structure level,

10

WIMS uses equivalence theory while MICROX uses Wälti's shielding factor method; at the compact-cell level, both codes use collision probability methods to calculate the fine-group flux and weighted broad group resonance cross sections.

In another study on a pebble-bed type gas-cooled reactor for burning plutonium [23], both the SCALE and WIMS codes were used to analyze a unit-cell at the fuel pebble level, accounting for the double heterogeneity. For the WIMS code, the same modules were used to analyze an equivalent cylindrical model, which has a fuel particle region surrounded by a pebble graphite shell. For the SCALE code, the treatment of double heterogeneity was implemented by a two-stage calculation: grain-cell level and pebble-cell level. The shielded group cross sections for the fuel zone at the pebble-cell level were generated by the grain level calculation based on the Nordheim Integral Method (NIM).

From the deterministic point of view, the treatment of the double heterogeneity configuration is a model that yields an equivalent homogeneous system by calculating the shielded cell-homogenized group cross sections through accurate or approximate techniques and methods. Such a homogenization process should be simple and fast. Those resultant group cross sections can be used for a full core computation with homogenized fuel assemblies in the global neutronic analysis code. Inevitably, such a multi-level homogenization method in the deterministic code, while simplifying and accelerating the global calculation, eliminates the possibility of predicting results at the microscopic level, such as the fuel microsphere in a VHTR. In some situations, the understanding of the neutronic behavior for individual fuel particles is important, such as in the fuel cycle analysis, where the depletion of the fuel kernel can provide useful

information in determining the optimum fuel cycle strategy. Also in safety analyses, the hot-spot analysis may require information about the stochastic nature of the distribution of the fuel particles and fuel pebbles. The analysis of these stochastic effects is difficult and perhaps impossible for deterministic codes.

1.3 Description of Thesis Work

1.3.1 Thesis goals and objectives

The goal of the thesis research is to develop a methodology to analyze fuel particles randomly distributed in the VHTR, accounting for kernel absorptions as well as the stochastic depletion of the fuel mixture. This method should be accurate enough to properly model stochastic particle fuel in both static and time-dependent configurations and yet be efficient enough to be used for routine analyses. This effort includes the creation of a new physical model, development of a simulation algorithm, and application to real reactor configurations.

1.3.2 Summary of thesis research

The thesis consists of four major chapters:

Chapter 2 describes the general neutronic analysis for a prismatic type VHTR using MCNP5 and the coupled depletion code ORIGEN (Monteburns). The VHTR is modeled explicitly, accounting for the double heterogeneity. The stochastic distribution of the fuel particles is also modeled explicitly inside the fuel compact using a RSA (Random Sequential Addition) algorithm [24] but only for a few realizations in full core analysis. The self-shielding behavior at resonance energies in the fuel kernel cell model is studied, and it is shown that a two-region cell model can adequately represent the six-

region microsphere cell with MCNP5. The equivalence between the two-region and six-region models is verified by criticality calculations at multiple levels: the microsphere cell level, the fuel compact cell level, and the full core model level with the fuel modeled as fully stochastic (RSA) and on a lattice. Global depletion calculations yield similar results. The benefit of the two-region model is a decrease in the Monte Carlo simulation time by a factor of two compared to a six-region model. For example, a typical calculation of a full core prismatic VHTR, modeling the fuel kernels on a lattice, may require two days on a 4 CPU cluster with Mac G5 processors, using the two-region model and one depletion time step.

Chapter 3 examines an alternative method, chord length sampling (CLS), to account for the stochastic distribution of fuel kernels in both VHTR designs. A theoretical derivation of the chord length PDF between two microsphere particles in an infinite medium is presented. The model is verified numerically by a direct Monte Carlo simulation at several different packing fractions and very good agreement is obtained. When the PDF is used for the CLS simulation in a finite medium, where overlapping of the kernels with the external boundaries needs to be accounted for, an effective packing fraction should be used in the PDF formula. This is done by a fast iteration calculation prior to the Monte Carlo simulation. Then the CLS Monte Carlo simulation is performed on two unit cells (a prismatic compact cell and a fuel pebble cell) using the analytical PDF with the corrected packing fraction. Excellent agreement with benchmark results are found in terms of resonance integrals in the fuel kernel, leakage rates from the external boundary, and the average scalar flux in different regions. Also, the average intra-

compact and intra-pebble Dancoff factors for the fuel kernel are calculated by the CLS method, and the predicted values are very close to benchmark results.

Chapter 4 presents a general method to derive closed form formulas for average Dancoff factors using the chord method in stochastic random media. The method greatly simplifies, mathematically and physically, existing analytical methods by replacing the multiple double integral calculations with multiple single integrals of the chord length PDF. As a typical application to VHTR analysis, two mathematical models are proposed to calculate average Dancoff factors for fuel compacts and fuel pebbles in infinite and finite geometries using the analytical chord length PDF derived in Chapter 3. Results are in good agreement with benchmark results.

Chapter 5 studies the impacts on neutronic properties with different random packing schemes. Three random packing schemes are investigated for infinite stochastic mixtures: lattice structure, the RSA model, and the jiggling model. The chord length distribution PDFs are determined for all three schemes at 28.92% and 5.76% packing fractions and substantial differences are found among the different random packing methods. Infinite medium Dancoff factors are averaged over many realizations for each of the random packing schemes. The maximum discrepancy in Dancoff factors is 0.2% at a 28.92% packing fraction and 5% for a 5.76% packing fraction, indicating that one needs to pay more attention to the neutronic analysis for lower packing fractions.

CHAPTER 2

Explicit Modeling of VHTR Configurations

In the previous chapter, we described VHTR configurations for both pebble-bed and prismatic type designs. Since our goal is to develop an efficient and accurate Monte Carlo methodology to analyze TRISO fuel particles in VHTR, we will use MCNP5 [9], a production-level, widely-used Monte Carlo simulation code, to perform our neutronic analyses. These analyses are for multi-scale geometry models ranged from individual TRISO fuel particle cells to fuel compact cells to full core configurations in prismatic type VHTRs. The analyses include spectra and radial flux distributions in a TRISO fuel kernel, as well as criticality computations for different geometry configurations and time-dependent depletion analyses for full core configurations.

2.1 MCNP Model of Full Core Geometry

Modeling the geometrical configuration of a reactor efficiently and accurately is critical for neutronic computations. The model should be kept as close as possible to the real geometry, with correct material composition and density. The model should also account for the double heterogeneity and stochastic distribution of fuel particles.

2.1.1 Microsphere cell to fuel compact cell to full core

Taking advantage of MCNP5's capability for modeling lattice structure geometry, we begin with a single TRISO microsphere cell, consisting of a cubic graphite matrix

containing a microsphere in the center. The cell preserves the volume packing fraction of microspheres in a fuel compact, i.e. 28.92% for the prismatic VHTR design. The microsphere, representing the TRISO fuel particle, has a fuel kernel region surrounded by four coating layers. The fuel kernel is the first heterogeneity. The five regions in a fuel particle are depicted in Figure 2.1 and the TRISO data are given in Table 2.1. The isotopic densities in each region are given in Table 2.2.
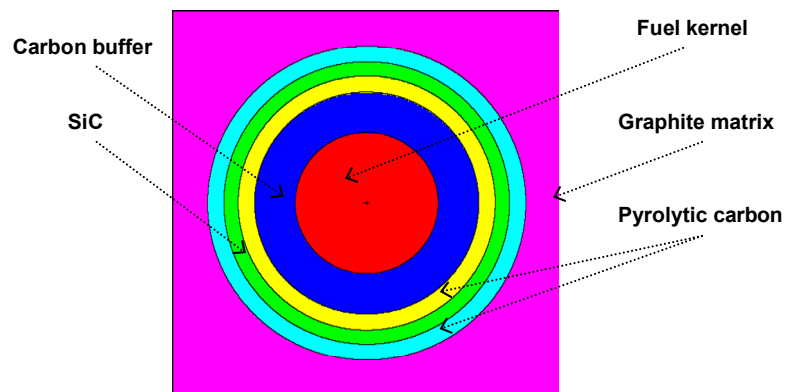
Figure 2.1 Heterogeneous microsphere cell for TRISO fuel

Table 2.1 TRISO dimensions and compositions

Region #	Name	Outer radius (μ)	Composition	Density (g/cc)
1	Uranium oxycarbide	175	UCO ($UC^{.5}O^{1.5}$)	10.5
2	Porous carbon buffer	275	C	1.0
3	Inner pyrolytic carbon	315	C	1.9
4	Silicon carbide	350	SiC	3.2
5	Outer pyrolytic carbon	390	C	1.9

Table 2.2 TRISO number densities

Region #	Isotope	Number density (at/b-cm)
1	U235	.002475
	U238	.021143
	C	.011809
	O	.035426
2	C	.050137
3	C	.095261
4	C	.048060
	Si	.048060
5	C	.095261

The next step is the fuel compact cell, which consists of the cylindrical fuel compact, consisting of a mixture of microspheres and the background graphite matrix, centered in a hexagonal graphite cell. The size of the hexagonal cell is determined by the amount of graphite in the fuel block that "belongs" to each fuel compact. The fuel compact comprises the second heterogeneity. Table 2.3 specifies the layout for a standard fuel block shown in Figure 2.2.
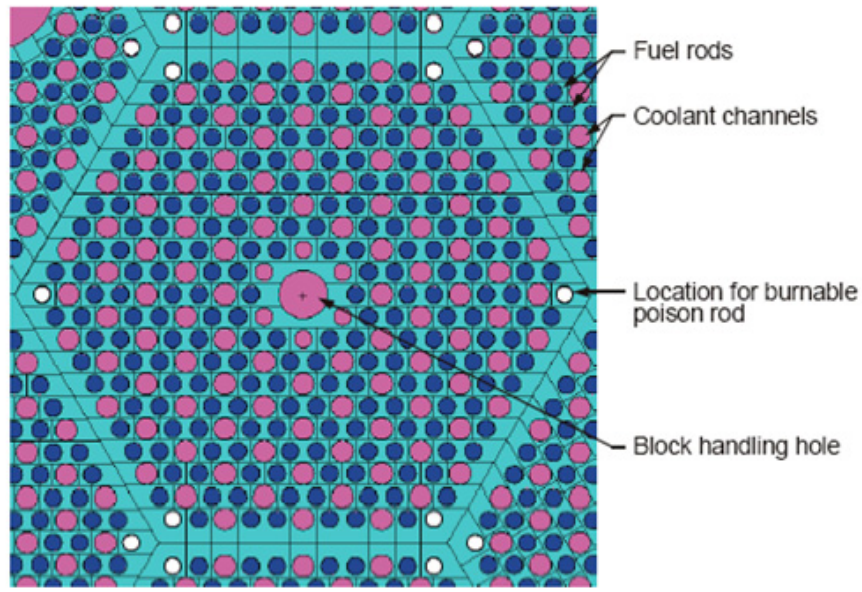
Figure 2.2 A standard fuel block (from [2])

Table 2.3 Layout of regular TRISO fuel block

Item	Diameter (cm)	Number	Total area (cm^2)
Small coolant holes	1.27	6	7.60
Large coolant holes	1.588	102	202.02
Fuel compact holes	1.27	216	273.62
			483.24

The flat-to-flat dimension of the hexagonal fuel block is 35.996 cm, resulting in a

total fuel block area $A = \dfrac{\sqrt{3}d^2}{2} = 1122.18$ cm^2, hence a total graphite area of $1122.18 -$

$483.24 = 638.93$ cm^2 which yields the graphite (moderator) area per fuel compact $A_M =$

2.958 cm^2. Modeling this as a hexagonal graphite region surrounding the inner cylindrical

fuel compact with diameter D_F = 1.245 cm, we find the flat-to-flat dimension of the fuel compact cell to be d_c = 2.1958 cm.

Next, we need to model a hexagonal fuel block with coolant holes and fuel compacts filled with TRISO fuel particles. For simplicity, we ignore the large handling hole centered in a standard fuel block and the six small coolant holes. Instead, they are replaced by several large coolant holes and fuel compacts. There are 109 large coolant holes and 222 fuel compacts in a fuel block. Each coolant hole or fuel compact is in a hexagonal lattice with a flat-to-flat dimension of 1.8796 cm. The coolant hole cells and fuel compact cells form a hexagonal fuel block cell as shown in Figure 2.2. Each fuel block cell is 79.3 cm high.

Next, a full core configuration model can be set up with a simplified fuel block model with fuel compacts filled with TRISO particles. The full core is modeled as a cylinder of hexagonal blocks with radius 341.63 cm and height 951.6 cm, equivalent to the height of 12 blocks (fuel and graphite blocks have the same height). The reactor is composed of an inner reflector region, three fuel ring regions, top and bottom reflectors, and an outer reflector region. The inner and outer reflector regions consist of 12 graphite blocks stacked axially, while the fuel rings are ten blocks with one single reflector blocks at both the top and bottom of the core. At each axial level, there are 30 fuel blocks in the inner ring, 36 fuel blocks in the middle ring, and 36 fuel bocks in the outer ring, for a total of 102 fuel blocks. Since there are ten axial layers of fuel blocks, the total number of fuel blocks in the full core is 1020.

Thus, a full core model accounting for the double heterogeneity configuration using MCNP5 is completed. Figure 2.3 shows the geometry progression from a microsphere cell to full core.

Fuel block

Full core

Fuel compact

Microsphere particle
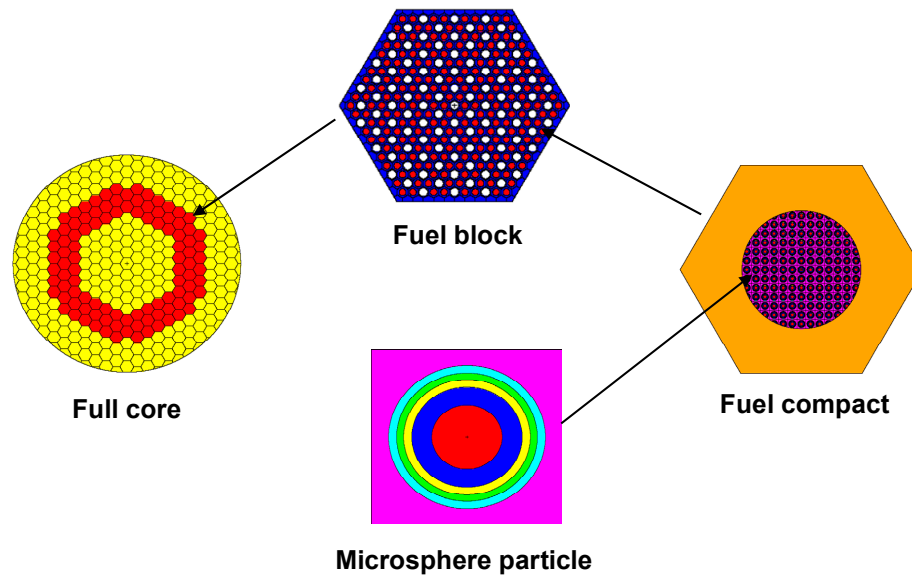
Figure 2.3 Cross sectional view of MCNP models from fuel particle to full core

2.1.2 Model improvements

The MCNP5 models in the previous section have explicitly modeled all five regions of the microsphere. This results in a very large number of MCNP5 regions, which causes the execution time to increase and could become a limiting factor due to the MCNP5 limit on the number of distinct regions, especially when depletion is accounted for. In addition, the previous models have resulted in "clipped" microspheres due to the fuel compact cylinder intersecting the universe (lattice) of microsphere cells. Clipped cells are an artifact of the geometrical modeling and are not physical and should be eliminated. Our previous model will be improved to reduce the number of regions and

eliminate clipped cells so as to improve both the efficiency and accuracy of the Monte Carlo model.

2.2 Physical Geometry Simplifications

This section addresses both of these issues. First, as a result of a thorough study regarding the neutronic behavior in a microsphere cell, a new two-region model has been developed and tested for the microsphere cell. The two-region cell reduces the region count by a factor of 3 and reduces the execution time by a factor of two, compared to the six-region cell. Secondly, the fuel region model has been modified to eliminate the "clipped" microspheres, and the results indicate that this is an important effect that needs to be included. A number of MCNP5 calculations have been performed to substantiate these conclusions, including simulations with randomly packed fuel compacts.

2.2.1 Detailed neutronic analysis of TRISO microsphere cell

First, energy spectra in the fully heterogeneous microsphere cell model (six-region model) were calculated. The calculations were done separately for all six regions of the cell depicted in Figure 2.1. Figure 2.4 shows the results, and it can be seen that except for the neutron energies close to the resonance peaks, which Figure 2.4 does not resolve, the average spectra are essentially the same in all regions of the microsphere cell. This indicates that the TRISO fuel is effectively homogeneous for all neutrons except resonance energy neutrons. Additional evidence in support of this conclusion is given in the next section.
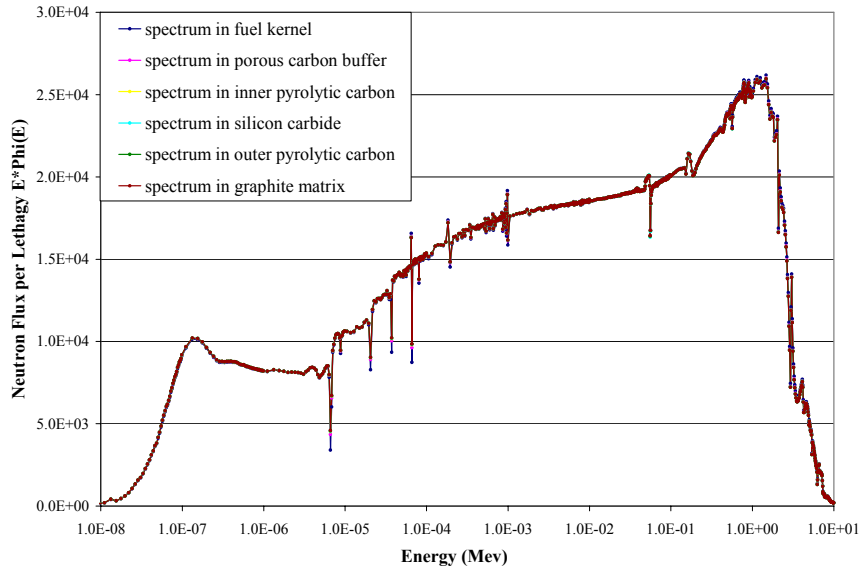
Figure 2.4 Spectra for six-region microsphere model

Another important physical quantity, the energy-dependent radial flux profile in a six-region microsphere cell, was also calculated. The radial tally regions for the energy-dependent track length estimator are depicted in Figure 2.5, and the results are shown in Figure 2.6.
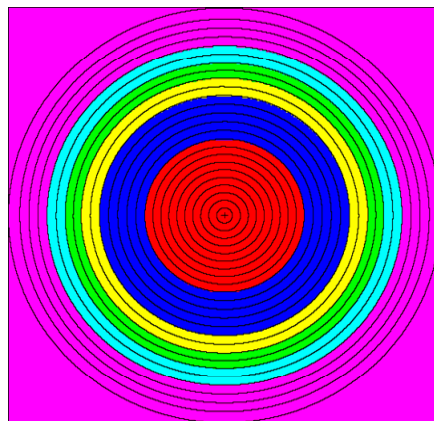
Six-region heterogeneous

Reflecting b.c. on all sides of cube

Figure 2.5 Tally regions for six-region microsphere cell
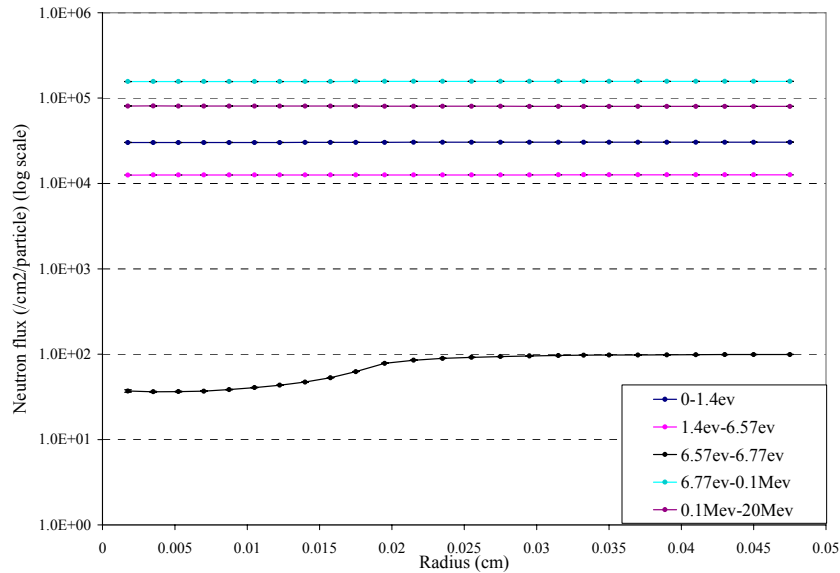
Figure 2.6 Radial neutron flux profiles in six-region microsphere cell

From Figure 2.6, it is clear that for non-resonance energies, the flux is not perturbed by the presence of the fuel kernel and is essentially flat, equivalent to the flux in an equivalent homogenized cell. Therefore, we conclude that the double heterogeneity is only important for resonance-energy neutrons, and the microsphere cell is homogeneous for all neutrons except resonance energy neutrons. Moreover, even for resonance neutrons, the coating and graphite matrix regions are essentially homogeneous, since their radial scalar flux profiles are flat.

2.2.2 From six-region to two-region model for microsphere cell

The neutronic analysis in the previous section suggests a possible way to simplify the six-region heterogeneous microsphere cell. The approach is to keep the fuel kernel intact and homogenize (volume weight) the four microsphere coatings and the graphite

matrix. As a result, the six-region becomes a two-region microsphere cell with a fuel

kernel surrounded by the homogenized coating-matrix region, as depicted in Figure 2.7.

Six-region heterogeneous   Two-region heterogeneous

Reflecting b.c. on all sides of cubes
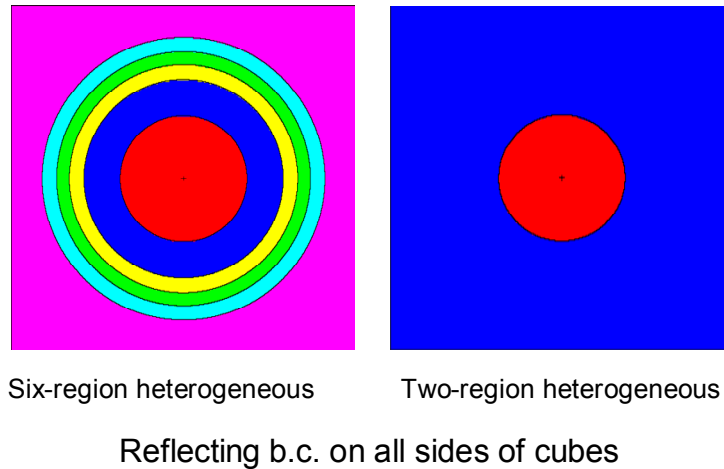
Figure 2.7 From six-region to two-region microsphere cells

In order to show the validity of this two-region model, the same spectra and radial

scalar flux profiles were calculated with the two-region model and compared with the

corresponding quantities using the six-region model and are shown in Figure 2.8. Figure

2.9 shows the tally region divisions for the radial flux profiles for the two-region model.

Figure 2.10 compares the resultant radial flux profiles for two-region versus six-region

calculations for the energy range centered around the 6.67 eV resonance of U-238. These

comparisons show excellent agreement, demonstrating that for lattice geometry, the two-

region model is acceptable for the heterogeneous microsphere cell.
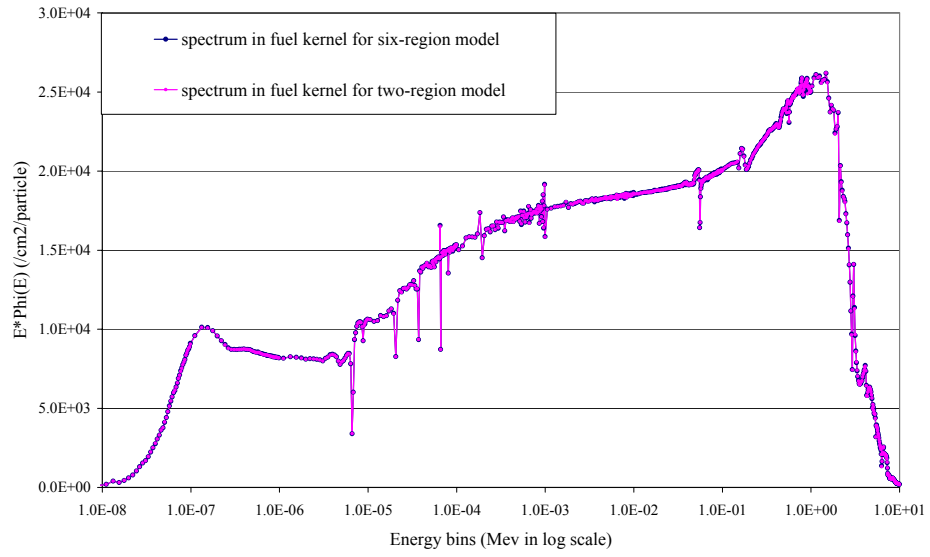
Figure 2.8 Spectra comparison between six-region and two-region models in fuel kernel
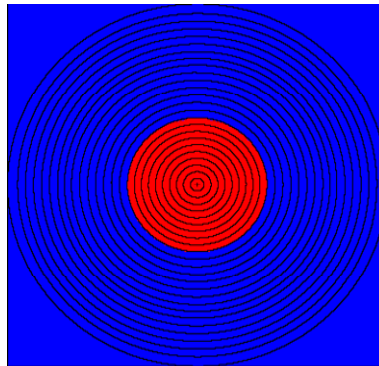
Two-region heterogeneous

Reflecting b.c. on all sides of cubes

Figure 2.9 Tally regions for two-region microsphere models
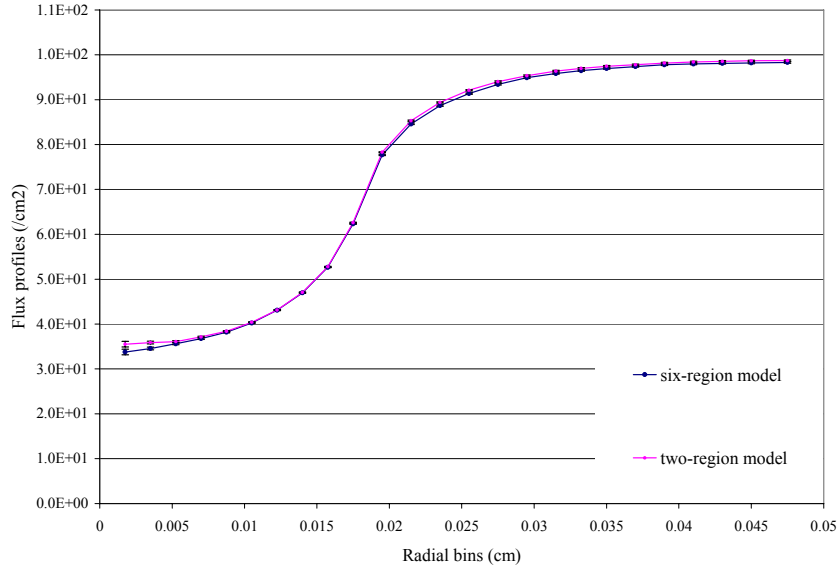
Figure 2.10 Radial flux profile in energy group 6.57ev-6.77ev

Criticality calculations using MCNP5 for the two-region and six-region

microsphere cells were performed, and the values of k_{inf} are listed in Table 2.4 along with

the standard deviations in the estimates of k_{inf}. Again, excellent agreement is obtained.

Table 2.4 MCNP5 simulations of microsphere cells

Configuration	Kernel location	k_{inf}	Sigma
Two-region heterogeneous cell	Centered	1.1535	.0004
Six-region heterogeneous cell	Centered	1.1533	.0003

2.2.3 From six-region to two-region model for fuel compact cell

The neutronic analysis was also done at the fuel compact level using the six-

region and two-region models, as well as a homogeneous model for comparison. Figure

2.11 shows the three different MCNP5 fuel compact models. The graphite region

surrounding the fuel compact is the proportional share of the graphite in a hexagonal fuel

block that "belongs" to a fuel compact. The homogeneous model consists of a

homogenized mixture of the fuel kernel, coating, and graphite matrix regions into one

fuel region.

Six-region heterogeneous   Two-region heterogeneous   Homogeneous

Reflecting b.c. on all surfaces of fuel compact cell
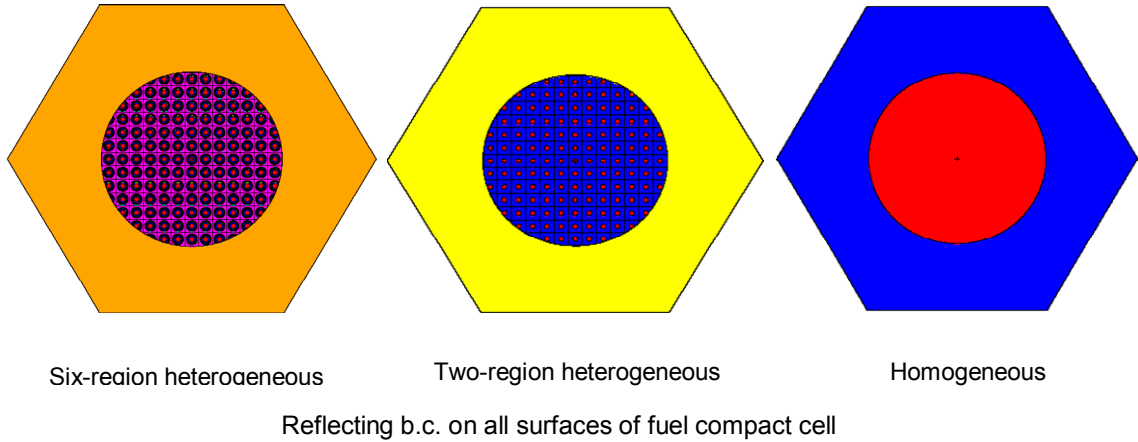
Figure 2.11 Fuel compact cells

Criticality computations using MCNP5 for the three compact cell models were

also performed, and the results are tabulated in Table 2.5. The results show that the fuel

kernel heterogeneity is important at the fuel compact level, yielding a 4% increase in

reactivity compared to a homogenized fuel region. Again, two-region and six-region

results show very good agreement with each other.

Table 2.5 MCNP5 simulations of fuel compact cells

Fuel compact filled with	k_{inf}	Sigma
Homogeneous microsphere cells	1.2885	.0004
Two-region heterogeneous microsphere cells	1.3408	.0004
Six-region heterogeneous microsphere cells	1.3401	.0004

2.2.4 Eliminating "clipping" in the fuel compact model

A closer look at the preliminary MCNP5 models depicted in Figure 2.3 of the heterogeneous microsphere cells in the fuel compact shows "clipped" or partial microspheres at the cylindrical boundary of the fuel compact. This is an artifact of the MCNP5 geometry handling routines for imbedding a universe (the lattice of microspheres) in an enclosing body (the outer diameter of the fuel compact). This unphysical anomaly is illustrated in Figure 2.12. Clipping may change the packing fraction; however, a more important consequence is the reduction in the self-shielding, since the escape probability from a partial fuel kernel will be significantly larger than for a full kernel, which is equivalent to a reduction in the self-shielding. This reduction in the self-shielding of the fuel kernel will increase the resonance absorption, resulting in a decrease in k_{inf}. Even though this effect is due to only those kernels on the boundary of the fuel compact, this reactivity bias is noticeable in Table 2.6.
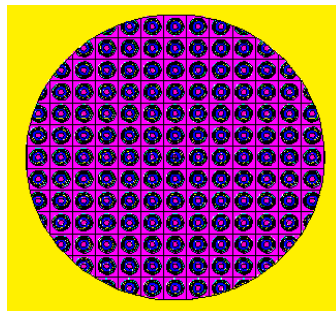
Figure 2.12 Clipped model

In order to correct this error caused by clipping while keeping the total packing fraction constant, two models were investigated. These models are depicted in Figure 2.13.

Unclipped model 1   Unclipped model 2
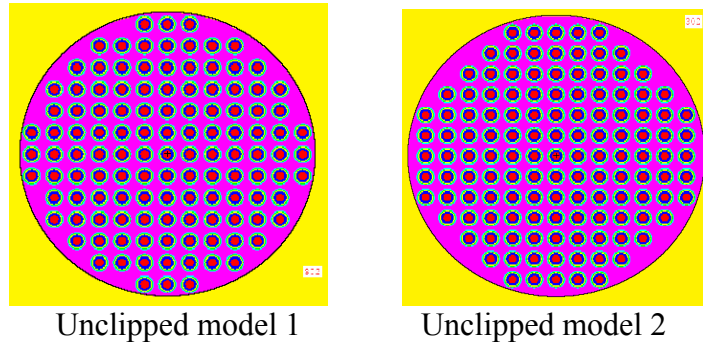
Figure 2.13 Unclipped models

Both models still use simple cubic lattice structures, but the lattice cells in the x-y plane are adjusted to avoid clipping and preserve the packing fraction. In model 1, the z-dimension of the "cubical" cell is reduced to preserve the overall packing fraction, but the x and y dimensions are left unchanged, resulting in a non-cubical cell (a cuboid), which is then repeated throughout the fuel compact cylinder to form a finite lattice of microspheres. For a packing fraction of 0.289, this results in 121 microspheres in the x-y plane for model 1. In model 2, the cube is uniformly squeezed in three dimensions to yield the desired packing fraction, and this cubical cell is then repeated throughout the fuel compact. There are 129 microspheres in the x-y plane for model 2. Neutronic results are shown in Table 2.6 for clipped cells and for unclipped cells using both models 1 and 2. Both models 1 and 2 yield k_{inf} higher than with the clipped model, a consequence of the artificial reduction in the self-shielding for the clipped fuel kernels as noted above. Model 2 is preferred because it preserves a simple cubic lattice while maintaining the correct packing fraction.

Table 2.6 Clipped versus unclipped fuel compact cells

Fuel region modeled as	k_{inf}	Sigma
Six-region microsphere cells (clipped)	1.3401	.0004
Six-region microsphere cells (not clipped using model 1)	1.3438	.0002
Six-region microsphere cells (not clipped using model 2)	1.3445	.0002
Two-region microsphere cells (clipped)	1.3408	.0004
Two-region microsphere cells (not clipped using model 1)	1.3435	.0002
Two-region microsphere cells (not clipped using model 2)	1.3447	.0002

2.2.5 Lattice and stochastic models for TRISO fuel

A lattice structure in VHTR analysis is a good model for TRISO fuel particles. However, in reality, the TRISO fuel particles are randomly distributed in the fuel compact. As a result, alternative models were explored for accurate computations.

A straightforward way to model this stochastic distribution is to "jiggle" the microsphere within its cell. Every time a neutron enters a new microsphere cell, the microsphere in that cell is moved randomly within the cell but constrained to stay wholly within the cell. This method can take advantage of modeling the microspheres on a lattice, which is relatively easy to analyze with MCNP5. Brown et al.[12,20,21] have studied this model and implemented it in the new release of MCNP5. In this way, randomness is local, i.e. bounded only inside a cubic cell.

Although it is a local stochastic model, the effect of such randomness on neutronic behavior may be modeled by comparing the radial flux profile in a microsphere cell with white boundary conditions (isotropic return) versus reflecting boundary

conditions. The white boundary condition qualitatively represents the randomness of the location of the microsphere within the cell. (The next section substantiates this.) The tally region for this case is the same as shown in Figure 2.5, except that the boundary condition is white. Figure 2.14 shows the comparison of the radial flux in the resonance energy group between reflecting boundary conditions and white boundary conditions.
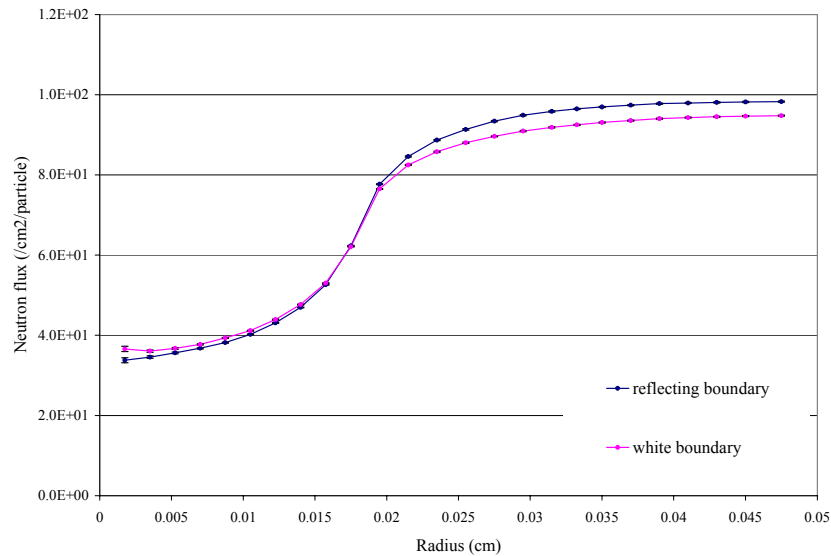
Figure 2.14 Neutron radial flux profile in energy group 6.57ev-6.77ev

If we assume that the slowing down source in the graphite matrix is the source for the fuel kernel, then the ratio of the absorption in the fuel kernel to the flux in the graphite matrix gives the reactivity effect. If this "absorption ratio" is high, it means that fewer neutrons escape the resonance. From Figure 2.14, it is seen that the white b.c. case yields a higher absorption ratio, hence less self shielding and if the curves were normalized by the level in the graphite matrix, there would be less depression in the fuel kernel for the white b.c. case. This makes sense physically as the white b.c. option throws more neutrons out of the path of the kernels, equivalent to a stochastic effect.

Another way to explicitly model the stochastic distribution is a model with global randomness. This is a more realistic model of the stochastic mixture of microsphere particles. As an example, it has been examined at the fuel compact level, whereby microspheres are randomly distributed in the fuel compact. This was studied by using the RSA (Random Sequential Addition) method [24] for both the six-region and two-region fuel compact models. This was done by taking a single fuel compact, which has an average of 6050 microspheres using a packing fraction of .289, and subdividing it into 50 axial layers, each containing 121 microspheres. RSA was then used to insert the 121 microspheres randomly within each layer. Each layer was statistically different, so this may be described as a "stratified" RSA approach. An MCNP5 input deck was then written for the compact cell, explicitly accounting for the 6050 randomly placed microspheres. Figure 2.15 illustrates the "stratified" RSA models and Table 2.7 compares two physical realizations of each of the two-region and six-region RSA models.
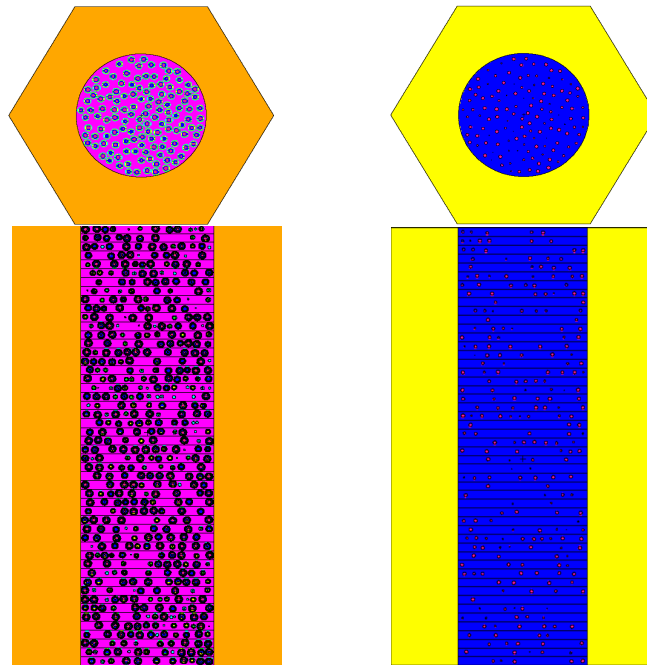
Figure 2.15 Two-region and six-region RSA models

Table 2.7 Fuel compact cells with stratified RSA models

Fuel region modeled as 50 layers with	k_{inf}	*Sigma*
Two-region RSA model (realization 1)	1.34232	.00023
Six-region RSA model (realization 1)	1.34262	.00022
Two-region RSA model (realization 2)	1.34243	.00022
Six-region RSA model (realization 2)	1.34275	.00022

Table 2.7 shows the equivalence of the two-region and six-region RSA models. A comparison of Table 2.6 and Table 2.7 shows that the stochastic effect (RSA versus a lattice of kernels) is small: either two-region or six-region RSA models yield ~ 0.15% decrease in k_{inf} compared to the corresponding lattice models. In order to investigate the axial effect of this stratified model, RSA was used to generate a more random distribution of two-region microsphere cells by using 10 axial layers rather than 50 layers, as shown in Figure 2.16. The results are compared in Table 2.8, where it is seen that the stratified model with 10 layers yields essentially the same results (within .02% k_{inf}) as the 50 layer case.
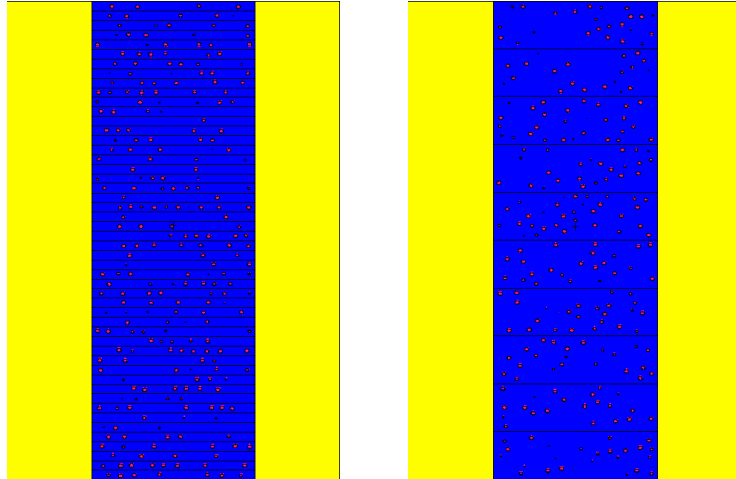
Figure 2.16 Fuel compact cells modeled with 50 RSA layers and 10 RSA layers

Table 2.8 Fuel compacts modeled with 50 RSA layers versus 10 RSA layers

Fuel region modeled as	k_{inf}	Sigma
Two-region fifty-layer randomly distributed microsphere cells (average over 19 realizations)	1.34228	.00019
Two-region ten-layer randomly distributed microsphere cells (average over 2 realizations)	1.34258	.00022

We have also modeled hexagonal fuel block geometry, where coolant holes and fuel compact cells are modeled explicitly. These calculations have been done with homogeneous and heterogeneous fuel compacts, but the results are not included in this thesis, since they are consistent with the fuel compact results and we also have full-core results to present.

2.3 Comparison of Neutronic Computation Results in Full Core

Based on the microsphere cell and fuel compact cell models, we have modeled the full core geometry with MCNP5 as shown in Figure 2.3.

2.3.1 Static criticality computation

Early calculations were performed with MCNP5 for four different full core

configurations, where all fuel blocks and all axial and radial reflector blocks are modeled.

These simulations assumed 6.69 ppm boron-10 impurity in the graphite fuel blocks and

reflector blocks in accordance with the NGNP Point Design Report [2]. This has since

been determined to be 6.69 ppm natural boron, not boron-10, but these results will be

presented anyway, since the relative changes in k_{eff} are of interest, not the actual value of

k_{eff}. For these cases, the fuel blocks were modeled as:

(1) Homogeneous fuel blocks

(2) Heterogeneous fuel blocks with homogeneous fuel

(3) Heterogeneous fuel blocks with two-region heterogeneous fuel

(4) Heterogeneous fuel blocks with six-region heterogeneous fuel.

Case (1) does not account for either portion of the double heterogeneity, because

both the fuel kernels and the fuel compacts are homogenized, while Case (2) only

accounts for the fuel compact heterogeneity and Cases (3) and (4) account for both the

fuel compact and fuel kernel heterogeneities. Table 2.9 presents the results.

Table 2.9 MCNP5 simulations of full core configurations

Case	Full core modeled with:	k_{eff}	Sigma
1	Homogeneous fuel blocks	1.0153	.0002
2	Heterogeneous fuel blocks with homogeneous fuel regions	1.0583	.0001
	Heterogeneous fuel blocks with fuel regions modeled as:		
3	Six-region microsphere cells (clipped)	1.0949	.0002
4	Six-region microsphere cells (not clipped using model 1)	1.0957	.0002
5	Six-region microsphere cells (not clipped using model 2)	1.0966	.0002
6	Two-region microsphere cells (clipped)	1.0952	.0002
7	Two-region microsphere cells (not clipped using model 1)	1.0959	.0002
8	Two-region microsphere cells (not clipped using model 2)	1.0965	.0002
9	Two-region randomly distributed microsphere cells (RSA)	1.0948	.0002

On the basis of the results, it is evident that modeling the double heterogeneity is a necessity for full core VHTR analysis. The effect of the second heterogeneity (fuel compact heterogeneity) is seen to be 4% by comparing Cases 1 and 2 in Table 2.9. The effect of the first heterogeneity (fuel kernel heterogeneity) is seen to be another 4% by comparing Cases 2 and 4.

The results given in Table 2.9 corroborate the results for the fuel compact cell cases given in Table 2.6, showing that the two-region cells are adequate for full-core configurations. This can be seen by comparing Cases 4 and 7 or Cases 5 and 8. Therefore, the two-region microsphere cell gives acceptable results (< .02%) for all comparisons, from microsphere cell to full core. In addition to speeding up the MCNP5

calculations by a factor of two, this allows the analysis of larger systems due to the MCNP5 limit on the number of regions. This may be a limiting factor for full core depletion cases.

A comparison of Cases 3 and 4 or Cases 6 and 7 shows that clipping the microsphere cells is less significant for full core (~ 0.1%) than for the fuel compact cell (~ 0.3%). This is consistent with previous observations regarding the effect of the double heterogeneity for finite geometries versus infinite geometries, because the finite geometries include the graphite reflectors and the increased moderation reduces the impact of the change in resonance absorption due to the particle fuel. Since it is easy to do so, clipping the cells should be avoided to eliminate the unphysical geometry.

A comparison of Cases 7 or 8 with Case 9 shows that the effect of modeling the stochastic distribution of fuel particles with a lattice of fuel particles results in ~ 0.15% reactivity effect for a full core simulation. This is consistent with the fuel compact results, where the reactivity effect was ~ 0.17% from a comparison of the unclipped and RSA two-region models given in Table 2.6 and Table 2.7.

The effect of fuel temperature feedback was also examined, which is important for the VHTR since it is operated at very high temperatures. Using the coupled thermal/hydraulic calculation done by Conlin et al.[25,26] and Yesilyurt et al.[27], the temperature distribution throughout the reactor core was obtained and is shown in Table 2.10. It is noted that the temperature in the reflectors was assumed to be the average temperature in the full core. In practical computations, the highlighted numbers may vary according to different cases, such as choosing the temperature in the closest fuel ring block as the temperature in the reflector blocks. MCNP5 was then run with the fuel

regions modeled at the temperatures given in Table 2.10, and the results are in Table 2.11. For these cases, the boron impurity in graphite was assumed to be 6.69 ppm of natural boron in graphite.

Table 2.10 Temperature distribution for 30 fuel regions and reflectors

Inner Reflector	Inner Ring	Middle Ring	Outer Ring	Outer Reflector
1020 K	1020 K	1020 K	1020 K	1020 K
1020 K	889 K	891 K	882 K	1020 K
1020 K	993 K	981 K	965 K	1020 K
1020 K	1076 K	1058 K	1037 K	1020 K
1020 K	1147 K	1123 K	1097 K	1020 K
1020 K	1204 K	1175 K	1145 K	1020 K
1020 K	1248 K	1215 K	1183 K	1020 K
1020 K	1280 K	1243 K	1208 K	1020 K
1020 K	1298 K	1258 K	1222 K	1020 K
1020 K	1303 K	1261 K	1225 K	1020 K
1020 K	1295 K	1251 K	1216 K	1020 K
1020 K	1020 K	1020 K	1020 K	1020 K

From room temperature to high temperature calculations, there is a 5% change in k_{eff}. Both six-region and two-region models consistently reflect this large effect. This is due to the Doppler broadening of the resonance capture cross sections of the fuel. Also, Table 2.11 indicates that a uniform temperature distribution in the fuel region yields a k_{eff} that is higher by 1% than the distributed temperature case with the same average temperature. Therefore, it is important to predict an accurate temperature distribution in the VHTR to get accurate simulation results.

Table 2.11 MCNP5 full core simulations with heterogeneous fuel blocks

Heterogeneous fuel blocks with fuel regions modeled as six-region microsphere cells (not clipped using model 2)	k_{eff}	Sigma
Room temperature	1.3190	.0002
Uniform temperature at 1020K	1.2714	.0001
Distributed temperature in active core and 1020K in reflectors	1.2608	.0001
Distributed temperature in active core and in reflectors	1.2606	.0001
Heterogeneous fuel blocks with fuel regions modeled as two -region microsphere cells (not clipped using model 2)		
Room temperature	1.3187	.0002
Distributed temperature in active core and in reflectors	1.2622	.0001

2.3.2 Time-dependent depletion computation

Depletion analysis is another important issue that needs to be accounted for in the full core simulation. Depletion calculations have been performed for full core models at room temperature and elevated temperatures. Figure 2.17 compares the predicted k_{eff} rundown for room temperature and elevated temperature cases with heterogeneous fuel blocks with six-region microsphere cells. Figure 2.18 compares the reactivity rundown for six-region vs. two-region full-core models at room temperature and the difference is negligible.
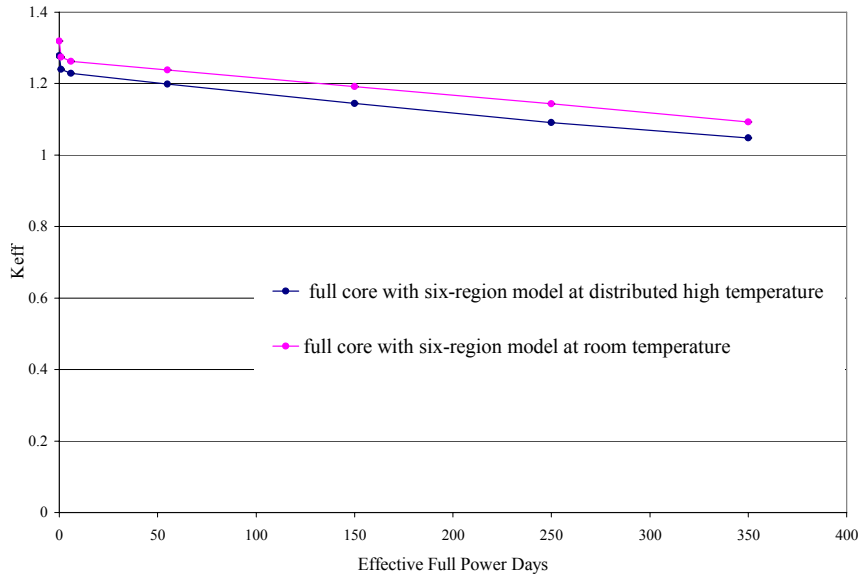
Figure 2.17 Depletion comparison: room temperature versus distributed temperature
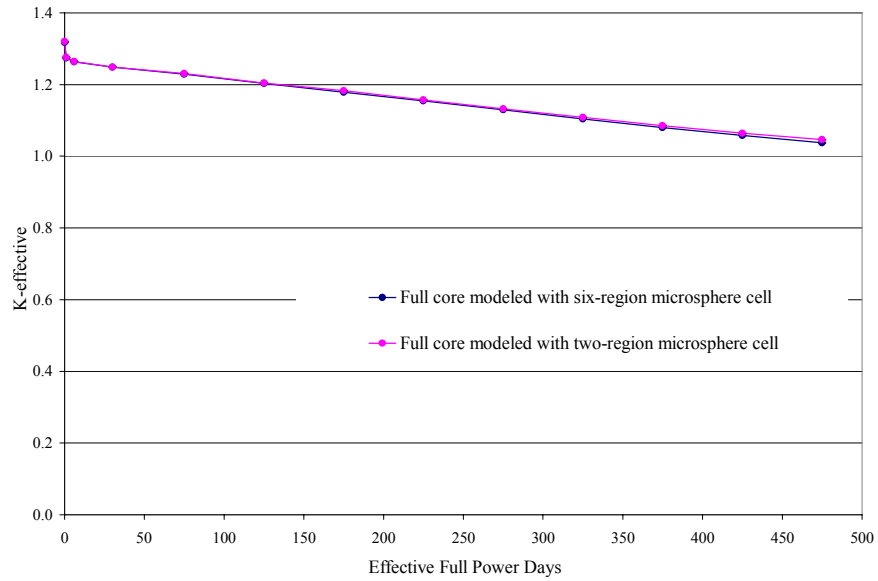
Figure 2.18 Depletion comparison: two-region versus six-region models

40

CHAPTER 3

Chord Length Sampling Method with Application to VHTR Configurations

3.1 Introduction

The Very High Temperature Gas-Cooled Reactor (VHTR) is a potential

Generation IV design. Two types of designs are considered for the VHTR, the prismatic

block reactor and the pebble bed reactor [2,28]. Both designs use TRISO fuel, which is a

stochastic mixture of coated microspheres (of diameter 0.78 mm) that are randomly

distributed in a background graphite matrix with a volume packing fraction of 28.9% for

prismatic fuel and 5.76% for pebble bed fuel. The TRISO fuel kernels present a

prohibitive computational challenge to traditional neutronic analysis because they are

strong absorbers for resonance energy neutrons, resulting in the well-known "double

heterogeneity" caused by the fuel kernels at the first level and the fuel compacts (or fuel

pebbles) at the second level. Methods for treating the double heterogeneity range from

the calculation of Dancoff factors in order to augment traditional resonance integral

calculations to detailed Monte Carlo simulations that take into account the detailed

geometry of the VHTR including resolution of individual microspheres [12,29].

Explicit Monte Carlo simulation of the VHTR is very time-consuming (For

example, a typical full core criticality calculation needs about a week on a Macintosh G5

with a single CPU, with 100K neutron histories per cycle with 80 inactive and 200

active cycles.), and may not be feasible when space-dependent phenomena are accounted for, such as depletion and temperature feedback. We have studied an alternative methodology to analyze particle fuel that is based on chord length sampling (CLS). The CLS methodology is applied to general Monte Carlo simulation as well as to the calculation of Dancoff factors in cubical, spherical, and cylindrical geometries filled with stochastically distributed microspheres.

3.2 Chord Length Sampling Methodology

3.2.1 Historical review

As far as the author knows, the CLS method was first studied in a 1D geometry [30] to avoid explicitly modeling the stochastic mixture in 1991. The basic idea of CLS is to treat the stochastic geometry as a binary stochastic mixture whose two components are characterized by chord length probability distribution functions (PDFs). The Monte Carlo simulation proceeds by sampling a distance to collision in the current medium and comparing to a distance to the medium boundary that was sampled from the chord length PDF for the current medium. If a neutron crosses a medium boundary, this process is repeated in the second medium. Figure 3.1 shows the algorithms for both the regular Monte Carlo random walk and the CLS random walk.
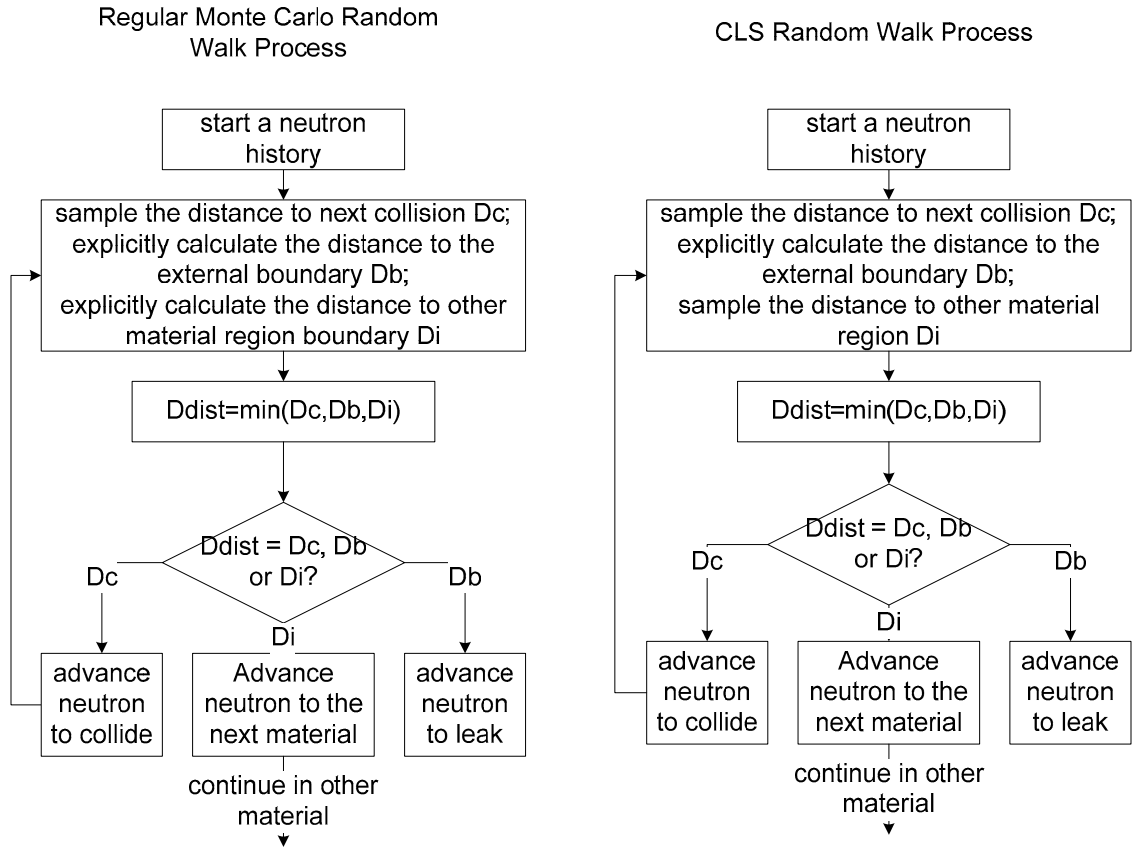
Figure 3.1 Random walk with regular Monte Carlo and CLS methods

A variation on CLS, called limited chord length sampling (LCLS) [17] was examined in a 2D geometry for stochastic mixtures similar to TRISO fuel. For LCLS, chord length sampling is only done in the background medium, and conventional Monte Carlo is performed in the fuel region, which is a microsphere in the case of TRISO fuel. The results were promising, but there were several areas that warranted further investigation: (1) the results were limited to 2D, (2) the chord length PDFs were based exclusively on empirical chord length distributions, (3) microspheres near the external boundary needed to be treated carefully to avoid overlap with the boundary, and (4) one needed to account for the fact that a neutron leaving a microsphere may preferentially backscatter into the same microsphere.

A method very similar to LCLS had been developed earlier by Murata et al.[15,16] for the analysis of TRISO fuel in both prismatic and pebble-bed reactors. This method included effective chord length sampling along the neutron flight path to find the next microsphere using the nearest neighbor distribution (NND) function, and then conventional Monte Carlo within the microsphere. The NND function $N(r)dr$ is defined as the probability of finding the nearest fuel particle whose center lies at a distance between r and $r+dr$ [15,16,36]. Depending on the starting point in the system, there are three NND functions: starting from (1) the surface of a microsphere (NND1), (2) from the graphite matrix (NND2), or (3) from the surface of external boundary (NND3). Murata et al. had examined these three NNDs and obtained them with direct Monte Carlo simulation of a random medium employing the collective rearrangement algorithm (see Section 5.2.2). These empirical NNDs were used and excellent results were obtained in criticality calculations. Moreover, Murata et al. had accounted for the boundary effect inherent in their method by proposing two solutions: (1) using NNDs generated at a higher packing fraction (prismatic type reactor) and (2) allowing interference to exist (pebble-bed reactor). Murata's method is essentially a chord length sampling method with empirical NNDs, rather than analytical chord length PDFs, as we have done, to sample the distance to the next microsphere.

3.2.2 Using CLS to analyze stochastic distribution of fuel kernels

To yield a method capable of analyzing realistic TRISO fuel configurations, we have based the chord length PDF for the background medium on a theoretical model rather than an empirical model. We have validated the theoretical chord length PDFs for the background medium with benchmark Monte Carlo simulations. These chord length

PDFs were then used in a stochastic mixture representative of TRISO fuel with neutrons at the 6.67 eV resonance of U238. A general neutron transport analysis including leakage rates, flux integrals, and resonance absorption rates for different geometry configurations was performed using the CLS method. Also, Dancoff factors for infinite and finite media (sphere and cylinder) were calculated based on the CLS method.

These calculations were performed using packing fractions ranging from pebble bed reactors (~ 5%) to prismatic type reactors (~ 29%), and the predictions were compared with the benchmark Monte Carlo results. The results are very promising and suggest that the CLS method with theoretical PDFs can be used to analyze TRISO fuel for both pebble bed and prismatic type reactors.

3.3 CLS Probability Distribution Function

Up till now, we have assumed that CLS consisted of a single exponential PDF to sample a distance to a microsphere, regardless of whether the neutron was: (1) on the incoming boundary of the stochastic region, (2) on the outgoing boundary of a microsphere, or (3) within the background portion of the stochastic region. In the current work, we generalize the notion of chord length sampling to include three different chord length PDFs:

- $f_{b \to m}$ – chord length PDF from the external boundary (b) to a microsphere (m)

- $f_{m \to m}$ – chord length PDF from the microsphere (m) to another microsphere (m)

- $f_{g \to m}$ – chord length PDF from the graphite (g) matrix to a microsphere (m)

Figure 3.2 depicts a 3D binary stochastic mixture of microspheres within a box of background material. This is an actual realization of microspheres using the RSA

algorithm [24,31] to add spheres to the box. We will now derive the chord length

distribution that characterizes the background material in Figure 3.2.
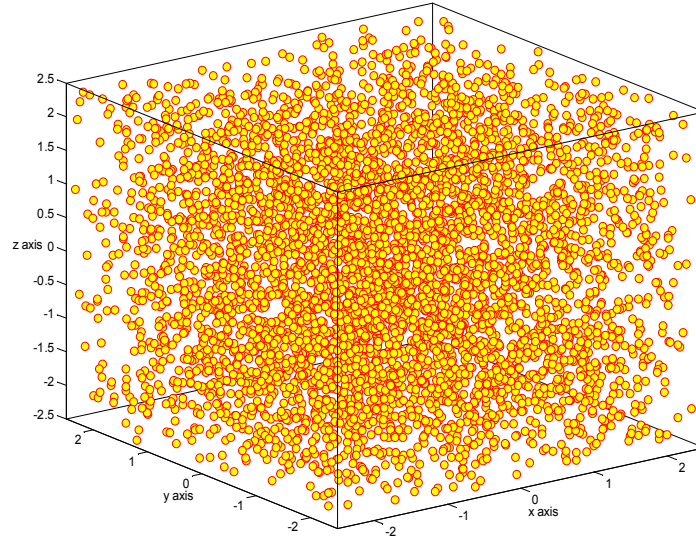
Figure 3.2 A realization of microspheres randomly located inside a cube

3.3.1 Theoretical derivation

The key assumption we will make is that the distribution of chord lengths in the

background material is exponential. This assumption will be confirmed with numerical

results later in this chapter. The following functional form for the chord length PDF may

then be written:

$$p(\lambda_1) = \frac{1}{<\lambda_1>} \cdot e^{-\lambda_1/<\lambda_1>} \tag{3.1}$$

where λ_1 is the chord length between two microspheres and $<\lambda_1>$ is the mean chord

length.
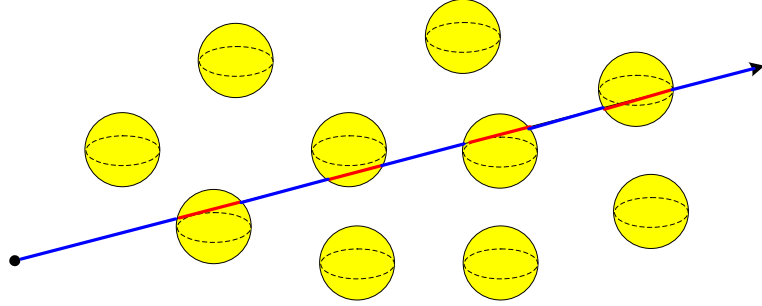
Figure 3.3 A neutron trajectory in an infinite stochastic medium

Consider a neutron trajectory that crosses N microspheres and background material regions in an infinite stochastic medium depicted in Figure 3.3. Along this trajectory, the probability the neutron is in a microsphere region is given by:

$$p_2 = \frac{N \cdot <\lambda_2>}{N \cdot <\lambda_1> + N \cdot <\lambda_2>} \qquad (3.2)$$

where $<\lambda_2>$ is the mean chord length inside a microsphere. This is identical to the volume packing fraction *frac* if the microspheres are randomly distributed in the background medium:

$$frac = \frac{<\lambda_2>}{<\lambda_1> + <\lambda_2>} \qquad (3.3)$$

Applying the Cauchy formula for the mean chord length in an arbitrary volume, $<\lambda> = 4V/S$ [34] to a microsphere with radius R, we find $<\lambda_2> = 4R/3$. Inserting this into Eq. (3.3), we find the following expression for $<\lambda_1>$:

$$<\lambda_1> = \frac{4 \cdot R}{3} \cdot \frac{1 - frac}{frac} \qquad (3.4)$$

Inserting Eq. (3.4) into Eq. (3.1), an analytical chord length PDF is obtained:

$$p(\lambda_1) = \frac{3}{4R} \cdot \frac{frac}{1 - frac} \cdot e^{-\lambda_1 \cdot \frac{3}{4R} \cdot \frac{frac}{1 - frac}} \qquad (3.5)$$

This is a general formula for the chord length PDF in the background medium as a function of the packing fraction and microsphere radius. It depends on the assumption of exponentially distributed chord lengths. An equivalent expression was derived earlier by Murata et al. [15] using the definition of the nearest neighbor distribution. Interestingly, the definitions of chord length distribution and nearest neighbor distribution are different: the former defines the distance distribution from a point on the surface of a microsphere to the surface of another microsphere, while the latter defines the distance distribution from the center of a microsphere to the center of another microsphere. The detailed description on these two concepts is explained in Torquato's book [36]. Mathematically, the equivalence between the two expressions derived using these different distribution functions is due to the exponential assumption, which underpins both expressions. Next, the accuracy of the exponential assumption is validated by direct Monte Carlo simulations.

3.3.2 Empirical estimation using Monte Carlo simulation

A cubical box representing the background material was filled with microspheres according to different packing fractions: from 5.76% (pebble-bed reactor) to 28.92% (prismatic reactor). The microsphere radius was 0.039 cm, identical to the NGNP design [2]. The fast RSA (random sequential addition) algorithm [31] was used to insert 1 million (1M) microspheres into the box for each realization, as depicted in Figure 3.2. To carry out a simulation for a single realization, 5M neutrons were emitted with a cosine current angular distribution from the cube boundary (b), 5M neutrons were emitted with a cosine current angular distribution from the surface of the microsphere (m), and 5M neutrons were emitted isotropically within the background graphite (g) region. Each

neutron was tracked to the closest microsphere, and the distance from emission to microsphere intersection was tallied. The resultant chord length histograms are the chord length PDFs for each of the three cases. We describe this approach as a direct ray-tracing simulation method, whereas other researchers have used parallel rays to tally chord length distributions [33,34].

The details of our direct ray-tracing method are described here. The Monte Carlo simulation proceeded by first using a fast RSA algorithm [31] with computational time $O(N)$ to construct a realization of a stochastic mixture of N microsphere similar to that depicted in Figure 3.2. For $f_{b \to m}(s)$, a uniform plane source is located on one side of the cube, which emits entering neutrons with a cosine angular current distribution. For $f_{m \to m}(s)$, a microsphere near the center of the cube is selected and an emission point is randomly chosen on the surface of the microsphere. An exiting neutron is then sampled with a cosine current distribution with respect to the outer normal on the microsphere. For $f_{g \to m}(s)$, an emission point is uniformly sampled within the background graphite (near the center of the cube) and a neutron is emitted isotropically. The cube was sized to ensure that the first flight escape probability was less than 10^{-5}, assuring that the PDFs represented an infinite stochastic medium. A total of 4,000 realizations were constructed and for each realization, there were 50 sampled points and 100,000 sampled directions for each point, yielding 20 billion sampled chord lengths. The chord length was determined by tracking the neutron to the next microsphere. The empirical chord length PDFs from these simulations were then compared with the theoretical PDF given in Eq. (3.5) for a range of packing fractions.

3.3.3 Comparisons with benchmark problem

Figure 3.4 presents the resultant empirical chord length PDFs at packing fractions of 5.76% and 28.92% along with the theoretical exponential PDF given in Eq. (3.5) for comparison.
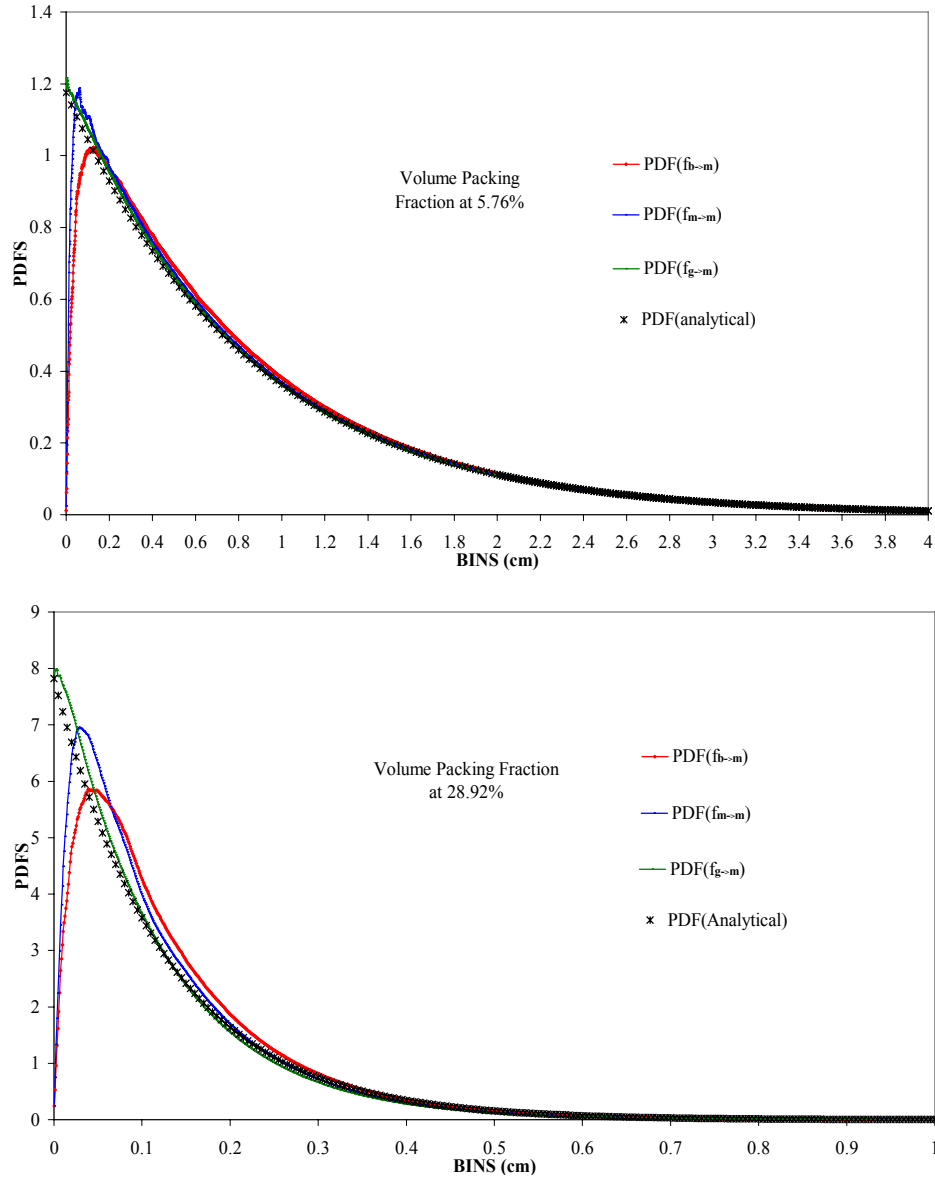
Figure 3.4 Chord length PDFs ($f_{b \to m}$, $f_{m \to m}$, and $f_{g \to m}$) for different packing fractions

It can be seen that all three PDFs approach the theoretical exponential PDF for large chord lengths. In addition, the $f_{g \to m}$ PDFs, from the graphite background region to a microsphere, are very close to the theoretical PDFs for all chord lengths and all packing fractions studied, with better agreement for smaller packing fractions. It is interesting to note that although this analytical result was derived for $f_{m \to m}$, it actually matches the results for $f_{g \to m}$ far better, as discussed below.

Both $f_{b \to m}$ and $f_{m \to m}$ deviate substantially from exponential behavior for small chord lengths. This can be explained by the observation that even if the microspheres touch the boundary (for $f_{b \to m}$) or another microsphere (for $f_{m \to m}$), they only touch at a single point, and hence the PDF must be zero at zero chord length for $f_{b \to m}$ and $f_{m \to m}$. Moreover, this "edge effect" is seen to be more pronounced for smaller packing fractions since on average the microspheres will not be as close to a boundary or to another microsphere as the packing fraction decreases. This edge effect has also been observed by other researchers [37,38]. It can be seen from the plots that the rapidly increasing initial portion of the PDFs can be approximated reasonably well by a straight line. This is a direct verification of Dirac's argument [39] that for very small chord lengths, the PDF is linear with the chord length. Based on this, a fully analytical formula can be determined by using a composite linear-exponential PDF, as long as we can determine the chord length that corresponds to the peak value.

In order to observe the long-range chord length distribution, a semi-log plot of the empirical chord length PDF as a function of packing fraction is shown in Figure 3.5, along with the theoretical PDF (dotted lines) from Eq. (3.5). The comparison between

these two sets of results shows very good agreement with improved results for smaller
packing fractions.
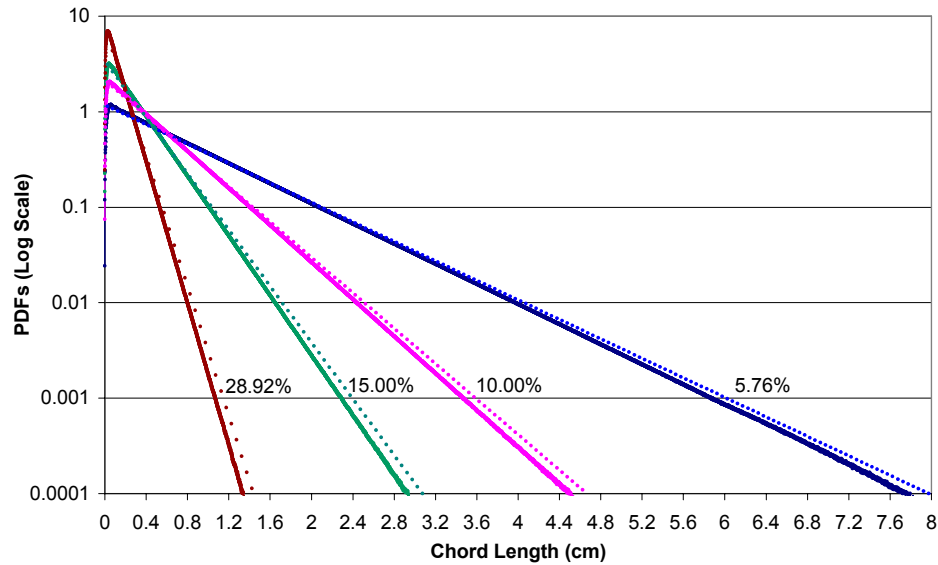
Figure 3.5 Comparison of theoretical and benchmark chord length distributions

The chord length PDF given in Eq. (3.5) was then used in the CLS method to
simulate neutron transport in a stochastic mixture of microspheres with a range of
packing fractions. The microsphere geometry is representative of TRISO fuel for the
NGNP [2]. The microsphere outer diameter is 0.78 mm and the fuel kernel diameter is
0.350 mm. The cross sections for the graphite matrix region and the microspheres were
obtained from the Brookhaven National Laboratory (BNL) website [32] for neutrons at
6.67 eV. The four microsphere coatings were homogenized into a single coating.
Although the coating region and the graphite matrix region were distinct regions for the
Monte Carlo simulation, these regions had identical cross sections obtained by
homogenizing the materials in these two regions [12].

Two types of transport problems were investigated. One is a general neutron transport simulation to evaluate leakage rates, flux integrals over different material regions, and fuel kernel absorption rates for three different geometries: a cube, a sphere, and a cylinder. The second problem is the calculation of Dancoff factors for an infinite medium and two finite medium geometries – a sphere and a finite cylinder. The following two sections will address how to solve these problems using the CLS method. The accuracy of the CLS method is established by comparison with analog Monte Carlo results.

3.4 Neutron Transport in Stochastic Media Using the CLS Method

As noted in the previous section, the CLS method is used to analyze neutron transport in a cube, a sphere, and a cylinder. The cube was simulated for a range of packing fractions from low to high. The sphere represents a fuel pebble and was simulated with a 5.76% packing fraction and the cylinder represented a fuel compact cell model and was modeled with a 28.92% packing fraction.

3.4.1 Cubical geometry

The stochastic mixture of microspheres and graphite matrix was contained in a cubical box with edge 8 cm. The microspheres were added to the box using RSA with packing fractions ranging from 5.76% to 29.8%. Incoming neutrons were emitted from a point at the center of the left side with a cosine current angular distribution, as shown in Figure 3.6.
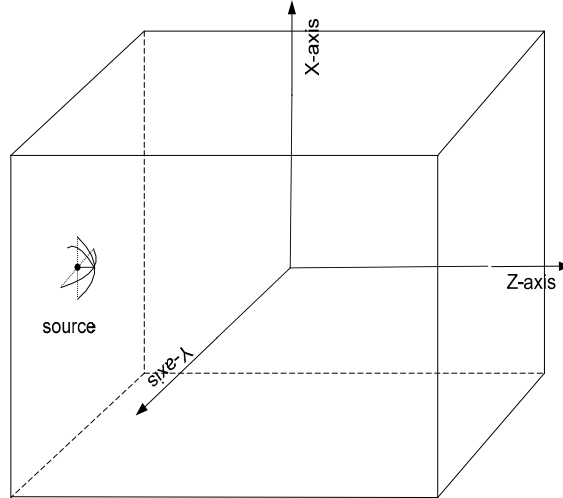
Figure 3.6 Monte Carlo simulation in cubical geometry

The average absorption rate in the microspheres and leakage rate on the left wall were tallied, along with flux integrals over the graphite matrix, coating, and fuel kernel regions. The benchmark Monte Carlo results for the cube were based on 100 realizations of the stochastic geometry with 10,000,000 particle histories per realization. These benchmark Monte Carlo results were then compared with the results using chord length sampling to analyze the stochastic mixture. The results are given in Table 3.1.

Table 3.1 The results for cubical geometry model

(graphite matrix) $\Sigma_{t,1}$=0.4137cm^{-1}, $\Sigma_{a,1}$=0.0cm^{-1}, $\Sigma_{s,1}$=0.4137cm^{-1}; (coatings) $\Sigma_{t,2}$=0.4137cm^{-1}, $\Sigma_{a,2}$=0.0 cm^{-1}, $\Sigma_{s,2}$=0.4137cm^{-1}; (fuel kernel) $\Sigma_{t,3}$=228.4cm^{-1}, $\Sigma_{a,3}$=189.7cm^{-1}, $\Sigma_{s,3}$=38.7cm^{-1}					
solution method	absorption rate $\oint_{V_3}\Sigma_a \cdot \phi(r)dr$ in fuel kernels ($\pm 1\sigma$)	reflection leakage rate via ($-z$) ($\pm 1\sigma$)	flux integral $\iiint_{V_1}\phi(r)dr$ in graphite matrix ($\pm 1\sigma$)	flux integral $\iiint_{V_2}\phi(r)dr$ in coatings ($\pm 1\sigma$)	flux integral $\iiint_{V_3}\phi(r)dr$ in fuel kernels ($\pm 1\sigma$)
volume packing fraction at 5.76%					

54

benchmark (b)	0.668 ±.001	0.229 ±.001	3.08 ±.01	0.1542 ±.0001	3.52e-3 ±.01e-3
CLS method (c)	0.667 ±.001	0.2287 ±.0001	3.129 ±.001	0.1539 ±.0001	3.51e-3 ±.01e-3
relative error (c-b)/b	-0.15%	-0.13%	1.59%	-0.19%	-0.17%
volume packing fraction at 15.00%					
benchmark (b)	0.856 ±.001	0.133 ±.001	1.38 ±.01	0.1973 ±.0001	4.51e-3 ±.01e-3
CLS method (c)	0.855 ±.001	0.1332 ±.0001	1.407 ±.001	0.1969 ±.0001	4.507e-3 ±.001e-3
relative error (c-b)/b	-0.12%	0.15%	1.96%	-0.20%	-0.07%
volume packing fraction at 20.00%					
benchmark (b)	0.8861 ±.0001	0.1101 ±.0002	1.02 ±.01	0.2043 ±.0001	4.67e-3 ±.01e-3
CLS method (c)	0.8848 ±.0001	0.1112 ± .0001	1.036 ±.0001	0.2035 ±.0001	4.66e-3 ±.01e-3
relative error (c-b)/b	-0.15%	1.00%	1.57%	-0.39%	-0.24%
volume packing fraction at 28.92%					
benchmark (b)	0.9147 ±.0001	0.085 ±.001	0.642 ±.001	0.2105 ±.0001	4.82e-3 ±.01e-3
CLS method (c)	0.9102 ±.0001	0.089 ±.001	0.665 ±.001	0.209 ±.001	4.80e-3 ±.01e-3
relative error (c-b)/b	-0.49%	4.71%	3.58%	-0.71%	-0.46%

The results in Table 3.1 show very good agreement between the CLS method and the benchmark Monte Carlo simulations for most neutron transport results. For all packing fractions, the absorption rate was within 0.50%, with no apparent dependence on

packing fraction. For the reflection leakage rates, the agreement is within 1% for the low

packing fractions and somewhat higher for high packing fractions, but it seems that the

higher relative errors occur with relatively small absolute leakage rates, such as the

reflection leakage rate for the 28.92% packing fraction. For flux integrals, less than

0.71% relative errors are obtained in the coating and fuel kernel regions for all packing

fractions, but larger relative errors occur in the graphite matrix regions.

3.4.2 VHTR cells: spherical geometry and cylindrical geometry

As a more practical application, the CLS method was used to perform a neutronic

analysis of two VHTR configurations.

Figure 3.7 illustrates the two VHTR configurations: a spherical fuel pebble for a

pebble bed VHTR and a cylindrical fuel compact for a prismatic VHTR. The CLS

simulations assume a uniform, isotropic source in the graphite regions. Vacuum boundary

conditions are assumed for all outer boundaries except for the upper and lower cylindrical

faces, which are assumed to be reflecting boundaries.

R1=2.5cm   R2=3.0cm   R=0.039cm   r=0.0175cm   Rc=0.6225cm   H=100cm   P=2.196cm

Fuel-pebble cell   TRISO fuel particle   Fuel compact cell
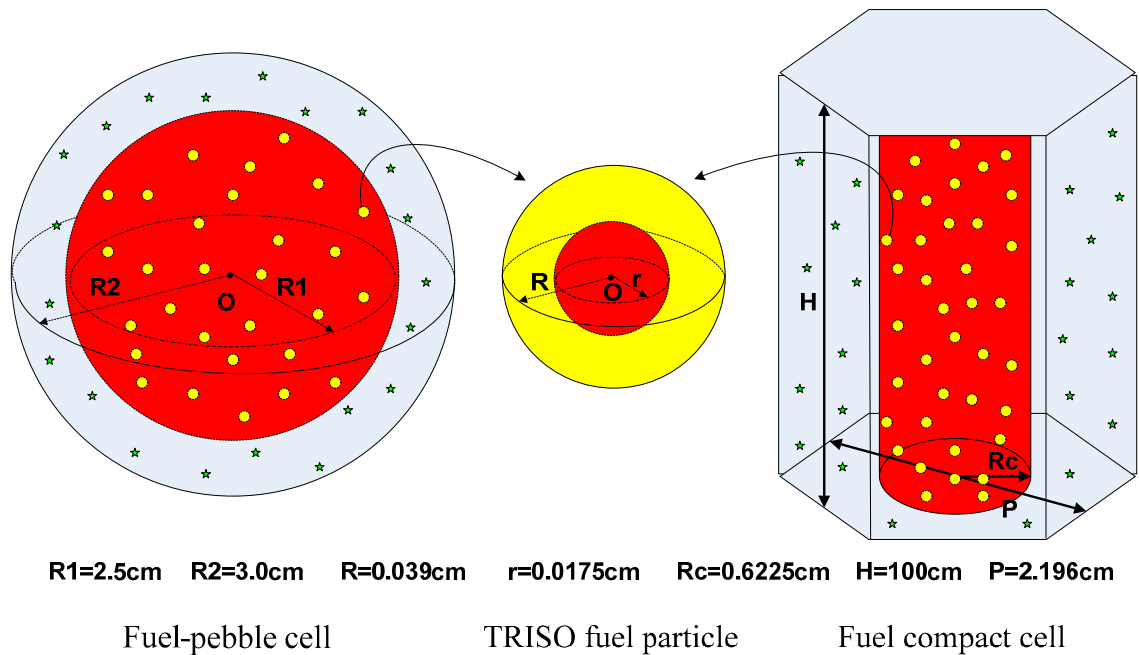
Figure 3.7 Illustration of VHTR cells and TRISO fuel particles

The average absorption rate in the microspheres and the leakage rate across the outer boundary were tallied, along with flux integrals over four regions: graphite matrix region, coating region, fuel kernel region, and graphite shell region. These benchmark Monte Carlo results were then compared with the results using chord length sampling. The benchmark Monte Carlo results were based on 100 realizations with 10,000,000 particle histories per realization.

If Eq. (3.5) is used without modification within the CLS method, the results will underestimate the resonance absorption in the fuel region and overestimate the flux integral in the non-fuel region for both unit cells as shown in Table 3.2 and Table 3.3.

A straightforward explanation for these poor estimates is that the CLS method based on Eq. (3.5) does not preserve the actual volume packing fraction. This is due to the fact that microspheres are not allowed to overlap the external boundary when the next microsphere is sampled with the CLS method, effectively reducing the packing fraction

near the boundary, hence increasing it in the interior in order to preserve the specified average packing fraction for the finite region. In order to preserve the average packing fraction, we need to replace *frac* with a higher packing fraction *frac** in Eq. (3.5):

$$p(\lambda_1) = \frac{3}{4R} \cdot \frac{frac^*}{1 - frac^*} \cdot e^{-\lambda_1 \cdot \frac{3}{4R} \cdot \frac{frac^*}{1 - frac^*}}. \tag{3.6}$$

Murata et al.[15,16] first noticed this boundary interference and suggested a simple way to obtain *frac** by shrinking the stochastic region away from each surface by a distance *t=R*, the microsphere radius, which leads to *frac*= (V/V*)•frac*, where V is the original volume and *V** is the reduced volume. The choice of *R* is motivated physically by noting that the center of a microsphere cannot be placed within *R* of a boundary. This higher packing fraction *frac** was then used with CLS and the results showed very good agreement with benchmark results in criticality calculations.

However, when Murata's boundary correction method is used in a general transport computation, the results were not always satisfactory, depending on the geometry, packing fraction, and microsphere radius. So shrinking the stochastic volume may give a first order correction but does not seem to work in general. As a result, an alternative approach to compute *frac** was developed.

Since the packing fraction is only a function of geometry and not a function of material composition, the CLS method can be used to compute the packing fraction for the given geometry by performing a special simulation that assumes all regions are voided and using the track length estimator to estimate the volumes of the microsphere and background regions. This yields the effective packing fraction for this geometry as experienced by the CLS method. This effective packing fraction is the actual packing

fraction seen by the CLS method for that geometry and the idea is to force this to equal the specified packing fraction. This is done by changing the input packing fraction for the special CLS calculation until the resulting packing fraction equals the desired packing fraction. This input packing fraction is then used in the actual CLS simulation of the stochastic geometry. The special CLS calculation is performed with a monodirectional plane source on one side of the stochastic geometry with all internal regions voided. This is done for both the cylindrical and spherical VHTR cells.

Table 3.2 and Table 3.3 show the results using the CLS method to simulate both a fuel pebble and a fuel compact. The CLS results are tallied for three different choices of the corrected packing fraction to account for the external boundary – no correction, Murata's correction, and the proposed correction scheme discussed above. The results contained in Table 3.2 show that both Murata's scheme and the new correction scheme improve the results compared to no correction. Other cases have also been analyzed that are not reported here, but the results show that in general the new iteration scheme yields better results than Murata's scheme for most cases except for the fuel pebble with a low packing fraction.

Table 3.2 Transport analysis in a VHTR fuel pebble cell

(graphite) $\Sigma_{t,4}$=0.4137cm^{-1}, $\Sigma_{a,4}$=0.0cm^{-1}, $\Sigma_{s,4}$=0.4137cm^{-1};						
(matrix) $\Sigma_{t,1}$=0.4137cm^{-1}, $\Sigma_{a,1}$=0.0cm^{-1}, $\Sigma_{s,1}$=0.4137cm^{-1};						
(coatings) $\Sigma_{t,2}$=0.4137cm^{-1}, $\Sigma_{a,2}$=0.0 cm^{-1}, $\Sigma_{s,2}$=0.4137cm^{-1};						
(fuel kernel) $\Sigma_{t,3}$=228.4cm^{-1}, $\Sigma_{a,3}$=189.7cm^{-1}, $\Sigma_{s,3}$=38.7cm^{-1}						
packing fractions	methods	absorption rate in kernels	leakage rate	flux integral in matrix	flux integral in coatings	flux integral in kernels

	benchmark	0.154	0.846	0.6712	0.0356	8.12E-04
	CLS based on Eq. (3.5)	0.1475	0.8524	0.7100	0.0341	7.77E-04
	relative error	**-4.22%**	**0.76%**	**5.78%**	**-4.21%**	**-4.31%**
5.76%	CLS with Murata's scheme	0.152	0.8479	0.6955	0.03517	8.01E-04
	relative error	**0.63%**	**-0.21%**	**3.27%**	**0.72%**	**0.63%**
	CLS with iteration scheme	0.1496	0.8504	0.7034	0.03461	7.88E-04
	relative error	**-2.86%**	**0.52%**	**4.80%**	**-2.78%**	**-2.96%**
	benchmark	0.2806	0.7194	0.1984	0.0647	1.48E-03
	CLS based on Eq. (3.5)	0.2794	0.7204	0.2111	0.0647	1.47E-03
	relative error	**-0.43%**	**0.14%**	**6.40%**	**0.00%**	**-0.41%**
28.92%	CLS with Murata's scheme	0.2814	0.7183	0.1995	0.0652	1.48E-03
	relative error	**0.29%**	**-0.15%**	**0.55%**	**0.77%**	**0.27%**
	CLS with iteration scheme	0.2804	0.7195	0.2065	0.0649	1.48E-03
	relative error	**-0.07%**	**0.01%**	**4.08%**	**0.31%**	**-0.14%**

Table 3.3 Transport analysis in a VHTR compact cell

(graphite) $\Sigma_{t,4}$=0.4137cm^{-1}, $\Sigma_{a,4}$=0.0cm^{-1}, $\Sigma_{s,4}$=0.4137cm^{-1};					
(matrix) $\Sigma_{t,1}$=0.4137cm^{-1}, $\Sigma_{a,1}$=0.0cm^{-1}, $\Sigma_{s,1}$=0.4137cm^{-1};					
(coatings) $\Sigma_{t,2}$=0.4137cm^{-1}, $\Sigma_{a,2}$=0.0 cm^{-1}, $\Sigma_{s,2}$=0.4137cm^{-1};					
(fuel kernel) $\Sigma_{t,3}$=228.4cm^{-1}, $\Sigma_{a,3}$=189.7cm^{-1}, $\Sigma_{s,3}$=38.7cm^{-1}					
packing fractions	methods	absorption rate in kernels	leakage rate	flux integral in	flux integral in	flux integral in kernels

				matrix	coatings	
	benchmark	0.0692	0.9308	0.3244	0.01598	3.65E-04
	CLS based on Eq. (3.5)	0.065	0.9351	0.3311	0.01501	3.43E-04
	relative error	**-6.07%**	**0.46%**	**2.07%**	**-6.07%**	**-6.03%**
5.76%	CLS with Murata's scheme	0.0724	0.9276	0.3213	0.01677	3.81E-04
	relative error	**4.62%**	**-0.34%**	**-0.96%**	**4.94%**	**4.38%**
	CLS with iteration scheme	0.0692	0.9309	0.3254	0.016	3.65E-04
	relative error	**0.00%**	**0.01%**	**0.31%**	**0.13%**	**0.00%**
	benchmark	0.2002	0.7997	0.1423	0.0462	1.06E-03
	CLS based on Eq. (3.5)	0.1948	0.8052	0.1526	0.0454	1.03E-03
	relative error	**-2.70%**	0.69%	7.24%	-1.73%	**-2.65%**
28.92%	CLS with Murata's scheme	0.2061	0.7942	0.1347	0.048	1.09E-03
	relative error	2.95%	-0.69%	-5.34%	3.90%	**2.94%**
	CLS with iteration scheme	0.1992	0.8008	0.1456	0.04638	1.05E-03
	relative error	**-0.50%**	**0.14%**	**2.32%**	**0.39%**	**-0.47%**

3.4.4 Backscattering correction

We have considered an extension to the CLS method for the analysis of TRISO fuel to account for the fact that a neutron exiting a microsphere in a highly scattering medium will have a reasonable probability of scattering back into the same microsphere. This was accounted for in our CLS method by "remembering" the last microsphere the

neutron exited and including its boundary as a potential surface to be tracked to along the sampled chord length. If a neutron enters a microsphere, this memory is erased. This results in an improvement in the range of 0.1% to 2.0% depending on the specific configuration. Normally, for cases with low scattering cross sections ($<1.0\text{cm}^{-1}$) in background material, the correction is very small ($< 0.5\%$); however, for cases with high scattering cross sections ($>1.0\text{cm}^{-1}$), the backscatter correction can approach 2.0%.

3.5 Dancoff Factor Computation Using CLS Method

The Dancoff factor is an important quantity that is needed in most reactor design lattice codes, including those used for VHTR analysis. It is important to have an efficient and accurate method for computing the Dancoff factor for TRISO fuel and this section will discuss the application of CLS to compute this quantity. A general definition of the Dancoff factor for TRISO fuel is the average probability that a neutron escaping from an absorber (fuel kernel) enters another absorber (fuel kernel) without having a collision in the moderator between. In this section, we apply the CLS method to calculate the Dancoff factor for an infinite medium of TRISO fuel, as well as a finite sphere and a finite cylinder, corresponding to a fuel pebble and a fuel compact, respectively. The predictions of the Dancoff factor are compared with results from analog Monte Carlo benchmark simulations.

Two distinct models were developed for the application of CLS to calculate Dancoff factors for TRISO fuel: single-sphere model and dual-sphere model. In each model, neutron emission is assumed to be uniformly distributed on the surface of the exiting fuel kernel with a cosine current distribution. However, the random walk process for each neutron is different. The dual-sphere model is based on Eq. (3.5): the distance to

the next microsphere fuel particle is sampled and neutrons are tracked through the coating regions until the neutron enters the kernel (and is tallied) or undergoes a collision, at which point the history is terminated. The single-sphere model treats the fuel kernels as stochastically distributed, rather than the microspheres, by homogenizing the coating regions with the graphite matrix region. Thus, the next fuel kernel is sampled during a random walk and the neutrons reaching the next fuel kernel without collision are tallied. In this case, the chord length sampling PDF is based on the following:

$$p(\lambda) = \frac{3}{4r} \cdot \frac{frac \cdot (r/R)^3}{1 - frac \cdot (r/R)^3} \cdot e^{-\lambda \cdot \frac{3}{4r} \cdot \frac{frac \cdot (r/R)^3}{1 - frac \cdot (r/R)^3}}, \tag{3.7}$$

where r is the radius of fuel kernel and R is the radius of the TRISO fuel particle. Equation (3.7) is easily derived from Eq. (3.5) by changing the packing fraction to be the ratio of the fuel kernel volume to the total volume, rather than the ratio of the microsphere volume to the total volume.

A comparison of the two models, based on either Eq. (3.5) or Eq. (3.7), was performed by first computing infinite medium Dancoff factors at different volume packing fractions. Then finite medium Dancoff factors based on the two approaches were compared for a finite sphere and a finite cylinder, representative of a fuel pebble and a fuel compact, respectively.

3.5.1 Infinite medium Dancoff factors

The infinite medium Dancoff factors were computed for a cubical geometry large enough to simulate resonance energy neutron transport in an infinite stochastic medium. Depending on the packing fraction, approximately 15-30 million TRISO fuel kernels were dispersed randomly in a matrix graphite background region using the RSA

algorithm. Neutrons were emitted uniformly from the surface of fuel kernels with a cosine angular current distribution. The number of neutrons that successfully reach another fuel kernel without having a collision in the coating and matrix graphite regions was tallied, and the Dancoff factor was computed as the ratio of this number to the total number of neutrons emitted. A total of 100 physical realizations were performed, and 10M neutrons were emitted per realization. The final Dancoff factor was ensemble-averaged over the 100 realizations. The results are listed in Table 3.4 and compared with benchmark results from an analog Monte Carlo simulation. As in the previous simulations, cross sections are based on 6.67 eV neutrons, and the geometry and composition of the microspheres and graphite matrix are based on the NGNP design.

Table 3.4 Infinite medium Dancoff factors

volume packing fractions	benchmark ($\pm1\sigma=0.0001$)	CLS with dual-sphere model ($\pm1\sigma=0.0001$)	relative error	CLS with single-sphere model ($\pm1\sigma=0.0001$)	relative error
5.76%	**0.3478**	**0.3469**	**-0.26%**	**0.3515**	**1.06%**
10.00%	**0.4820**	**0.4806**	**-0.29%**	**0.4857**	**0.77%**
15.00%	**0.5838**	**0.5825**	**-0.22%**	**0.5874**	**0.62%**
20.00%	**0.6527**	**0.6516**	**-0.17%**	**0.6559**	**0.49%**
25.00%	**0.7029**	**0.7014**	**-0.21%**	**0.7054**	**0.36%**
28.92%	**0.7325**	**0.7318**	**-0.10%**	**0.7354**	**0.39%**

Both CLS methods based on single-sphere model and dual-sphere model give very good agreement with the benchmark results. All the relative errors are within an absolute value of 1.06%. The dual-sphere model gives a somewhat more accurate result for all packing fractions; however, the simulation using the single-sphere model is about

three times faster than the first model. It is interesting to note that the dual-sphere model, based on tracking to microspheres, underestimates the Dancoff factor for all packing fractions, while the single-sphere model, based on tracking to fuel kernels, overestimates the Dancoff factor, again for all packing fractions.

Let us now consider a finite sphere and a finite cylinder, both filled with TRISO microspheres that are analyzed with CLS using the two models discussed above. For these finite geometries, the first flight escape probability is computed as well as the Dancoff factors. The first-flight escape probability is defined as the average probability that a neutron leaving an absorber (fuel kernel) will escape the finite sphere or cylinder without having a collision in the moderator and without entering another absorber (fuel kernel).

Since this is a finite medium, the packing fraction correction due to the overlapping of microspheres on the external boundary needs to be applied. Therefore, the dual-sphere CLS model will make use of Eq. (3.6), which accounts for this effect. The single-sphere CLS model for the finite geometry, corresponding to Eq. (3.7) for the infinite geometry case, should also be corrected for boundary overlapping, resulting in:

$$p(\lambda) = \frac{3}{4r} \cdot \frac{frac^* \cdot (r/R)^3}{1 - frac^* \cdot (r/R)^3} \cdot e^{-\lambda \cdot \frac{3}{4r} \cdot \frac{frac^* \cdot (r/R)^3}{1 - frac^* \cdot (r/R)^3}}. \tag{3.8}$$

Eq. (3.8) is used as the PDF in the single-sphere CLS method for the first flight escape probability and Dancoff factor calculations. The same iteration scheme was used as in the previous section to determine the corrected packing fraction $frac^*$ in Eq. (3.8).

For both models, a microsphere was sampled before the CLS simulation proceeds. The center of the microsphere was assumed to be uniformly distributed inside the finite medium, excluding the volume with a distance R to the medium boundary. Neutrons were

then emitted at the surface of the fuel kernel in that sampled microsphere with a cosine current distribution.

In both geometries, the analog Monte Carlo benchmark results are based on 100 physical realizations of the medium filled with randomly distributed TRISO fuel kernels. There are 10M neutron emissions per realization. The final Dancoff factor is ensemble-averaged over the 100 realizations.

3.5.2 Intra-Dancoff factors and first-flight escape probabilities in spherical geometry

The Dancoff factors for the finite spheres (also called intra-pebble Dancoff factor) are calculated using CLS with single-sphere and dual-sphere models, and are shown in Figure 3.8 and Table 3.5, along with Monte Carlo benchmark results.
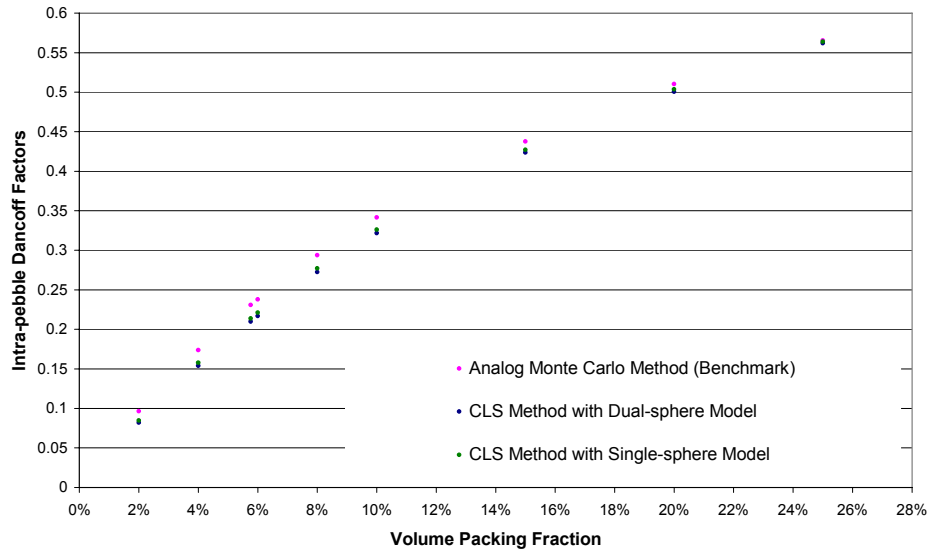
Figure 3.8 Comparison between CLS and analog Monte Carlo methods on intra-Dancoff factors in spherical geometry

Table 3.5 Intra-Dancoff factors in spherical geometry

volume packing fractions	benchmark (±1σ=0.001)	CLS with dual-sphere model (±1σ=0.001)	relative error	CLS with single-sphere model (±1σ=0.001)	relative error
2.00%	**0.097**	**0.082**	**-14.92%**	**0.085**	**-12.02%**
4.00%	**0.174**	**0.154**	**-11.51%**	**0.158**	**-9.27%**
5.76%	**0.231**	**0.210**	**-9.10%**	**0.214**	**-7.32%**
6.00%	**0.238**	**0.217**	**-8.91%**	**0.221**	**-7.14%**
8.00%	**0.294**	**0.273**	**-7.18%**	**0.277**	**-5.69%**
10.00%	**0.342**	**0.322**	**-5.77%**	**0.326**	**-4.54%**
15.00%	**0.438**	**0.424**	**-3.20%**	**0.427**	**-2.38%**
20.00%	**0.510**	**0.500**	**-1.90%**	**0.504**	**-1.27%**
25.00%	**0.566**	**0.562**	**-0.64%**	**0.564**	**-0.30%**

Both models, which are based on Eq. (3.6) and Eq. (3.8), give approximately the same results, with slightly better results with the single-sphere model. However, the poor agreement with the benchmark results at low packing fractions, greater than 9% relative error at 5.76% packing fraction, implies there may be other factors having a dominant impact on the Dancoff factor calculations. Some of these possible factors are explored in Chapter 5, and more work needs to be done to understand this in the future. As seen with the infinite medium cases, the simulation process using the single-sphere CLS model is three times faster than with the dual-sphere CLS model since there is no need to track within the layers and there are fewer collisions with kernels that with microspheres.

The first-flight escape probability results calculated using the two CLS models are shown in Figure 3.9 and Table 3.6, along with the Monte Carlo benchmark results.
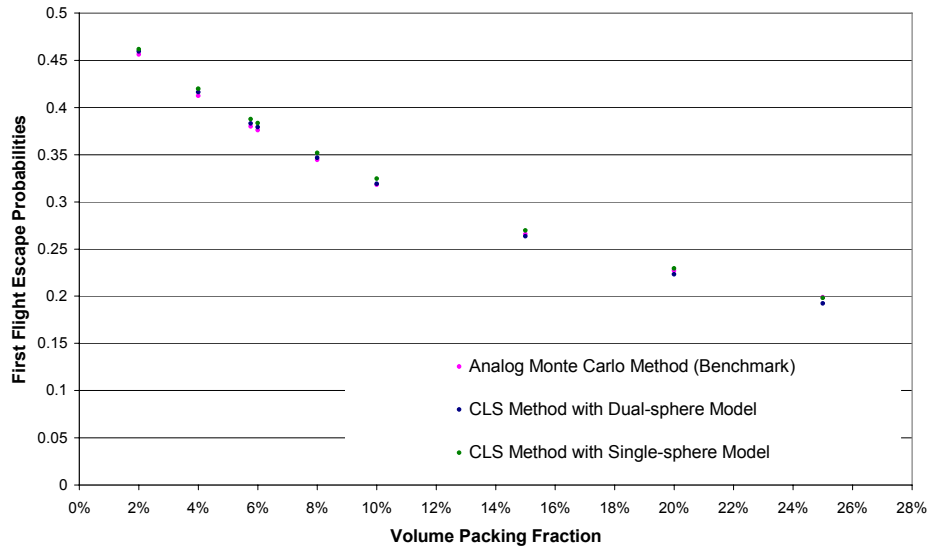
Figure 3.9 Comparison between CLS and analog Monte Carlo methods on first-flight
escape probabilities in spherical geometry

Table 3.6 First-flight escape probabilities in spherical geometry

volume packing fractions	benchmark ($\pm 1\sigma$=0.001)	CLS with dual-sphere model ($\pm 1\sigma$=0.001)	relative error	CLS with single-sphere model ($\pm 1\sigma$=0.001)	relative error
2.00%	0.456	0.460	0.70%	0.462	1.18%
4.00%	0.412	0.416	0.92%	0.420	1.77%
5.76%	0.380	0.383	0.84%	0.388	2.00%
6.00%	0.376	0.379	0.85%	0.384	1.99%
8.00%	0.344	0.347	0.73%	0.352	2.24%
10.00%	0.318	0.319	0.22%	0.325	1.98%
15.00%	0.266	0.264	-0.90%	0.270	1.47%
20.00%	0.227	0.223	-1.72%	0.229	0.97%
25.00%	0.199	0.192	-3.22%	0.198	-0.25%

Generally, the dual-sphere model gives better results for packing fractions less than 20%, while the single-sphere model yields better results for packing fractions of 20% and higher.

3.5.3 Intra-Dancoff factors and first-flight escape probabilities in cylindrical geometry

The Dancoff factors for a finite cylinder (the intra-compact Dancoff factor) calculated using CLS methods with single-sphere and dual-sphere models are shown in Figure 3.10 and Table 3.7, along with the comparisons to analog Monte Carlo benchmark results.
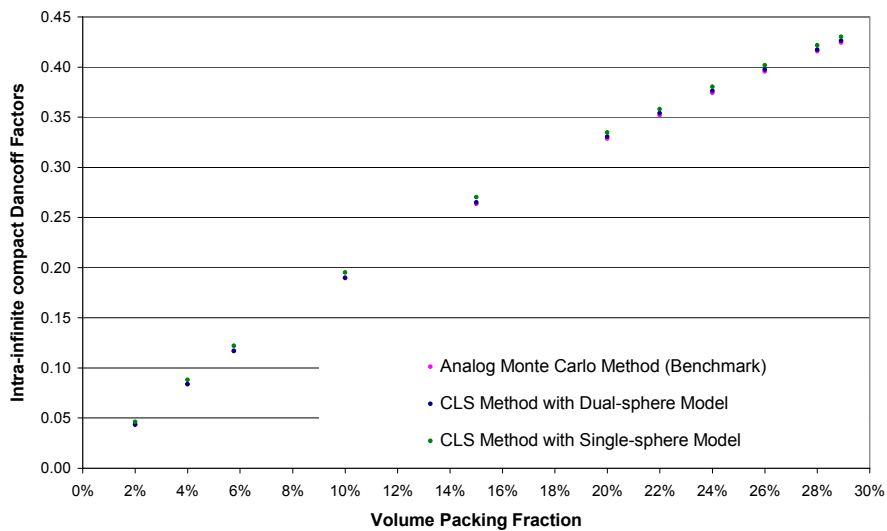
Figure 3.10 Comparison between CLS and analog Monte Carlo methods on intra-Dancoff factors in cylindrical geometry

Table 3.7 Intra-Dancoff factors in cylindrical geometry

volume packing fractions	benchmark ($\pm 1\sigma$=0.001)	CLS with dual-sphere model ($\pm 1\sigma$=0.001)	relative error	CLS with single-sphere model ($\pm 1\sigma$=0.001)	relative error
2.00%	0.0435	0.0434	-0.23%	0.0462	6.21%
4.00%	0.0838	0.0837	-0.12%	0.0880	5.01%
5.76%	0.1170	0.1169	-0.09%	0.1220	4.27%
10.00%	0.1896	0.1899	0.16%	0.1949	2.80%
15.00%	0.2634	0.2652	0.68%	0.2701	2.54%
20.00%	0.3286	0.3306	0.61%	0.3349	1.92%
22.00%	0.3518	0.3539	0.60%	0.3581	1.79%
24.00%	0.3741	0.3762	0.56%	0.3802	1.63%
26.00%	0.3957	0.3975	0.45%	0.4018	1.54%
28.00%	0.4159	0.4173	0.34%	0.4215	1.35%
28.92%	0.4244	0.4261	0.40%	0.4301	1.34%

The results in Table 3.7 show excellent agreement between the CLS method and the benchmark Monte Carlo simulations for the dual-sphere model. For all packing fractions, the Dancoff factors are within absolute relative error of 0.68%, with no apparent dependence on packing fraction. The single-sphere model results show poor agreement at low packing fractions but reasonable agreement at high packing fractions, but still substantially inferior to the results obtained with the microsphere model.

The first-flight escape probability for the finite cylinder is also calculated using the two CLS models, and the results are shown in Figure 3.11 and Table 3.8.
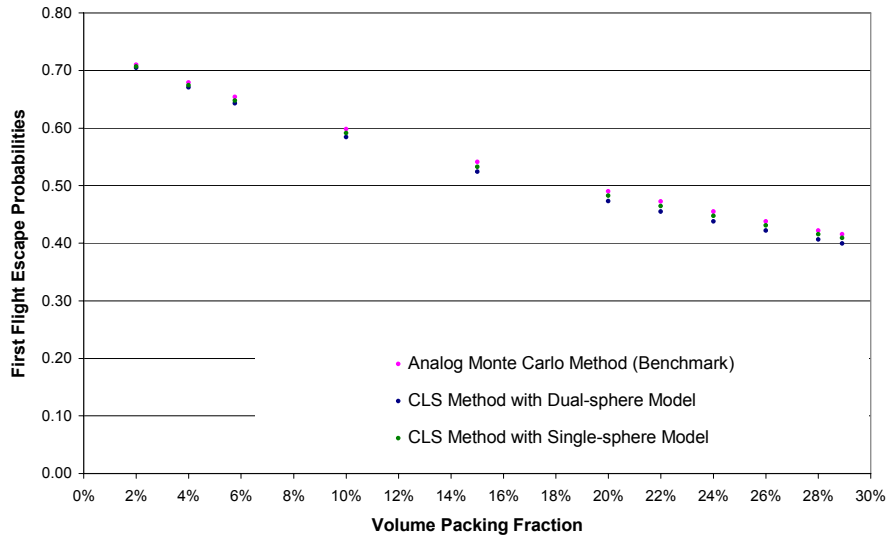
Figure 3.11 Comparison between CLS and analog Monte Carlo methods on first-flight escape probabilities in cylindrical geometry

Table 3.8 First-flight escape probabilities in cylindrical geometry

volume packing fractions	benchmark ($\pm 1\sigma$=0.001)	CLS with dual-sphere model ($\pm 1\sigma$=0.001)	relative error	CLS with single-sphere model ($\pm 1\sigma$=0.001)	relative error
2.00%	**0.7098**	**0.7048**	**-0.70%**	**0.7068**	**-0.42%**
4.00%	**0.6792**	**0.6707**	**-1.25%**	**0.6744**	**-0.71%**
5.76%	**0.6538**	**0.6431**	**-1.64%**	**0.6478**	**-0.92%**
10.00%	**0.5980**	**0.5842**	**-2.31%**	**0.5910**	**-1.17%**
15.00%	**0.5413**	**0.5242**	**-3.16%**	**0.5328**	**-1.57%**
20.00%	**0.4901**	**0.4732**	**-3.45%**	**0.4823**	**-1.59%**
22.00%	**0.4722**	**0.4550**	**-3.64%**	**0.4644**	**-1.65%**
24.00%	**0.4547**	**0.4379**	**-3.69%**	**0.4473**	**-1.63%**
26.00%	**0.4378**	**0.4216**	**-3.70%**	**0.4308**	**-1.60%**
28.00%	**0.4220**	**0.4064**	**-3.70%**	**0.4156**	**-1.52%**
28.92%	**0.4155**	**0.3997**	**-3.80%**	**0.4090**	**-1.56%**

Contrary to the Dancoff factor computations, the results in Table 3.8 show better results for the single-sphere CLS method, with smaller errors by a factor of two for the dual-sphere model method for all packing fractions.

CHAPTER 4

Application of Chord Method to Dancoff-factor Calculations in Double

Heterogeneous Stochastic Media

4.1 Introduction

When neutrons slow down into the resonance energy range in the moderator, they

may be absorbed by fuel kernels (called "fuel absorbers") before having their next

collision with the moderator. For a single fuel absorber, this resonance absorption is

reduced by a certain amount due to the existence of adjacent absorbers. This is because

the neighboring absorbers would block the path of resonance neutrons to the fuel

absorber in question, reducing the probability that those resonance neutrons will reach

that absorber without colliding with a moderator. This effect is equivalent to increased

self-shielding and is called the "shadowing effect" in many references [40,41]. The

earliest paper on this topic that could be found by the author is the classic report by

Dancoff and Ginsburg in 1944 [42]. They derived a formula to calculate the reduction in

surface resonance absorption due to neighboring absorbers, and this reduction is known

as the "Dancoff-Ginsburg factor" or "Dancoff factor" [41,43].

The Dancoff factor plays an important role in calculating collision probabilities

and resonance integrals for reactor fuel lattices [44,45,46].

In the Very High Temperature Gas-cooled Reactor (VHTR) analysis, it is

essential to generate accurate few-group cross sections for use in global reactor

calculations [3]. In particular, one needs to account for the stochastic distribution and double heterogeneity of the TRISO particle fuel in order to obtain reasonable few-group cross sections, especially in the resonance energy range. While general purpose Monte Carlo codes such as MCNP5 [9] can analyze VHTR configurations from unit cell calculations to full-core with excellent results [12,21,25,29], the computational time is prohibitive, especially if one considers depletion and feedback effects. As a result, the conventional methodology is based on deterministic transport methods such as MICROX-2 [47] that include user-specified Dancoff factors to account for the double heterogeneity. These Dancoff factors may be calculated by Monte Carlo or semi-analytical/analytical methods [48,49,50]. In this section, we discuss several methods that are used to compute Dancoff factors, and we derive an analytical formula for the Dancoff factor based on the chord length PDF that we have developed in the previous chapter. Closed form expressions for the Dancoff factor have been obtained for infinite stochastic geometry, for an infinite cylinder, and for a finite sphere. Closed form expressions have also been obtained for finite configurations of infinite cylinders and spheres, but these expressions include probabilities that need to be evaluated empirically due to the complexity of analyzing these finite geometries.

In recent years, three papers [48,49,50] were published on analytical calculations of Dancoff factors for pebble-bed and prismatic type reactors. These include (1) infinite medium Dancoff factors, (2) finite medium Dancoff factors for an isolated fuel pebble or fuel compact (intra-pebble or intra-compact), and (3) finite medium Dancoff factors for a collection of fuel pebbles or fuel compacts (inter-pebble and inter-compact), including accounting for the coating region in a TRISO fuel particle [50]. In all of these works

regarding analytical expressions for Dancoff factors, the derivations are based on complicated integrations over surfaces and angles which can be avoided by using a chord length PDF, as discussed next.

In this chapter, a general formulation of the Dancoff factor is given following Dancoff and Ginsburg's original procedure [42]. In this derivation, the Dancoff factor is expressed in a simple form by introducing a chord length distribution function as Dirac did when he studied neutron multiplication [39]. This expression avoids the double integral evaluation performed by Dancoff and Ginsburg, but one needs to know the chord length distribution function, which we have previously determined.

The new expression for the Dancoff factor was applied to the calculation of Dancoff factors for TRISO fuel in a VHTR. Two fuel particle models were investigated: single-sphere and dual-sphere models, which correspond roughly to either treating the fuel kernel by itself (single sphere) or the fuel kernel and fuel microsphere together (dual sphere). Analytical formulas for the Dancoff factor are derived for both models using the analytical chord length PDFs derived in Chapter 2. These formulas are used to compute Dancoff factors for an infinite medium and for finite medium configurations representative of both pebble-bed and prismatic type VHTRs. The numerical results from these formulas are compared with Monte Carlo benchmark results and the agreement is good:

o   within 1.1% relative error for infinite medium Dancoff factors

o   within 7.7% relative error for intra-pebble Dancoff factors

o   within 1.5% for intra-compact Dancoff factors

o   within 0.8% relative error for inter-pebble Dancoff factors

o   within 0.5% for inter-compact Dancoff factors

In addition, the actual chord length PDF between two fuel kernels was calculated by direct Monte Carlo simulation using RSA algorithms [24,31]. This empirical PDF replaced our analytical chord length PDF to calculate the Dancoff factors. Agreements to within 0.30% relative error compared to benchmark results indicates that the chord length methodology is being applied correctly.

4.2 General Formulation for Dancoff Factor

In this section, the general formulation of the Dancoff factor for a single fuel lump in an infinite medium is given, along with extensions of the theory to treat finite media with multiple fuel regions. The derivations are applicable to fuel lumps, which have arbitrary shapes and are uniformly dispersed in a background moderator with arbitrary packing schemes.

4.2.1 Dancoff factor of a single fuel lump in an infinite medium

We consider the situation in which fuel lumps with arbitrary (non-reentrant) shapes are dispersed randomly in a background moderator. Fission neutrons are generated inside the fuel lumps and are slowed down in the moderator. After several scatterings in the moderator, some of the neutrons may enter the resonance energy range and be absorbed. To model this, a uniform, isotropic source of resonance-energy neutrons is assumed in the moderator.

Given the source density Q neutrons/cm^3-s at a point $\vec{r}'$ in the moderator, the uncollided flux at the surface point $\vec{r}$ of a fuel lump due to that source is:

$$\Psi(\vec{r}' \to \vec{r}) = Q \cdot \frac{e^{-|\vec{r}-\vec{r}'|/\lambda}}{4\pi |\vec{r}-\vec{r}'|^2}, \tag{4.1}$$

where λ is the mean free path of resonance neutrons in the moderator and it is assumed that no other fuel lump is between $\vec{r}'$ and $\vec{r}$, i.e. $\vec{r}'$ and $\vec{r}$ can see each other only through the moderator region. The rate that neutrons enter the fuel lump through a small surface element dA at $\vec{r}$ is:

$$J(\vec{r}' \to \vec{r}) = \Psi(\vec{r}' \to \vec{r})\cos\theta dA = Q \cdot \frac{e^{-|\vec{r}-\vec{r}'|/\lambda}}{4\pi |\vec{r}-\vec{r}'|^2}\cos\theta dA, \tag{4.2}$$

where θ is the angle between $\vec{r}-\vec{r}'$ and the outer normal of dA. The total rate that neutrons enter a fuel lump without colliding with the moderator is:

$$J = \iint J(\vec{r}' \to \vec{r})dAd^3\vec{r}' = \frac{Q}{4\pi}\int dA\cos\theta\int d^3\vec{r}'\frac{e^{-|\vec{r}-\vec{r}'|/\lambda}}{4\pi |\vec{r}-\vec{r}'|^2}. \tag{4.3}$$

Now using a spherical coordinate transformation $d^3\vec{r}' = s^2 ds d\Omega$ where $\vec{r}$ is the origin, $s = |\vec{r}-\vec{r}'|$, and $d\Omega$ is a solid angle element about direction (θ, φ), we get:

$$J = \frac{Q}{4\pi}\int dA\int d\Omega\cos\theta\int_0^l e^{-s/\lambda}ds = \frac{Q\lambda}{4\pi}\int dA\int d\Omega\cos\theta(1-e^{-l/\lambda}), \tag{4.4}$$

where l is the length of the chord through the point $\vec{r}$ in the direction (θ, φ) to the surface of an adjacent fuel lump. After simple manipulation, Eq. (4.4) can be written as:

$$J = \frac{Q\lambda A}{4}\left[1 - \frac{\int dA\int d\Omega\cos\theta(e^{-l/\lambda})}{\int dA\int d\Omega\cos\theta}\right], \tag{4.5}$$

where *A* is the total surface area of the recipient fuel lump. This is the equation Dancoff

and Ginsburg obtained in their paper [42]. Now it can be easily seen that the first part in

Eq. (4.5) is the total rate that resonance neutrons enter the fuel lump if only one fuel lump

exists in the moderator. The second part is the reduction in the entering rate due to

neighboring lumps. The complicated second term in the bracket is called the Dancoff

factor *C*, which is the fractional reduction in surface resonance absorption due to the

presence of the neighboring fuel regions:

$$C = \frac{\int dA \int d\Omega \cos\theta (e^{-l/\lambda})}{\int dA \int d\Omega \cos\theta}. \tag{4.6}$$

Next, we introduce the probability density function for the distribution of chord

lengths in the moderator region, as Dirac did when he studied neutron multiplication for a

solid of arbitrary shape [39]. According to Dirac, the chord length distribution PDF *f(l)* is

defined such that for any function *g(l)*:

$$\int f(l)g(l)dl = \frac{\int dA \int d\Omega \cos\theta [g(l)]}{\int dA \int d\Omega \cos\theta}. \tag{4.7}$$

Then Eq. (4.6) becomes:

$$C = \int f(l)e^{-l/\lambda}dl. \tag{4.8}$$

The relative simplicity of Eq. (4.8) versus Eq. (4.6) is clear – the 4D integral over

surface and angle has been replaced by a 1D integral over the chord length distribution.

This expression for the Dancoff factor in terms of the chord length PDF was first

published by Sauer [53] in 1963, but with somewhat different notation. A similar result

for the first flight escape probability was given by Case et al. [51] in 1953 but no mention

was made of the Dancoff factor. In spite of these early references, there has been

essentially no mention of the use of chord length PDFs for the calculation of Dancoff factors in stochastic media in the past 40 years, even though many papers have been published on the calculation of Dancoff factors for TRISO fuel [45,48,49,50,65].

As a result of Eq. (4.8), the calculation of the Dancoff factor is reduced to determining the chord length PDF between two fuel lumps in the moderator. However, we have already found an analytical expression for the chord length PDF in Chapter 2, which we will use to determine the Dancoff factor.

Dancoff also derived Eq. (4.4) and performed the double integral over two fuel lump surfaces to obtain the second part. However, the chord method introduced in Eqs. (4.5) to (4.8) can decrease the computation cost, which is normally high for the double integral, and can be applied to media with any geometry distribution such as the stochastic distribution of fuel lumps in a VHTR.

Also, Eq. (4.8) yields another physical explanation for the Dancoff factor. The original derivation was based on the physical assumption that resonance neutrons are created uniformly in the moderator and reach a fuel lump without collision. However, Eq. (4.8) suggests another physical interpretation. If resonance neutrons are emitted from the surface of a fuel lump and travel through the moderator towards another fuel lump, then $f(l)dl$ is the probability that the distance to the next fuel lump is within (l, $l+dl$) and $e^{-l/\lambda}$ is the probability that the neutron traverses the distance l without a collision. In this sense, the Dancoff factor C can be defined as an average probability that resonance neutrons escaping from a fuel lump will reach another fuel lump without experiencing any collisions with the moderator in between. This definition can be found in many references and is equivalent to the original definition and is a consequence of reciprocity.

4.2.2 Average intra-volume Dancoff factors for a finite volume

Eq. (4.8) can be used to calculate the Dancoff factor for a collection of fuel lumps in an infinite medium (e.g., an infinite medium of TRISO microspheres) if we set the upper limit to infinity in the integral. However, we would like to consider a finite volume, such as a cylindrical fuel compact or spherical fuel pebble that is filled with TRISO microspheres. In this case we want the average Dancoff factor for a TRISO microsphere in the finite volume in order to determine space-dependent few-group cross sections. For the case of a fuel lump in a finite volume, the upper limit would be a finite value related to the position of the fuel lump in the volume and the direction of neutron travel, as depicted by the chords R_1, R_2, R_3 etc. shown in Figure 4.1 below.
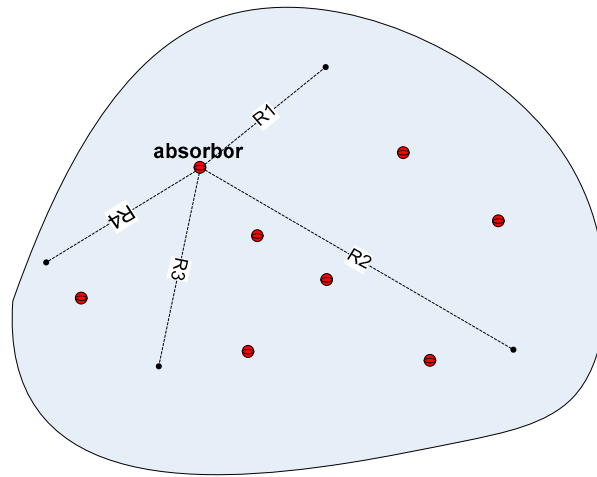
Figure 4.1 Fuel lumps in finite volume

In order to obtain the average Dancoff factor for all the fuel lumps in the volume, the integral in Eq. (4.8) needs to be performed over the surface area of each fuel lump and over the entire volume accounting for every fuel lump. This would be a cumbersome integration. However, if we introduce the chord method to perform the calculation as we did in the previous section, the calculation would be much simpler. Here we take

advantage of the fact that the fuel lumps are randomly distributed in the volume. The physical process that we need to simulate is summarized as follows: A source of resonance-energy neutrons is uniformly distributed on the surface of a fuel lump, and a resonance neutron is emitted outwards with a cosine current angular distribution. The probability that a neutron enters another fuel lump without colliding in the intervening moderator is calculated and averaged over the surface neutron emissions. This average probability is only for a specific fuel lump at a specific location inside the solid body. Since the fuel lump could be anywhere in the volume, we need to average this to account for fuel lumps at different locations in the volume. However, we note that the assumption of a uniform distribution of fuel lumps with uniform cosine current surface sources is equivalent to a uniform, isotropic volumetric source in the moderator. Then the mathematical derivation becomes equivalent to that performed by Case, Hoffmann, and Placzek [51] and Bell and Glasstone [43], when they calculated escape probabilities for finite volumes. This derivation is given below.

A resonance neutron is generated in $d\Omega dV$ with probability $d\Omega dV / 4\pi V$, traveling along direction Ω. If this neutron is regarded as the one just escaping from a fuel lump, its maximum distance along the traveling direction to enter another fuel lump within the volume is l. This distance is determined by the maximum distance to the volume boundary along the chord determined by (r, Ω) and, strictly speaking, should be reduced by the average chord length in the absorber since the absorber cannot overlap the outer boundary. Since the probability of traversing distance l' without a collision in the moderator is given by $e^{-l'/\lambda}$, we find the following expression for the Dancoff factor:

$$C(l) = \int_{min\_d}^{l} f(l')e^{-l'/\lambda}dl', \tag{4.9}$$

where *min_d* is a problem-dependent lower integral limit parameter (such as the minimum distance between two TRISO fuel kernels due to the coatings). This is the Dancoff factor for a specific neutron emitted randomly from the surface of a random fuel lump within the volume. The probability of choosing this specific neutron is $d\Omega dV / (4\pi V)$ hence the average Dancoff factor over all fuel lumps in the volume is given by:

$$\overline{C^{intra}} = \iint \frac{1}{4\pi V} C(l) dV d\Omega. \tag{4.10}$$
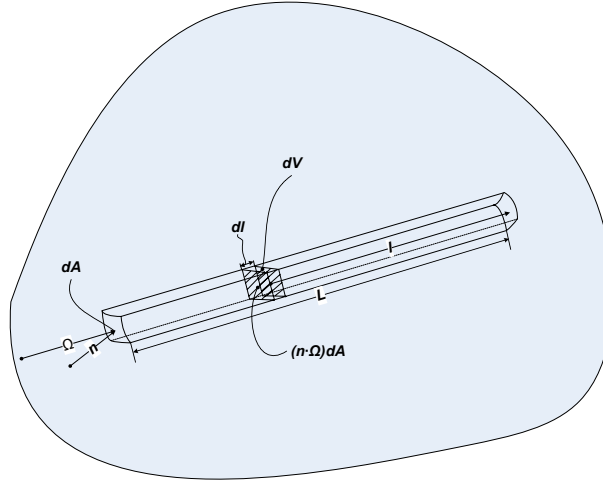
Figure 4.2 Volume element division

From Figure 4.2, $dV = (n \cdot \Omega) dA dl$, so Eq. (4.10) becomes:

$$\overline{C^{intra}} = \frac{1}{4\pi V} \int dA \int d\Omega \cos\theta \int_{min\_d}^{L} C(l) dl, \tag{4.11}$$

where *min_d* has the same meaning as in Eq. (4.9) and L is the maximum distance to the volume boundary as defined earlier. Let $G(L) = \int_{min\_d}^{L} C(l) dl$ and use $\int dA \int d\Omega \cos\theta = \pi A$, where A is the total surface area of the solid. We then get:

$$\overline{C^{intra}} = \frac{\pi A}{4\pi V} \frac{\int dA \int d\Omega \cos\theta G(L)}{\int dA \int d\Omega \cos\theta} = \frac{1}{<L>} \frac{\int dA \int d\Omega \cos\theta G(L)}{\int dA \int d\Omega \cos\theta}, \qquad (4.12)$$

where $<L>=4V/A$, the mean chord length in the solid. As we did in the previous section, if we introduce a chord distribution function $F(L)$ for the finite volume, then a formula with a simple mathematical form is obtained:

$$\overline{C^{intra}} = \frac{1}{<L>} \int F(L)G(L)dL, \qquad (4.13)$$

or a more explicit form:

$$\overline{C^{intra}} = \frac{1}{<L>} \int dL F(L) \int_{min\_d}^{L} dl \int_{min\_d}^{l} dl' f(l')e^{-l'/\lambda}. \qquad (4.14)$$

So the complicated expression for the average Dancoff factor in a finite medium of fuel lumps, which consists of multiple 2D integrals over surface and angle domains, is reduced to a straightforward multiple integral by using two chord length distribution functions: one is the PDF $f(l)$ for the distribution of chord lengths between two fuel lumps and the other is the PDF $F(L)$ for the distribution of chord lengths inside the finite volume.

4.2.3 Average inter-volume Dancoff factors for a collection of finite volumes

VHTRs are characterized by the presence of the double heterogeneity, caused by multiple finite volumes, each of which contains a distribution of fuel lumps. When we calculate the Dancoff factor for a fuel lump, we need to account for not only the intra-volume contribution from the previous section but also the inter-volume contribution since a neutron might exit a finite volume and stream to another finite volume without a

collision. Figure 4.3 shows this general configuration. We will start with this picture to derive the average Dancoff factor accounting for the inter-volume contribution.
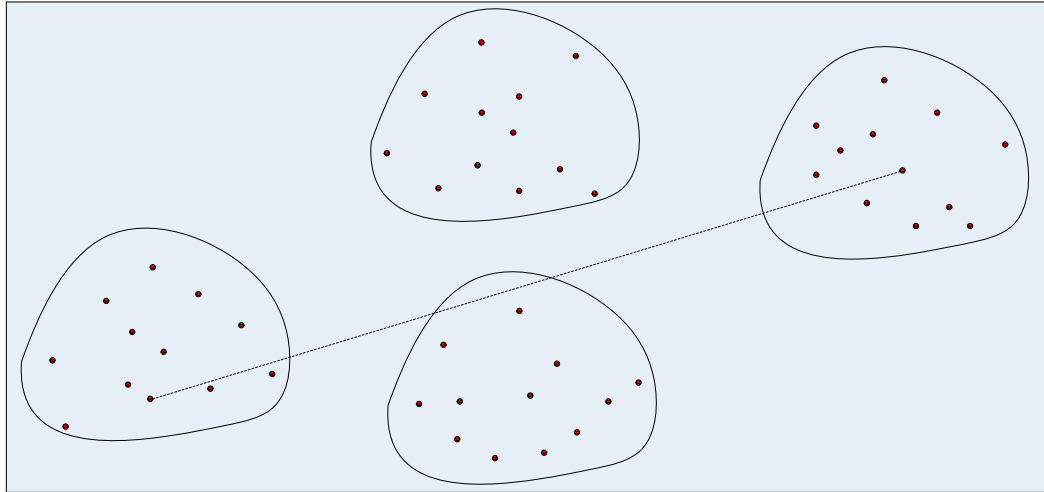
Figure 4.3 Distribution of finite volumes containing fuel lumps

This Dancoff factor can be defined as the probability that a neutron escaping from a fuel lump in a finite volume enters another fuel lump in a different finite volume, known as the inter-volume Dancoff factor. We can write down this probability in terms of several basic probabilities:

P_1---average probability that a neutron escaping from a fuel lump in a finite volume leaks out without entering any other fuel lump or colliding with the moderator

P_2---average probability that a neutron escaping from a finite volume enters another finite volume without collision

P_t---average probability that a neutron incident on a finite volume crosses it without entering any fuel lump or having a collision with the moderator

P_3---average probability that a neutron incident on a finite volume enters a fuel lump within that volume

If we consider that all the finite volumes are uniformly distributed in an infinite

background medium, then the inter-volume Dancoff factor can be written as:

$$\overline{C^{inter}} = P_1 P_2 P_3 + P_1 P_2 P_t P_2 P_3 + P_1 \left(P_2 P_t \right)^2 P_2 P_3 + P_1 \left(P_2 P_t \right)^3 P_2 P_3 + \cdots = P_1 P_2 P_3 \sum_{i=0}^{\infty} \left(P_2 P_t \right)^i \quad , \quad (4.15)$$

or:

$$\overline{C^{inter}} = P_1 P_2 P_3 \frac{1}{1 - P_2 P_t} \quad . \tag{4.16}$$

We will derive these probabilities using the chord method.

To obtain an expression for P_1, we proceed in a similar manner as the derivation

of $\overline{C^{intra}}$. If we write down the probability that any neutron from a small element $d\Omega dV$

escapes a finite volume along Ω without entering another fuel lump or colliding with the

moderator (See Figure 4.2 for geometry description),

$$P_1(l) = \frac{d\Omega dV}{4\pi V} e^{-l/\lambda} \int_l^{\infty} f(l')dl' \quad , \tag{4.17}$$

where l is the distance along the neutron's traveling direction from starting point to the

escaping point of the volume, then

$$P_1 = \iint \frac{d\Omega dV}{4\pi V} e^{-l/\lambda} \int_l^{\infty} f(l')dl' = \frac{\int dA \int d\Omega \cos\theta}{4\pi V} \frac{\int dA \int d\Omega \cos\theta \int_{min\_d}^{L} dl e^{-l/\lambda} \int_l^{\infty} f(l')dl'}{\int dA \int d\Omega \cos\theta} \quad . \tag{4.18}$$

Using the chord length distribution function in a finite body $F(L)$:

$$P_1 = \frac{1}{<L>} \iint \frac{d\Omega dV}{4\pi V} e^{-l/\lambda} \int_l^{\infty} f(l')dl' = \frac{1}{<L>} \int dL F(L) \int_{min\_d}^{L} dl e^{-l/\lambda} \int_l^{\infty} f(l')dl' \quad . \tag{4.19}$$

For P_2, if we assume $H(S)$ is the chord length PDF between two volumes in an

infinite background medium, then

$$P_2 = \int H(S)e^{-S/\lambda}dS \,. \tag{4.20}$$

We will assume $H(S)$ can be determined, perhaps approximately, for the given geometry.

For P_t, we can write down the probability that a neutron incident on a finite volume through a small element $dAd\Omega$ along Ω crosses the finite volume without hitting any fuel lump or colliding with the moderator:

$$P_t(L) = e^{-L/\lambda}\int_L^{\infty} f(l')dl' \,, \tag{4.21}$$

where L is the chord length from the incident point to the exit point along Ω. Then,

$$P_t = \frac{\iint dAd\Omega \cos\theta P_c(L)}{\iint dAd\Omega \cos\theta} = \int dLF(L)e^{-L/\lambda}\int_L^{\infty} f(l')dl' \,. \tag{4.22}$$

For P_3, this may be viewed as a Dancoff factor for a neutron incident on the boundary of the finite volume. Therefore, using our previous results, the average probability that a neutron entering a finite volume will enter a fuel region without colliding in the moderator is:

$$P_3(L) = \int_{min\_d}^{L} f(l)e^{-l/\lambda}dl \,, \tag{4.23}$$

where L is the chord length from the incident point to the exit point along Ω. This is then averaged over all possible chords in the finite volume,

$$P_3 = \frac{\iint dAd\Omega \cos\theta P_3(L)}{\iint dAd\Omega \cos\theta} = \int dLF(L) \int_{min\_d}^{L} f(l)e^{-l/\lambda}dl \,. \tag{4.24}$$

Now all of the terms P_1, P_2, P_3 and P_t have been expressed in terms of chord length distribution functions. Combining Eqs. (4.19), (4.20), (4.22) and (4.24), we obtain a complete analytical formula for $\overline{C^{inter}}$:

$$\overline{C^{inter}} = \frac{\left(\dfrac{1}{<L>}\int dLF(L)\int\limits_{min\_d}^{L} dl e^{-l/\lambda}\int\limits_{l}^{\infty} f(l')dl'\right)\cdot\left(\int H(S)e^{-S/\lambda}dS\right)\cdot\left(\int dLF(L)\int\limits_{min\_d}^{L} f(l)e^{-l/\lambda}dl\right)}{1-\left(\int H(S)e^{-S/\lambda}dS\right)\cdot\left(\int dLF(L)e^{-L/\lambda}\int\limits_{L}^{\infty} f(l')dl'\right)}.$$

(4.25)

4.2.4 Discussion

The methodology presented in previous sections has broad application to general reactor physics analysis but is specifically intended for application to the neutronic analysis of TRISO fuel in VHTRs. This methodology can be applied to the analysis of both pebble-bed and prismatic VHTR designs. The chord length PDF $F(L)$ is known analytically for spheres [52] and cylinders [51,56,57,58,60]. Also, the chord length PDF $H(S)$ between fuel compacts and between fuel pebbles can be determined in an approximate analytical form with an exponential function [53]. As long as we are able to determine the chord length PDF $f(l)$ between two fuel particles in an infinite medium, the average Dancoff factor for fuel particles in either VHTR design is readily obtained by Eqs. (4.14) and (4.25). In the next section, a detailed derivation for $f(l)$ will be given and average Dancoff factors will be calculated for a TRISO fuel particle in infinite medium and finite medium VHTR configurations.

4.3 Dancoff Factor Calculations for Fuel Particles in VHTR

In this section, we will calculate average Dancoff factors for a fuel particle in VHTR configurations, including an infinite medium of TRISO particles and finite cylinders and finite spheres filled with TRISO fuel particles. The finite volume Dancoff factors will include both intra-volume as well as inter-volume contributions.

4.3.1 Simplified physical models and associated mathematical models

Previous neutronic analysis has shown that homogenizing the four coating layer regions with the graphite matrix region does not affect the neutronic behavior [12]. Although the four coating regions and the graphite matrix region were distinct regions for the Dancoff factor calculation, these regions had identical cross sections obtained by homogenizing the materials in these five regions. Based on this, we will use the previously studied single-sphere and dual-sphere models.

Analytical derivations of the chord length PDF $f(l)$ between two fuel particles based on these two models are presented below along with the infinite medium Dancoff factor calculated with this PDF. The corresponding average Dancoff factors for a fuel kernel in a spherical fuel pebble and a cylindrical fuel compact with the two models are also given.

| single-sphere model | dual-sphere model |
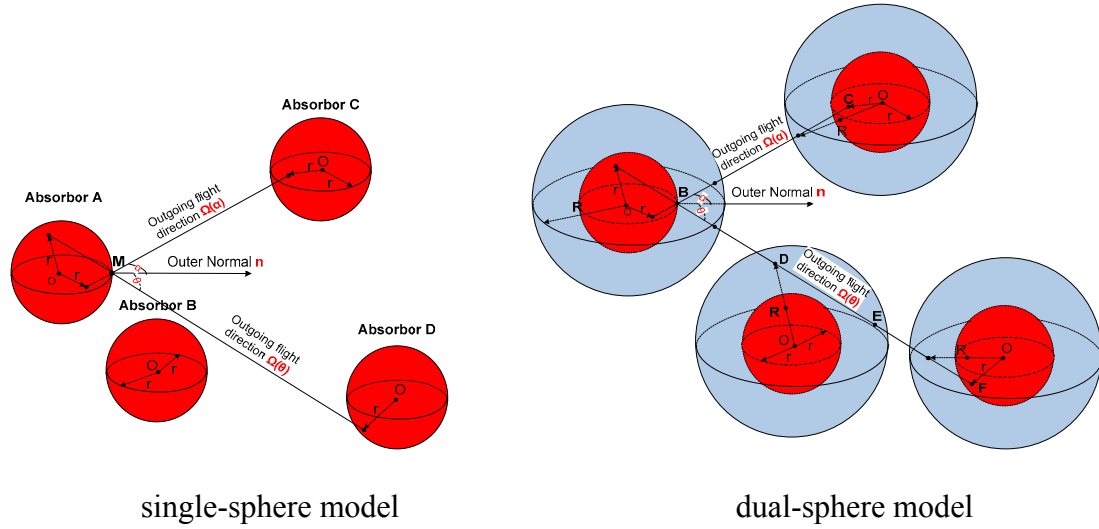
Figure 4.4 VHTR fuel particle models

4.3.2 Analytical derivations

We have already determined the chord length PDF $f_s(l)$ in Chapter 3:

$$f_s(l) = \frac{3}{4r} \cdot \frac{frac(r/R)^3}{1 - frac(r/R)^3} \cdot e^{-l \cdot \frac{3}{4r} \cdot \frac{frac(r/R)^3}{1 - frac(r/R)^3}}. \tag{4.26}$$

This will now be used to compute the Dancoff factor in infinite and finite geometries.

4.3.2.1 Dancoff factor with single-sphere model

- Dancoff Factor for Fuel Kernel in an Infinite Medium of Fuel Kernels

Substituting $f_s(l)$ into Eq. (4.8), the infinite medium Dancoff factor with the single-sphere model is obtained:

$$C^{s,\infty} = \int_0^\infty e^{-x/\lambda} \cdot \frac{1}{<l>} \cdot e^{-l/<l>} \cdot dl = \frac{1}{1 + \frac{1}{\lambda} \cdot <l>} = \frac{1}{1 + \frac{1}{\lambda} \cdot \frac{4r}{3} \cdot \frac{1 - frac \cdot (r/R)^3}{frac \cdot (r/R)^3}}. \tag{4.27}$$

89

- Average Dancoff Factor of Fuel Kernel in Finite Media (Fuel Pebble/Fuel Compact)

Substituting $f_s(l)$ into Eq. (4.14) , the intra-volume Dancoff factor with the single-sphere model is obtained:

$$\overline{C^{intra}} = \frac{1}{<L>} \int dL F(L) \int_0^l dl \int_0^l dl' \frac{1}{<l>} e^{-l'/<l>} e^{-l'/\lambda} ,$$ (4.28)

where we have set $min\_d = 0$ due to model assumptions.

If we define an effective cross section Σ^*:

$$\Sigma^* = \frac{1}{\lambda^*} = \frac{1}{\lambda} + \frac{1}{<l>} ,$$ (4.29)

then after several straightforward integration manipulations, we obtain:

$$\overline{C^{intra}} = \frac{\lambda^*}{<l>} \left[1 - \frac{\lambda^*}{<L>} \int \left(1 - e^{-L/\lambda^*} \right) F(L) dL \right].$$ (4.30)

It is easy to see that $\lambda^*/<l>$ is just $C^{s,\infty}$. It is also found with more careful observation that the second term in the bracket is just the first flight escape probability for a finite medium with a total cross section Σ^* [see page 22 in ref. 51]. The effective cross section Σ^* is identical to the modified total cross section for a two-region lattice in equivalence theory when the "escape" cross section $1/<l>$ is added to the total cross section [43].

So we have a very concise result:

$$\overline{C^{intra}} = C^{s,\infty} \left[1 - P_{esc}^* \right].$$ (4.31)

Thus the average intra-medium Dancoff factor is the product of the infinite medium Dancoff factor and the first flight collision probability for the finite medium.

Bende [48] and Talamo [49] also found a similar expression for $\overline{C^{intra}}$ for fuel pebbles and fuel compacts, respectively. However, their analyses are somewhat more complicated due to a different definition of Σ^* and the complicated integral expression for P^*_{esc}.

The introduction of the chord length PDF $F(L)$ in the expression of $\overline{C^{intra}}$ in Eq. (4.30) makes the formula more flexible, in that it can handle different finite media with arbitrary shape filled with randomly distributed fuel particles. Next, as an application to VHTR analysis, we use Eqs. (4.30) and (4.31) to derive intra-pebble and intra-compact Dancoff factors in terms of basic geometry parameters.

A fuel pebble is composed of two concentric spheres: an inner sphere with a typical radius $R_1 = 2.5$ *cm* and an outer sphere with a typical radius $R_2 = 3.0$ *cm*. Fuel particles are randomly distributed in the inner spherical region, which is called the fuel region. The outer spherical shell is graphite.

The chord length PDF for a sphere of radius R_1 has been obtained: (see Appendix of reference [52])

$$F(L) = \frac{L}{2R_1^2}, \quad 0 < L < 2R_1. \tag{4.32}$$

Substituting this into Eq. (4.30) and after several algebraic manipulations, we find:

$$P^*_{esc} = \frac{3}{4}\left(\frac{\lambda^*}{R_1}\right) + \frac{3}{4}\left(\frac{\lambda^*}{R_1}\right)^2 e^{-2\left(\frac{R_1}{\lambda^*}\right)} - \frac{3}{8}\left(\frac{\lambda^*}{R_1}\right)^3\left[1 - e^{-2\left(\frac{R_1}{\lambda^*}\right)}\right], \tag{4.33}$$

and the final results:

$$\overline{C^{intra}} = C^{s,\infty}\left\{1 - \frac{3}{4}\left(\frac{\lambda^*}{R_1}\right) - \frac{3}{4}\left(\frac{\lambda^*}{R_1}\right)^2 e^{-2\left(\frac{R_1}{\lambda^*}\right)} + \frac{3}{8}\left(\frac{\lambda^*}{R_1}\right)^3\left[1 - e^{-2\left(\frac{R_1}{\lambda^*}\right)}\right]\right\}. \tag{4.34}$$

This may be expressed as follows:

$$\frac{\overline{C^{intra}}}{C^{s,\infty}} = 1 - \frac{3}{4}\left(\frac{\lambda^*}{R_1}\right) - \frac{3}{4}\left(\frac{\lambda^*}{R_1}\right)^2 e^{-2\left(\frac{R_1}{\lambda^*}\right)} + \frac{3}{8}\left(\frac{\lambda^*}{R_1}\right)^3 \left[1 - e^{-2\left(\frac{R_1}{\lambda^*}\right)}\right].$$ (4.35)

As verification, when $R_1 \to \infty$, $\overline{C^{intra}} \to C^{s,\infty}$.

In prismatic VHTR, the fuel compacts are arranged in cylindrical columns of height 793cm. Although these are essentially infinite cylinders, we will derive an expression for $\overline{C^{intra}}$ for both infinite and finite cylinder cases.

For an infinite cylinder region, the chord length distribution PDF was derived by Case et al. (page 32 in reference [51]):

$$F(L) = \frac{16 R_c^2}{\pi L^3}\int_0^{x_0}\frac{x^4 dx}{\sqrt{(L^2/4R_c^2) - x^2}\sqrt{1-x^2}} \quad , \quad x_0 = \begin{cases} 1 & L > 2R_c \\ \dfrac{L}{2R_c} & L < 2R_c \end{cases}.$$ (4.36)

Using the above PDF and results from Inglis [56] for P^*_{esc} in terms of Bessel functions, we find:

$$P^*_{esc} = \frac{2}{3}\left\{2t^2\left[I_0(t)K_0(t) + I_1(t)K_1(t)\right] + t\left[I_0(t)K_1(t) - I_1(t)K_0(t) - 2\right] + I_1(t)K_1(t)\right\},$$ (4.37)

where $t = R_c/\lambda^*$. Substituting this into Eq. (4.31), we obtain the final result:

$$\overline{C^{intra}} = C^{s,\infty}\left\langle 1 - \frac{2}{3}\left\{2t^2\left[I_0(t)K_0(t) + I_1(t)K_1(t)\right] + t\left[I_0(t)K_1(t) - I_1(t)K_0(t) - 2\right] + I_1(t)K_1(t)\right\}\right\rangle.$$ (4.38)

Expressing this as a ratio as before, we find

$$\frac{\overline{C^{intra}}}{C^{s,\infty}} = 1 - \frac{2}{3}\left\{2t^2\left[I_0(t)K_0(t) + I_1(t)K_1(t)\right] + t\left[I_0(t)K_1(t) - I_1(t)K_0(t) - 2\right] + I_1(t)K_1(t)\right\}.$$ (4.39)

As verification, when $R_c \to \infty$, $t \to \infty$, so $P^*_{esc} = \dfrac{1}{2}\dfrac{1}{t} - \dfrac{3}{32}\dfrac{1}{t^3} + ... \to 0$, hence $\overline{C^{intra}} \to C^{s,\infty}$.

For a finite cylinder region, the analytical derivation of *F(L)* has been studied by many researchers [57,58]. Formulas for right circular cylinders and general cylinders have been given in complicated forms. However, by using some simple mathematical transformations, some researchers [59,60] have derived an expression for the escape probability P^*_{esc} for a finite cylinder, which can be used directly to obtain $\overline{C^{intra}}$. According to Marleau et al. [60], we have the following results for the escape probabilities:

$$P^*_{esc,t\&b} = \frac{\lambda^*}{H}\left[E_3(0) - E_3\left(\frac{H}{\lambda^*}\right)\right] - \frac{4}{\pi D^2}\frac{\lambda^*}{H}\int_0^D \left\{E_3\left(\frac{t}{\lambda^*}\right) - E_3\left[\frac{\left(t^2 + H^2\right)^{1/2}}{\lambda^*}\right]\right\}\left(D^2 - t^2\right)^{1/2} dt,$$

(4.40)

$$P^*_{esc,cyl} = \frac{4}{\pi D^2 H}\int_0^D t^2 dt \int_0^H (H-u)\frac{\exp\left(-\dfrac{\left(t^2 + u^2\right)^{1/2}}{\lambda^*}\right)\left(D^2 - t^2\right)^{1/2}}{\left(t^2 + u^2\right)^{3/2}} du,$$

(4.41)

$$P^*_{esc,cyl} = \frac{4}{\pi D^2 H}\int_0^D t^2 dt \int_0^H (H-u)\frac{\exp\left(-\dfrac{\left(t^2 + u^2\right)^{1/2}}{\lambda^*}\right)\left(D^2 - t^2\right)^{1/2} - D}{\left(t^2 + u^2\right)^{3/2}} du$$

$$+ \frac{4}{\pi D^2 H}\frac{D}{2}\left\{H^2 \ln\left[\frac{D + \left(D^2 + H^2\right)^{1/2}}{H}\right] + D\left(D^2 + H^2\right)^{1/2} - D^2\right\},$$

(4.42)

where $P^*_{esc,t\&b}$ is the axial escape probability across the top and bottom surfaces, $P^*_{esc,cyl}$ is the radial escape probability across the cylindrical surface, and $D = 2R_c$. Adding these two escape probabilities yields the total escape probability for a finite cylinder:

$$P_{esc}^* = P_{esc,t\&b}^* + P_{esc,cyl}^*. \tag{4.43}$$

So the final result is:

$$\overline{C^{intra}} = C^{s,\infty}\left(1-P_{esc}^*\right), \tag{4.44}$$

or:

$$\frac{\overline{C^{intra}}}{C^{s,\infty}} = 1-P_{esc}^*. \tag{4.45}$$

- Average Inter-Pebble and Inter-Compact Dancoff Factors for Fuel Kernels

As we did for $\overline{C^{intra}}$, we introduce the single-sphere model chord length PDF Eq.(4.26) between two fuel kernels into Eqs. (4.19), (4.22), (4.24) and (4.25) to obtain a general expression for $\overline{C^{inter}}$. Then we use this formula to obtain inter-pebble and inter-compact Dancoff factors.

Substituting Eq. (4.26) into Eqs. (4.19), (4.22), and (4.24), and using the effective cross section Σ^* defined by Eq. (4.29), we find:

$$P_{1,s} = \frac{1}{<L>}\int dLF(L)\int_0^L dl e^{-l/\lambda}\int_l^\infty \frac{1}{<l>}\cdot e^{-l'/<l>}dl' = \frac{\lambda^*}{<L>}\int\left(1-e^{-L/\lambda^*}\right)F(L)dL = P_{esc}^*, \tag{4.46}$$

$$P_{t,s} = \int dLF(L)e^{-L/\lambda}\int_L^\infty \frac{1}{<l>}e^{-l'/<l>}dl' = \int dLF(L)e^{-\frac{L}{\lambda^*}} = 1-\frac{<L>}{\lambda^*}P_{esc}^*, \tag{4.47}$$

$$P_{3,s} = \int dLF(L)\int_0^L \frac{1}{<l>}\cdot e^{-l/<l>}e^{-l/\lambda}dl = C^{s,\infty}\int\left(1-e^{-L/\lambda^*}\right)F(L)dL = C^{s,\infty}\frac{<L>}{\lambda^*}P_{esc}^*. \tag{4.48}$$

Finally, substituting these results into Eq. (4.25), we find:

$$\overline{C^{inter}} = \frac{P_{esc}^* \cdot \left(\int H(S) e^{-S/\lambda} dS \right) \cdot \left(C^{s,\infty} \frac{<L>}{\lambda^*} P_{esc}^* \right)}{1 - \left(\int H(S) e^{-S/\lambda} dS \right) \cdot \left(1 - \frac{<L>}{\lambda^*} P_{esc}^* \right)}, \tag{4.49}$$

which can be expressed as a ratio:

$$\frac{\overline{C^{inter}}}{C^{s,\infty}} = \frac{P_{esc}^* \cdot \left(\int H(S) e^{-S/\lambda} dS \right) \cdot \left(\frac{<L>}{\lambda^*} P_{esc}^* \right)}{1 - \left(\int H(S) e^{-S/\lambda} dS \right) \cdot \left(1 - \frac{<L>}{\lambda^*} P_{esc}^* \right)}. \tag{4.50}$$

Again, it can be seen that the average inter-volume Dancoff factor for a fuel kernel is a relatively simple expression involving the first flight escape probability P_{esc}^*, the effective cross section Σ^*, and the chord length PDF $H(S)$ between the finite volumes.

Next, we apply this formula to compute the inter-pebble and inter-compact Dancoff factors:

Eq. (4.33) gives the first flight escape probability for a spherical fuel pebble. Using this, we can explicitly find expressions for $P_{1,s}$, $P_{t,s}$ and $P_{3,s}$.

$$P_{1,s} = \frac{3}{4} \left(\frac{\lambda^*}{R_1} \right) + \frac{3}{4} \left(\frac{\lambda^*}{R_1} \right)^2 e^{-2\left(\frac{R_1}{\lambda^*} \right)} - \frac{3}{8} \left(\frac{\lambda^*}{R_1} \right)^3 \left[1 - e^{-2\left(\frac{R_1}{\lambda^*} \right)} \right], \tag{4.51}$$

$$P_{t,s} = -\left(\frac{\lambda^*}{R_1} \right) e^{-2\left(\frac{R_1}{\lambda^*} \right)} + \frac{1}{2} \left(\frac{\lambda^*}{R_1} \right)^2 \left[1 - e^{-2\left(\frac{R_1}{\lambda^*} \right)} \right], \tag{4.52}$$

$$P_{3,s} = C^{s,\infty} \left[1 + \left(\frac{\lambda^*}{R_1} \right) e^{-2\left(\frac{R_1}{\lambda^*} \right)} - \frac{1}{2} \left(\frac{\lambda^*}{R_1} \right)^2 \left(1 - e^{-2\left(\frac{R_1}{\lambda^*} \right)} \right) \right]. \tag{4.53}$$

For $P_{2,s}$, we need the chord length PDF between two spherical fuel pebbles. This PDF $H(S)$ could be for an infinite medium or a finite medium of fuel pebbles. For

simplicity, we will derive $H(S)$ for an infinite medium since the benchmark results are for

the infinite medium case. This will be relaxed later.

Assuming the spherical fuel pebbles are randomly distributed in the background

moderator, we have:

$$H(S) = \frac{1}{<S>} e^{-S/<S>}, \quad 0 < S < \infty, \tag{4.54}$$

where $<S> = \frac{4R_1(1-FRAC)}{3FRAC}$ and $FRAC$ is the volume packing fraction of the spherical

fuel region in the whole medium. Substituting Eq. (4.54) into the expression for $P_{2,s}$, we

find:

$$P_{2,s} = \int_0^{\infty} \frac{1}{<S>} e^{-S'/<S>} e^{-S'/\lambda} dS' = \frac{1}{1 + <S> \dfrac{1}{\lambda}}. \tag{4.55}$$

It should be noted that the model presented in Eqs. (4.54) and (4.55) to calculate

$P_{2,s}$ is a crude approximation. It is only valid for high packing fractions. In order to

predict accurate inter-pebble Dancoff factors, we need to perform a Monte Carlo

simulation to get $P_{2,s}$. We have found this simulation to be very cheap to obtain a "one

sigma" (one relative standard deviation) result accurate to within 10^{-4}. In the results

comparison section later in this chapter, we will show the comparison between this crude

model and the more precise Monte Carlo simulation for calculating $P_{2,s}$.

At this point we have obtained expressions for $P_{1,s}$, $P_{t,s}$, $P_{3,s}$, and $P_{2,s}$. Introducing

them into Eq. (4.49) or (4.50), we obtain $\overline{C^{inter}}/C^{s,\infty}$ in terms of basic geometry quantities

for fuel pebbles:

$$\overline{C^{inter}} = C^{s,\infty} \frac{\frac{3}{4}\frac{\lambda^*}{R_1}\left(1+\left(\frac{\lambda^*}{R_1}\right)e^{-2\left(\frac{R_1}{\lambda^*}\right)}-\frac{1}{2}\left(\frac{\lambda^*}{R_1}\right)^2\left[1-e^{-2\left(\frac{R_1}{\lambda^*}\right)}\right]\right)^2 \cdot \frac{1}{1+<S>\frac{1}{\lambda}}}{1-\frac{1}{1+<S>\frac{1}{\lambda}}\cdot\left(-\left(\frac{\lambda^*}{R_1}\right)e^{-2\left(\frac{R_1}{\lambda^*}\right)}+\frac{1}{2}\left(\frac{\lambda^*}{R_1}\right)^2\left[1-e^{-2\left(\frac{R_1}{\lambda^*}\right)}\right]\right)}. \qquad (4.56)$$

Again, expressing this as a ratio:

$$\frac{\overline{C^{inter}}}{C^{s,\infty}} = \frac{\frac{3}{4}\frac{\lambda^*}{R_1}\left(1+\left(\frac{\lambda^*}{R_1}\right)e^{-2\left(\frac{R_1}{\lambda^*}\right)}-\frac{1}{2}\left(\frac{\lambda^*}{R_1}\right)^2\left[1-e^{-2\left(\frac{R_1}{\lambda^*}\right)}\right]\right)^2 \cdot \frac{1}{1+<S>\frac{1}{\lambda}}}{1-\frac{1}{1+<S>\frac{1}{\lambda}}\cdot\left(-\left(\frac{\lambda^*}{R_1}\right)e^{-2\left(\frac{R_1}{\lambda^*}\right)}+\frac{1}{2}\left(\frac{\lambda^*}{R_1}\right)^2\left[1-e^{-2\left(\frac{R_1}{\lambda^*}\right)}\right]\right)}. \qquad (4.57)$$

To obtain inter-compact Dancoff factors for the prismatic VHTR, we will model the fuel compacts as both infinite cylinders and finite cylinders.

For both cases, Eqs. (4.37) and (4.43) give the first flight escape probabilities separately. Substituting these formulas into Eqs. (4.46)-(4.48), we can easily write down $P_{1,s}$, $P_{t,s}$ and $P_{3,s}$ for both infinite and finite cylinders. For conciseness, we will not repeat these long formulas here. Only one point needs to be noted, the average chord length $<L>$ appearing in $P_{1,s}$, $P_{t,s}$ and $P_{3,s}$ is different for infinite and finite cylinders: for an infinite cylinder, $<L> = 2R_c$ while for a finite cylinder, $<L> = \frac{2R_c H}{R_c + H}$.

For $P_{2,s}$, we need to obtain the chord length PDF between two cylindrical fuel compacts. At this point, if we look at the definition of $P_{2,s}$ in Eq.(4.20), we can see this is actually the Dancoff factor definition for finite volumes distributed in a moderator background. So the evaluation of $P_{2,s}$ becomes a classical problem: the calculation of the

Dancoff factor for cylindrical fuel rods in a hexagonal lattice, which was the original application studied by Dancoff and Ginsburg [42] in their classical report of 1944.

In such a lattice structure, an accurate expression for the PDF $H(S)$ is difficult to derive analytically especially for finite cylinders. Efforts to find reasonable approximations to $H(S)$ for the infinite cylinder case have been made by Sauer [53] and Chao et al.[61]. Sauer characterized $H(S)$ for the moderator by using a geometric index parameter determined by the method of logarithmic moments. Chao et al.suggested a moment expansion approximation scheme to transform the integral $\int H(S)\, e^{-S/\lambda} dS$ into a summation of a finite series and keeping low order terms. Both approaches gave good results for lattice structures. Meanwhile, based on formulas derived by Dancoff and Ginsburg, Thie [62], Fukai [63] and Carlvik [64] contributed by improving the accuracy of the analytical formula and by using numerical integration techniques. Also, Fehér et al.[65] incorporated the analytical integration into a Monte Carlo simulation to calculate the Dancoff factor for a lattice structure.

From our viewpoint, lattice structure, whether square or hexagonal, is a relatively simple geometry for calculating Dancoff factors. Taking advantage of modern day computing capability, this work can be done in a few seconds using Monte Carlo methods, yielding excellent results with a relative standard deviation less than 10^{-4}. Accordingly, we use Monte Carlo simulation to obtain $P_{2,s}$ for infinite and finite cylindrical fuel compacts.

During the writing of this thesis, a recently published paper by Talamo [49] draws our attention. Talamo utilized an equivalent unit cell of concentric cylinders to study the inter-compact Dancoff factor. A white outer boundary condition was applied, implying

that the fuel compact is randomly distributed inside the lattice, although this is not the case in reality. However, this is an interesting alternative model to the Monte Carlo calculation. That is, we can calculate $P_{2,s}$ using the chord length $H(S)$ between two fuel compacts, hence assuming a stochastic distribution of fuel compacts. We have already done this for the inter-pebble Dancoff factor analysis, although this is a more realistic assumption in this case.

As we did for fuel pebbles, if we regard the fuel compacts as being randomly distributed in background moderator (all the axes are kept vertical and parallel), we can make an assumption that the chord lengths between fuel compacts follow an exponential function,

$$H(S) = \frac{1}{<S>} e^{-S/<S>}, \quad 0 < S < \infty, \tag{4.58}$$

where $<S> = \dfrac{2R_c(1-FRAC)}{FRAC}$ and $FRAC$ is the volume packing fraction of the cylindrical fuel compact region in the whole medium. Introducing Eq. (4.58) into the $P_{2,s}$ expression, we then obtain,

$$P_{2,s} = \int_0^\infty \frac{1}{<S>} e^{-S'/<S>} e^{-S'/\lambda} dS' = \frac{1}{1+<S>\dfrac{1}{\lambda}} \tag{4.59}$$

It is noted that Eq. (4.59) only applies to the infinite cylinder case. For a finite cylinder, $H(S)$ would be related to the height of the cylinder and would not be such a simple exponential relation. In order to calculate $P_{2,s}$, for a finite cylinder, we will need to resort to the Monte Carlo method.

Now we have obtained analytical expressions for $P_{1,s}$, $P_{t,s}$ and $P_{3,s}$. By simple Monte Carlo simulations, we can obtain numerical values for $P_{2,s}$, or we can use Eq.

(4.59) to obtain an approximate value for $P_{2,s}$. Introducing this into Eq. (4.49) or (4.50), we obtain either an analytic formula or a numerical estimate for C^{inter} in terms of basic geometry quantities of fuel compacts.

4.3.2.2 Dancoff factor with dual-sphere model

- Dancoff Factor of Fuel Kernel in an Infinite Medium

For the dual-sphere model, the derivation starts with the single-sphere model result and takes into account the coating region. The chord length PDF with dual-sphere model can be derived from Eq. (4.26) by a small correction:

$$f_d(l) = \frac{f_s(l)}{\int_{2d}^{\infty} f_s(l) \cdot dl} = \frac{1}{<l>} \cdot e^{-(l-2d)/<l>}, \qquad 2d < l < \infty. \qquad (4.60)$$

Substituting $f_d(l)$ into Eq. (4.8), the infinite medium Dancoff factor with the dual-sphere model is obtained:

$$C^{d,\infty} = \int_{2d}^{\infty} e^{-l/\lambda} \cdot \frac{1}{<l>} \cdot e^{-(l-2d)/<l>} \cdot dl = \frac{1}{1 + \frac{1}{\lambda} \cdot <l>} \cdot e^{-2d/\lambda} = \frac{1}{1 + \frac{1}{\lambda} \cdot \frac{4r}{3} \cdot \frac{1 - frac \cdot (r/R)^3}{frac \cdot (r/R)^3}} \cdot e^{-2d/\lambda}.$$

$$(4.61)$$

The rest of this section will be the same as the previous section. For conciseness, we ignore the detailed derivations and directly list the final important results, which can be compared with the single-sphere model results.

- Average Dancoff Factor of Fuel Kernel in a Finite Medium (Fuel Pebble/Fuel Compact)

Substituting $f_d(l)$ into Eq. (4.14) and setting $min\_d = 2d$, the intra-volume Dancoff factor with the dual-sphere model is obtained:

$$\overline{C^{\text{int}ra}} = C^{d,\infty} \left[1 - \frac{\lambda^*}{<L>} + \frac{\lambda^*}{<L>} e^{2d/\lambda^*} - P^*_{esc} e^{2d/\lambda^*} - \frac{2d}{<L>} \right]. \tag{4.62}$$

The average intra-pebble Dancoff factor is then found and expressed as a ratio:

$$\frac{\overline{C^{\text{int}ra}}}{C^{d,\infty}} = 1 - \frac{3}{4}\left(\frac{2d}{R_1}\right) - \frac{3}{4}\left(\frac{\lambda^*}{R_1}\right) - \frac{3}{4}\left(\frac{\lambda^*}{R_1}\right)^2 e^{-2\left(\frac{R_1}{\lambda^*}\right)} e^{-2\left(\frac{d}{\lambda^*}\right)} + \frac{3}{8}\left(\frac{\lambda^*}{R_1}\right)^3 \left[1 - e^{-2\left(\frac{R_1}{\lambda^*}\right)} \right] e^{-2\left(\frac{d}{\lambda^*}\right)}. \tag{4.63}$$

The average intra-volume Dancoff factor for an infinite cylinder can be obtained

by substituting Eq. (4.37) into Eq. (4.62) and replacing $<L>$ by $2R_c$; while for a finite

cylinder by substituting Eqs. (4.40)-(4.43) into Eq. (4.62) and replacing $<L>$ by $\frac{2R_cH}{R_c+H}$.

- Average Dancoff Factor of Fuel Kernel between Finite Media (Fuel Pebbles/Fuel

  Compacts)

  Following the same procedure as for the single-sphere model by setting $min\_d =$

$2d$, the average inter-volume Dancoff factor with the dual-sphere model is found and

expressed as a ratio:

$$\frac{\overline{C^{\text{int}er}}}{C^{d,\infty}} = \frac{\frac{\lambda^*}{<L>}\left[1 - e^{\frac{2d}{\lambda^*}} + \frac{<L>}{\lambda^*} P^*_{esc} e^{\frac{2d}{\lambda^*}} \right] e^{-\frac{2d}{\lambda}} \cdot \left(\int H(S) e^{-S/\lambda} dS \right) \cdot \left(e^{\frac{2d}{\lambda^*}} \frac{<L>}{\lambda^*} P^*_{esc} \right)}{1 - \left(\int H(S) e^{-S/\lambda} dS \right) \cdot e^{2d/\lambda^*} \left(1 - \frac{<L>}{\lambda^*} P^*_{esc} \right) e^{-2d/\lambda}}. \tag{4.64}$$

By substituting appropriate expressions for $<L>$, P^*_{esc} and $H(S)$ for fuel pebble

and fuel compact geometries, the average inter-pebble and inter-compact Dancoff factors

can be obtained.

4.3.3 Early calculations of Dancoff factors for infinite stochastic media

The earliest papers that discussed the evaluation of the Dancoff factor for an infinite medium with grain structure are those by Lane et al. and Nordheim in 1962 [66,67]. These papers gave a result similar to Eq. (4.27), but with a different mean chord length $<l> = 4r/3 \cdot (1/frac')$. Since they used a classical atomic structure model to obtain the mean chord length, which assumes the fuel kernels are infinitesimal, the mean chord length was overestimated. Their derivations miss the factor $(1-frac')$, which accounts for the finite size of the grains hence leading to an incorrect homogeneous limit [67,68]. Although Nordheim had pointed out this homogeneous limit inconsistency, he did not give a solution to solve it. Lewis also noted this [68] and used an alternative result due to Bell [69] to obtain the correct homogeneous limit. It is clear that this inconsistency was due to the incorrect evaluation of the mean chord length in the moderator. This has been corrected in our expression for the infinite medium Dancoff factor in Eq. (4.27), which yields the correct homogeneous limit for the escape probability.

Also, Lane et al. [66] suggested a method to account for the coating region by changing the lower integral limit from 0 to $2d$ in Eq. (4.27). However, this treatment gave poor results since the chord length PDF should also be changed if a coating region was added to the fuel kernel, but this was not done by Lane. We need to simultaneously change the PDF to account for the coating region as well as the lower limit. This is what the dual-sphere model accomplishes.

4.3.4 Monte Carlo simulations

In order to verify the analytical formulas derived for Dancoff factor computations, Monte Carlo benchmark simulations were performed to compare with numerical and analytical results. These benchmark calculations cover the following aspects:

- Dancoff factors for fuel kernels in an infinite medium as a function of volume packing fractions

- Determination of the chord length PDF between two fuel kernels in an infinite stochastic medium generated by the RSA sphere packing method for different volume packing fractions.

- Average intra-pebble and inter-pebble Dancoff factors for fuel kernels in pebble-bed VHTRs

- Average intra-compact and inter-compact Dancoff factors for fuel kernels in prismatic VHTRs

Monte Carlo simulations employed conventional ray tracing to directly track neutron trajectories and used a modified fast RSA algorithm [31] to generate multiple realizations of the stochastic media.

4.3.4.1 Benchmark calculations for Dancoff factor of fuel kernel in an infinite medium

A Monte Carlo code was written to simulate the transport of resonance energy neutrons in a stochastic medium. Depending on the packing fraction, approximately 5-10 million TRISO fuel particles are dispersed randomly in a graphite background region using the RSA algorithm. Neutrons are emitted uniformly from the surface of fuel kernels with a cosine current distribution. The number of neutrons that successfully reach another

fuel kernel without having a collision in the graphite region was tallied, and the Dancoff factor was then computed as the ratio of this number to the total number of neutrons emitted. A total of 100 physical realizations were performed, and 10M neutrons were followed per realization. The final Dancoff factor was ensemble-averaged over the 100 realizations.

4.3.4.2 Chord length PDF simulations in an infinite medium

In order to verify the applicability of Eq. (4.8), the chord length PDF between two fuel kernels, a Monte Carlo simulation was performed at different volume packing fractions. The same geometry and source distribution were used as in the previous section except that the number of fuel particles was 10-20 million, and 500,000 neutrons were emitted per realization. Figure 4.5 shows the results with different volume packing fractions from 5.76% (pebble bed reactor) to 28.92% (prismatic type reactor).
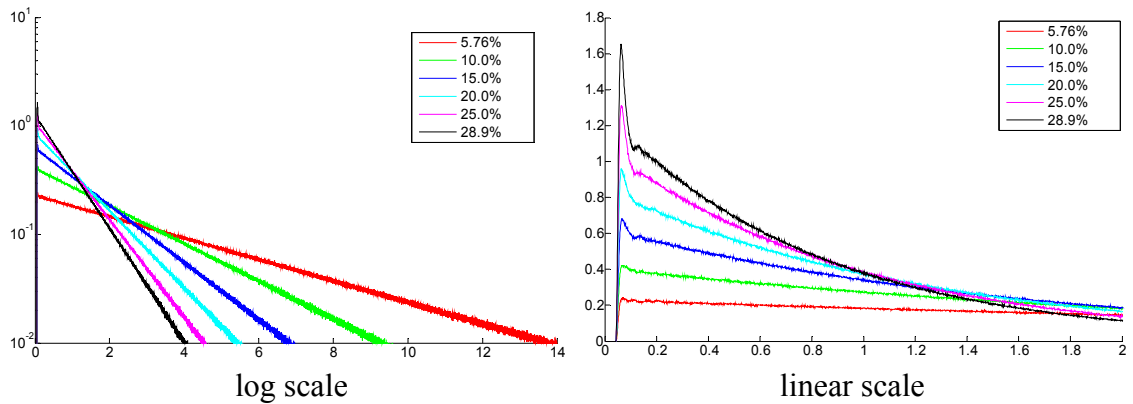
Figure 4.5 Chord length PDFs between two absorbers

All the PDFs start from chord length $2d = 2(R\text{-}r) = 0.043$ *cm*, which is as expected. They quickly increase to a peak value and then decay exponentially for long

chord lengths. The log scale plot verifies that the chord length PDF is well approximated

by an exponential distribution and may be used for the calculation of the Dancoff factor.

4.3.4.3 Benchmark calculations for intra- and inter-pebble Dancoff factors for pebble-bed VHTRs

Two concentric spheres (Figure 4.6) were set up to model the fuel pebble in the

pebble-bed reactor. The inner sphere represents the fuel region filled with stochastically

distributed fuel particles. Its radius is fixed at R_1=2.5cm. The outer spherical shell

represents the moderator region with outer radius R_2 that is approximately 3.0cm but may

change depending on the ratio of the fuel region and moderator region in a pebble-bed

reactor. This geometry is used to calculate both the intra-pebble and inter-pebble Dancoff

factors.

For the intra-pebble Dancoff factor, from 5K to 70K fuel particles were packed

inside the fuel region using the RSA algorithm, the actual number dependent on the

packing fractions which range from 2.00% to 25.00%. Neutrons are emitted uniformly

from the surface of 1000 sampled fuel kernels with a cosine current distribution. The

number of neutrons that successfully reach another fuel kernel without having a collision

was tallied, and the Dancoff factor is the ratio of this number to the total number of

neutrons emitted. Neutrons leaking out of the fuel region without a collision were

rejected. A total of 100 physical realizations were performed, and 10M neutrons were

emitted per realization. The final Dancoff factor was ensemble-averaged over the 100

realizations.

For the inter-pebble Dancoff factor, the same configuration was set up as for the

intra-pebble calculation, except that a white boundary condition was set on the outer

spherical surface. The packing fraction was fixed at 5.76%, but R_2 was adjusted from 3.0cm to 6.0cm. Neutrons were emitted from the surface of fuel particles and traveled through the fuel region and moderator shell region. Only those neutrons that reentered the fuel region at least once and encountered another fuel particle without colliding with a moderator were tallied. The ratio of this number to the total number of neutrons emitted is the inter-pebble Dancoff factor.

4.3.4.4 Benchmark calculations for intra-compact and inter-compact Dancoff factors for prismatic VHTRs

A hexagonal lattice structure was set up to model a fuel compact cell in the prismatic VHTR (Figure 4.6). The cylindrical fuel compact region has radius $R_c = 0.6225$ cm and the outer hexagonal graphite region has a flat-to-flat distance $2P = 2.196$ cm. Both infinite cylinders and finite cylinders were modeled.

For the infinite cylinder, the height was $H = 200$ cm with reflecting boundaries on the top and bottom. Fuel particles were randomly packed inside the cylinder with packing fractions from 2.00% to 28.92%. The packing fraction 28.92% was chosen for the inter-compact Dancoff factors. Only P was adjusted, from 1.098cm to 2.0cm. Then 10M neutrons were emitted per realization and 100 realizations were simulated, similar to the pebble-bed analysis.

For the finite cylinder, the packing fraction was fixed at 28.9% and H was adjusted from 2cm to 100cm for both intra-compact and inter-compact Dancoff factor computations. The other settings were the same as for the infinite cylinder case.
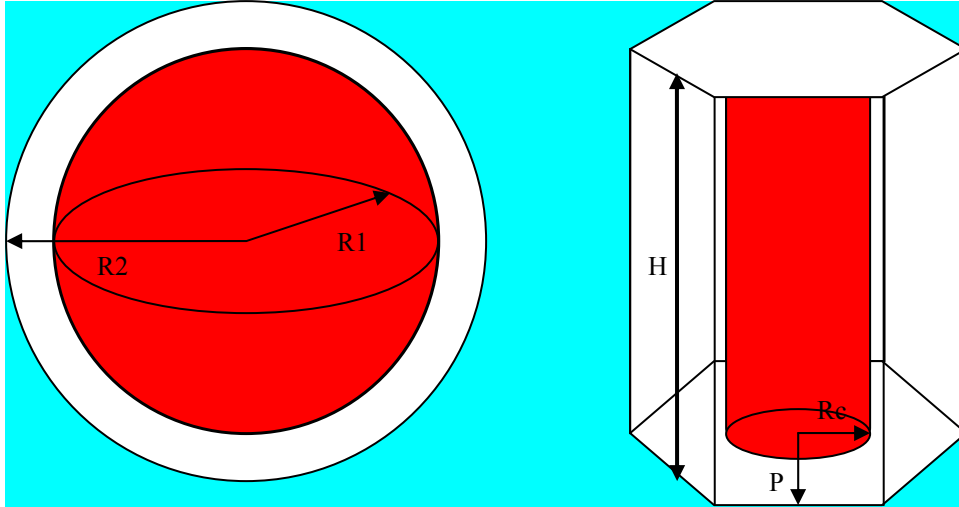
Figure 4.6 Monte Carlo simulation models for fuel pebble and fuel compact cells

4.3.5 Analytical Dancoff factors and comparison with benchmark results

Geometry and composition quantities used in the analytical calculations and Monte Carlo simulations are listed in Table 4.1. The geometry quantities are from a NGNP report [2], and cross section data are from the BNL website [32] evaluated at resonance energy 6.67ev.

Table 4.1 Quantities of parameters

Parameters	Quantities	Unit
r	0.0175	cm
R	0.0390	cm
$2d = 2(R\text{-}r)$	0.043	cm
$1/\lambda$	0.4137	cm^{-1}

4.3.5.1 Analytical infinite medium Dancoff factors

- Using single-sphere model

Table 4.2 includes Dancoff factors predicted with Eq. (4.27), which is the single-sphere model. The results are surprisingly good being within 1.1% for all volume packing

107

fractions, with somewhat better results for higher packing fractions. Interestingly, all the

predicted Dancoff factors are higher than the benchmarks.

Table 4.2 Analytical results with single-sphere model compared to benchmark results

Volume Packing Fractions	Analytical Formula Results $C^{s,\infty}$ Eq. (4.27)	Monte Carlo Benchmark Results C^B (1σ)	Differences $C^{s,\infty}- C^B$	Relative Error $(C^{s,\infty}- C^B)/ C^B$
0.0576	0.3515	0.3477 (.0002)	0.0038	1.09%
0.10	0.4857	0.4820 (.0002)	0.0037	0.77%
0.15	0.5873	0.5841 (.0002)	0.0032	0.55%
0.20	0.6559	0.6534 (.0001)	0.0025	0.38%
0.25	0.7054	0.7029 (.0001)	0.0025	0.35%
0.2892	0.7353	0.7331 (.0001)	0.0021	0.30%

- Using dual-sphere model

Table 4.3 includes results for the same cases as in Table 4.2, but using the dual-sphere model, Eq. (4.61) for the Dancoff factor. Contrary to the results in Table 4.2, the Dancoff factors are all under-estimated (within 1.5%) with the dual-sphere model and the results are better for low volume packing fractions.

Table 4.3 Analytical results with dual-sphere model compared to benchmark results

Volume Packing Fractions	Analytical Formula Results $C^{d,\infty}$ Eq. (4.61)	Monte Carlo Benchmark Results C^B (1σ)	Differences $C^{d,\infty}- C^B$	Relative Error $(C^{d,\infty}- C^B)/ C^B$
0.0576	0.3453	0.3477 (.0002)	-0.0024	-0.69%
0.10	0.4772	0.4820 (.0002)	-0.0048	-1.00%
0.15	0.5770	0.5841 (.0002)	-0.0071	-1.22%
0.20	0.6444	0.6534 (.0001)	-0.0090	-1.38%
0.25	0.6929	0.7029 (.0001)	-0.0100	-1.42%
0.2892	0.7223	0.7331 (.0001)	-0.0108	-1.47%

4.3.5.2 Calculation of Dancoff factors with empirical chord length PDFs

The introduction of the chord length PDF makes the Dancoff factor calculation succinct and mathematically simple. However, it is still worth studying the accuracy of this approach, i.e. how accurate is Eq. (4.8) if a known PDF is used. To address this, a separate calculation was performed to verify the consistency of the Dancoff factor calculation and the simulated chord length PDFs. Eq. (4.8) is an exact expression for the Dancoff factor in term of the fuel particle chord length PDF. Therefore, if the empirical PDF was used in Eq. (4.8), the resultant Dancoff factor should be equal to the benchmark Dancoff factors obtained by Monte Carlo simulation.

Table 4.4 compares these two estimates of the Dancoff factors and the agreement is within 0.3%, with no observable trend with packing factor. We conclude that our methodology for estimating Dancoff factors and estimating chord length PDF's, is reasonable and self-consistent.

Table 4.4 Analytical results from Eq. (4.8) using simulated PDF compared to benchmark results

Volume Packing Fractions	Analytical Formula Results $C^{A,\infty}$ Eq. (4.8)	Monte Carlo Benchmark Results $C^{B,\infty}$ (1σ)	Differences $C^{A,\infty} - C^{B,\infty}$	Relative Error $\dfrac{C^{A,\infty} - C^{B,\infty}}{C^{B,\infty}}$
0.0576	0.3471	0.3477 (.0002)	-0.0006	-0.17%
0.10	0.4810	0.4820 (.0002)	-0.0010	-0.21%
0.15	0.5827	0.5841 (.0002)	-0.0014	-0.24%
0.20	0.6516	0.6534 (.0001)	-0.0018	-0.27%
0.25	0.7014	0.7029 (.0001)	-0.0015	-0.21%
0.2892	0.7316	0.7331 (.0001)	-0.0015	-0.20%

4.3.5.3 Analytical intra-pebble and inter-pebble Dancoff factors

In this section, analytical intra-pebble and inter-pebble Dancoff factors are compared with Monte Carlo benchmark simulations.

- Intra-pebble Dancoff factors

Results are compared at different volume packing fractions ranging from 2.00% to 25.0%. Numerical data for both single-sphere and dual-sphere models are plotted in Figure 4.7, along with the Monte Carlo benchmark results.
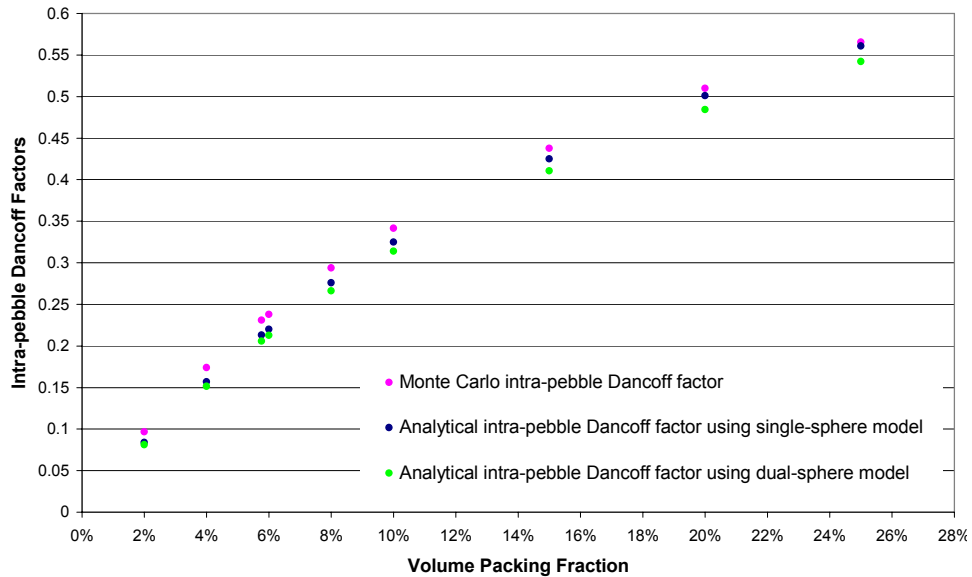
Figure 4.7 Comparison between analytical and Monte Carlo intra-pebble Dancoff factors

Figure 4.7 shows that the single-sphere model gives better results than the dual-sphere model over the range of volume packing fractions. At lower packing fractions, however, both models give poor results. With increasing packing fraction, the single-sphere model gives better results especially beyond 20.0%.

- Inter-pebble Dancoff factors

For inter-pebble Dancoff factors comparisons, we fixed the volume packing fraction at 5.76%. The outer radius R_2 of the fuel pebble was varied by changing the ratio R_2/R_1 from 1.2 to 2.4. The results are plotted in Figure 4.8.
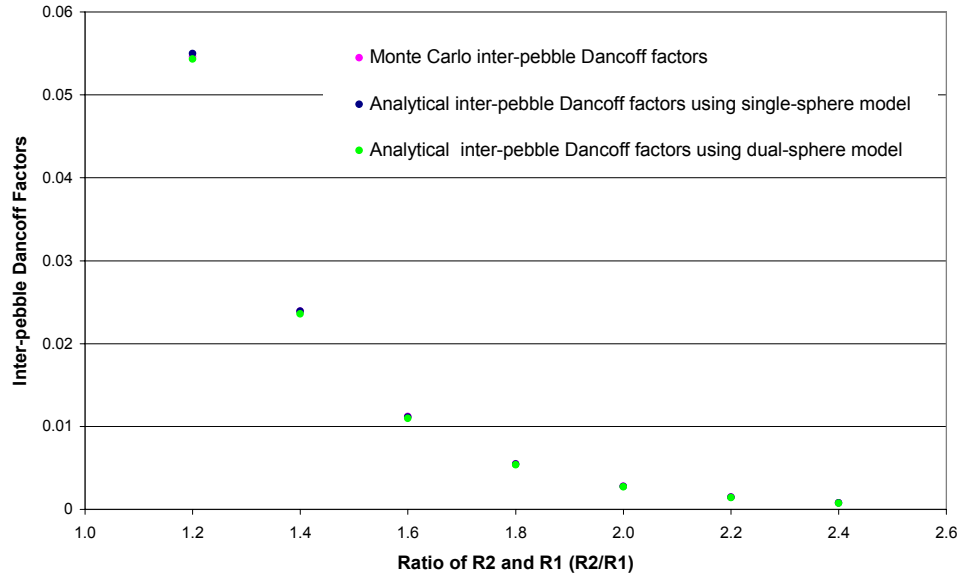
Figure 4.8 Comparisons between analytical and Monte Carlo inter-pebble Dancoff factors at packing fraction 5.76%

It can be seen that both models give excellent results, with good agreement with Monte Carlo results for different values of R_2/R_1. It should be noted that this agreement is partly due to an accurate calculation of P_2, which is the average probability that a neutron escaping from the fuel region in a pebble enters the fuel region in another pebble without collision. We used direct Monte Carlo simulation to get P_2. To illustrate the importance of this, we also used an approximate expression given in Eq. (4.55) to calculate P_2 and the results are compared in Table 4.5.

Table 4.5 Comparisons of P_2 using Eq. (4.55) and Monte Carlo method

R_2/R_1 (R_1=2.5cm)	P_2 [from Eq. (4.55)]	P_2 [from Monte Carlo]
1.2	0.4990	0.4406
1.4	0.2937	0.1996
1.6	0.1898	0.0945
1.8	0.1305	0.0466
2.0	0.0939	0.0238
2.2	0.0699	0.0125
2.4	0.0535	0.0067

Although a white boundary was set on the outer surface of the fuel pebble, the assumption of an exponential distribution function for $H(S)$ does not give a correct value of P_2 using Eq. (4.55). When we studied the microsphere particles distributed stochastically in the moderator, the assumption of an exponential chord length PDF between microspheres yields very good results for infinite medium Dancoff factors. However, when we used the same assumption for fuel pebbles within a VHTR core, inaccurate results were obtained, which indicates that the assumption of an exponential chord length PDF between two pebbles is not valid.

4.3.5.4 Comparison of fuel pebble Dancoff factors with Bende's results

- Intra-pebble Dancoff factors

We also used Monte Carlo benchmark results from Bende et al. (see Fig. 7 in reference [48]) to verify the analytical results from Eq. (4.35) (single-sphere model) and Eq. (4.63) (dual-sphere model) to calculate average inter-pebble Dancoff factors for fuel

kernels in a fuel pebble. The parameters used by Bende are listed in Table 4.6 and the results are presented in Table 4.7.

Table 4.6 Quantities of parameters used by Bende et al

Parameters	Quantities	Unit
r	0.01&0.025	cm
$2d = 2(R\text{-}r)$	0.021	cm
$(R_1)_{nom}$	2.5	cm
$1/\lambda$	0.4097	cm^{-1}

Table 4.7 Results comparison for average Dancoff factor in a fuel pebble

$R_1 /(R_1)_{nom}$	R_1 (cm)	Results with single-sphere model $\overline{C^{intra}}/C^{s,\infty}$	Results with dual-sphere model $\overline{C^{intra}}/C^{d,\infty}$	Benchmark results from Bende $\overline{C^{intra}}/C^{d,\infty}$
$r = 0.01cm \quad frac = 1.65\%$				
2.00	5.0	0.75	0.74	0.72
1.00	2.5	0.57	0.56	0.55
0.50	1.25	0.37	0.36	0.34
0.25	0.625	0.22	0.20	0.19
$r = 0.025cm \quad frac = 8.59\%$				
2.00	5.0	0.89	0.88	0.88
1.00	2.5	0.79	0.77	0.79
0.50	1.25	0.62	0.60	0.61
0.25	0.625	0.42	0.39	0.39

Generally speaking, both single-sphere and dual-sphere models give good results. It is interesting to see that although the benchmark results were obtained from an MCNP

lattice model [48], while our analytical results are based on a stochastic distribution model, they are reasonably close to each other. However, when we compare our analytical results with our Monte Carlo benchmark results based on a RSA stochastic model, the agreement is not very good for the lower packing fractions. This contradiction indicates that the Dancoff factor is very sensitive to the packing scheme when the fuel particles in a fuel pebble are modeled at realistic lower packing fractions. This in turn indicates that the simulation results will depend on the fuel pebble manufacture process.

- Inter-pebble Dancoff factors

We will use the Monte Carlo benchmark results of Bende et al. (see Fig. 8 in reference [48]) to verify our analytical results for average inter-pebble Dancoff factors for fuel kernels using single-sphere and dual-sphere models. Bende used a fuel pebble model with a white boundary to represent randomly packed fuel pebbles in an infinite medium. For each fuel pebble, the radius of the fuel region was fixed at $R_1 = 2.5 cm$, and the radius of the fuel pebble R_2 was adjusted to be $1.0R_1$, $1.1R_1$, $1.2R_1$, $1.5R_1$ and $3.0R_1$. Within a fuel pebble, the fuel particles were modeled as a lattice structure. The average Dancoff factor normalized to the infinite medium Dancoff factor C / C^∞ is given as a function of R_2 / R_1 and $C = \overline{C^{intra}} + \overline{C^{inter}}$. The analytical results for both single-sphere and dual-sphere models were compared with these benchmark results in Table 4.8.

114

Table 4.8 Results comparison for average Dancoff factor between fuel pebbles

R_2/R_1	Analytical results using single-sphere model $\dfrac{\overline{C^{intra}}+\overline{C^{inter}}}{C^{s,\infty}}$	Analytical results using dual-sphere model $\dfrac{\overline{C^{intra}}+\overline{C^{inter}}}{C^{d,\infty}}$	Benchmark results from Bende $\dfrac{\overline{C^{intra}}+\overline{C^{inter}}}{C^{\infty}}$
$r = 0.01cm$ $frac = 1.65\%$			
1.0	1	0.97	1
1.1	0.84	0.82	0.84
1.2	0.76	0.74	0.72
1.5	0.65	0.63	0.605
3.0	0.58	0.56	0.55
$r = 0.025cm$ $frac = 8.59\%$			
1.0	1	0.98	1
1.1	0.93	0.92	0.935
1.2	0.89	0.88	0.87
1.5	0.83	0.82	0.84
3.0	0.79	0.78	0.8

It can be seen that both models give good agreement. It is worth discussing the case when $R_2/R_1 = 1.0$. This corresponds to the infinite medium case, i.e. fuel particles are distributed in an infinite background medium. In this case the sum of the intra-pebble and inter-pebble Dancoff factors should equal the infinite medium Dancoff factor, or

$(\overline{C^{intra}}+\overline{C^{inter}})/C^{\infty} =1$. The single-sphere model predicts this value exactly while the

dual-sphere model does not. If we look back at the definitions of $\overline{C^{intra}}/C^{x,\infty}$, $P_{1,x}$, $P_{2,x}$,

$P_{3,x}$, and $P_{t,x}$ ($x = s$ or d), some relations among them should hold. In particular,

$$\frac{\overline{C^{intra}}}{C^{x,\infty}} = 1 - P_{1,x} \tag{4.65}$$

and

$$\frac{P_{3,x}}{C^{x,\infty}} = 1 - P_{t,x} \tag{4.66}$$

The single-sphere model preserves these relations by inspection of Eqs. (4.31), (4.46), (4.47) and (4.48). However, it can be shown that the dual-sphere model does not satisfy these relations exactly, indicating that the expression for the Dancoff factor based on the dual-sphere model may not be accurate. Eqs. (4.65) and (4.66) suggest an approach to improve the dual-sphere model or develop alternative models accounting for the coating regions. Future research will focus on this topic.

4.3.5.5 Analytical intra-compact and inter-compact Dancoff factors

According to the description of the previous section, intra-compact and inter-compact Dancoff factors were calculated by Monte Carlo simulation and compared to our analytical results. Results will be given for infinite cylinder and finite cylinder configurations.

4.3.5.5.1 Infinite cylinder

Results are shown for infinite cylinder Dancoff factors in this section.

- Intra-compact Dancoff factors

Results are compared at different volume packing fractions ranging from 2.00% to 28.92%. Numerical data in both single-sphere and dual-sphere models are plotted in Figure 4.9, along with the Monte Carlo results.

Figure 4.9 Comparison between analytical and Monte Carlo intra-compact Dancoff factors for infinite height compacts (nominal packing fraction is 28.9%)

It is interesting to see that the single-sphere model underestimates the results and dual-sphere model overestimates the results compared to the benchmark Monte Carlo simulations over all packing fractions. This is similar to the results for the infinite medium Dancoff factors. The dual-sphere model yields better results than the single-sphere model for lower packing fractions but is worse at higher packing fractions. In general, the single-sphere model gives good acceptable results for the entire range of packing fractions.

- Inter-compact Dancoff factors

The volume packing fraction of the fuel particles is fixed at 28.92% for the inter-compact Dancoff factor computation, while the flat-to-flat distance of the hexagonal moderator cell was varied. The results are presented in Figure 4.10.
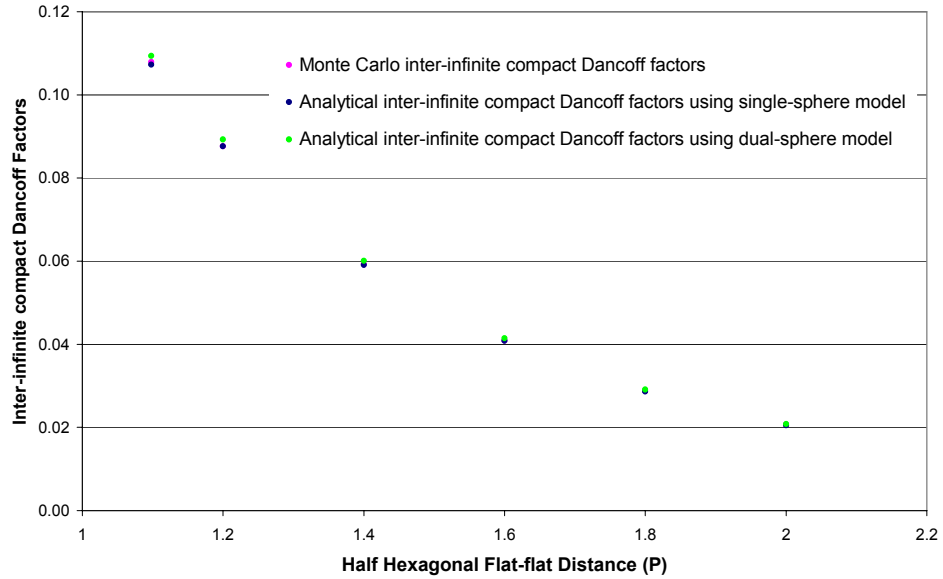
Figure 4.10 Comparisons between analytical and Monte Carlo inter-compact Dancoff factors at packing fraction 28.9%

Similar to what we have seen with the inter-pebble Dancoff factor results, both models predict the inter-compact Dancoff factors reasonably well and the single-sphere model gives better results overall. It is noted that the analytical results calculate P_2 from an inexpensive Monte Carlo simulation. To assess the validity of our analytical expression for P_2, Table 4.9 compares P_2 as from Eq. (4.59) with the Monte Carlo results.

Table 4.9 Comparisons of P_2 using Eq. (4.59) and Monte Carlo method

P(cm)	P_2 [from Eq. (4.59)]	P_2 [from Monte Carlo]
1.097875	0.4442	0.4022
1.2	0.3853	0.3334
1.4	0.2978	0.2295
1.6	0.2360	0.1607
1.8	0.1911	0.1140
2	0.1575	0.0820

The results in Table 4.9 indicate that the exponential assumption for the chord length PDF $H(S)$ between two fuel compacts, which leads directly to the expression for P_2 in Eq. (4.59), is questionable. This assumption leads to a large overestimation in P_2, especially when the ratio of the fuel compact region to the lattice region is large. Although these results are not reported here, the inter-compact Dancoff factors using the analytical expression for P_2 are consistent with the poor estimation of P_2. This shows that an accurate estimation of P_2 plays an important role in the inter-compact Dancoff factors as it did earlier with the calculation of inter-pebble Dancoff factors.

4.3.5.5.2 Finite cylinder

Let us now consider the calculation of Dancoff factors for finite cylinders. In this section, we will show the results of intra-compact and inter-compact Dancoff factors for finite cylindrical compacts using analytical and Monte Carlo methods. For both Dancoff factor calculations, the volume packing fraction of fuel particles is fixed at 28.92% within the compact and the height of the hexagonal cell is varied from 2*D to 100*D, where D is the diameter of the fuel compact.

- Intra-compact Dancoff factors

The following Figure 4.11 shows the results for the intra-compact Dancoff factors as a function of compact height. Similar to the intra-compact Dancoff factor for an infinite medium, the single-sphere model overestimates and the dual-sphere model underestimates the results, over the range of heights. Overall, the single-sphere model gives significantly more accurate results than the dual-sphere model, as can be seen from the plot.
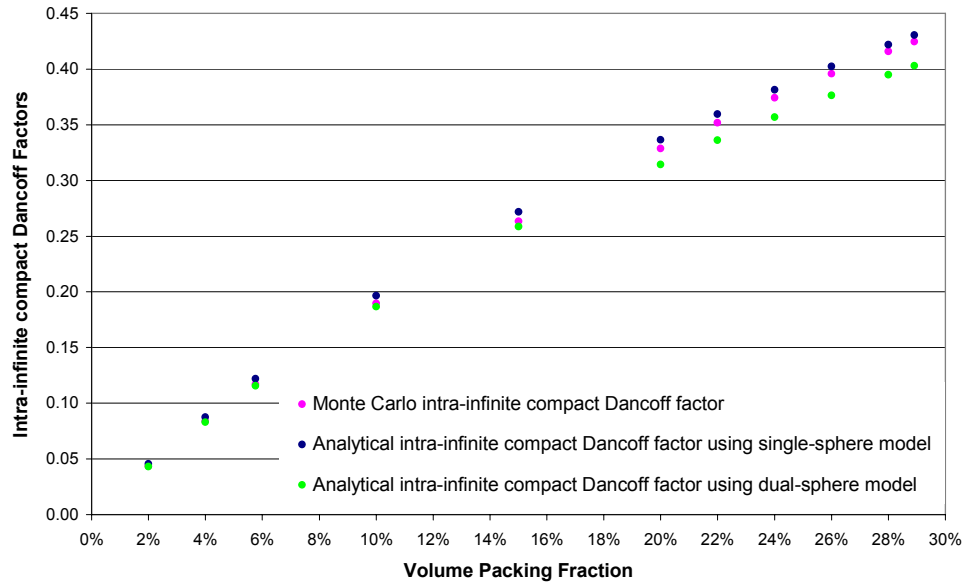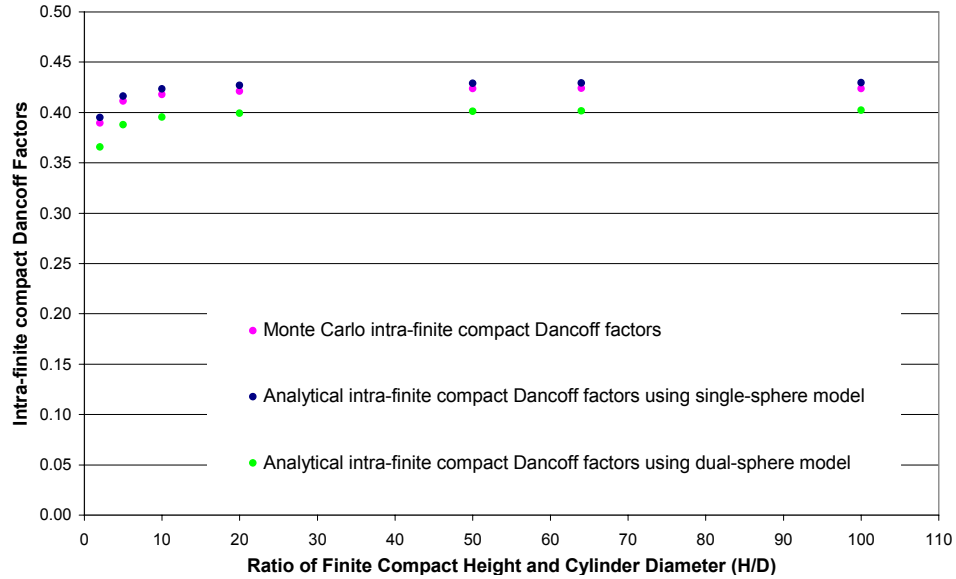
Figure 4.11 Comparisons between analytical and Monte Carlo intra-compact Dancoff factors for finite height compacts

- Inter-compact Dancoff factors

Results are shown in Figure 4.12. We can see when the ratio of height to diameter is small, less than 10, both the single-sphere and dual-sphere model give very poor results, significantly overestimating the inter-compact Dancoff factor. Once this ratio becomes larger than 20, the agreement is much better and the single-sphere model gives excellent agreement with Monte Carlo simulations. In practice, when we analyze the fuel compact, the ratio is normally about 64 and within the accurate results range.
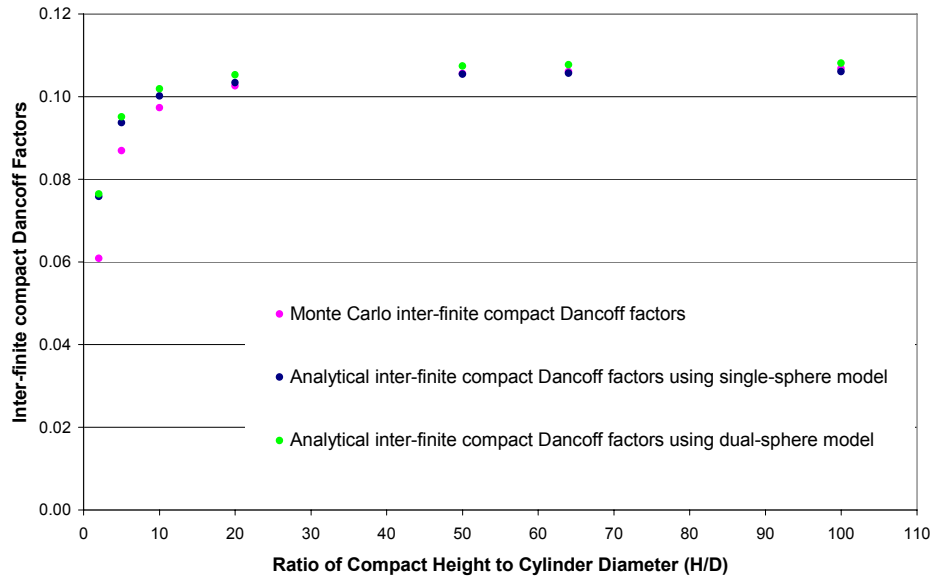
Figure 4.12 Comparisons between analytical and Monte Carlo inter-compact Dancoff factors at packing fraction 28.92%

4.3.5.6 Final remarks on Dancoff factor models

In section 4.3.5, numerical results based on the analytical formulas for Dancoff factors derived in section 4.3.2 were compared with Monte Carlo benchmark results based on the RSA algorithm. Those comparisons are for both pebble-bed and prismatic VHTRs.

Overall, the single-sphere model gives better accuracy than the dual-sphere model, especially in predicting the intra-pebble and intra-compact Dancoff factors. This was explained by noting that basic collision probability relationships were satisfied by the single-sphere model but not the dual-sphere model. However, the single-sphere model does not account for the coating regions, which would seem to be important. This indicates a potential line of inquiry to improve the existing dual-sphere model, which is physically more satisfying than the single-sphere model, or to find another model which

does satisfy the basic collision probability relationships and accounts for the presence of the coating regions.

The importance of the actual packing geometry was seen in the analysis of the intra-pebble Dancoff factors. Our analytical model, predicated on the PDF for a stochastic medium, gave worse results than a lattice-based Monte Carlo simulation, when compared to a Monte Carlo benchmark of the stochastic medium. This phenomenon suggests that the packing schemes for stochastic media have a strong impact on the simulation and this in turn implies that the manufacturing process, if it affects the packing geometry, may have a strong impact on the simulation results. Determination of how to set up a benchmark simulation model which is closest to the actual packing geometry would be very helpful for obtaining accurate simulation results and would be useful for assessing the analytical model.

In predicting the inter-pebble and inter-compact Dancoff factors, both single-sphere and dual-sphere models give good agreement with benchmark results. This is due to the minor impact of the coating region of fuel particles on the inter-volume computations. In this case, the first-flight escape probability (P_2) for a pebble or compact plays a much more important role.

CHAPTER 5

Random Packing of Microspheres

5.1 Introduction

In previous chapters, the RSA algorithm has been used to generate physical realizations of a stochastic medium filled with randomly dispersed TRISO fuel particles, or microspheres. Those physical realizations were used for benchmark computations. Some comparisons between analytical and Monte Carlo results have indicated that different packing schemes can give markedly different Monte Carlo simulation results. For instance, when we compared the intra-pebble and inter-pebble Dancoff factors with the Monte Carlo benchmark results, the analytical results gave poor agreement with our own benchmark based on an RSA-based simulation model, but there was good agreement with the benchmark results of Bende et al. [48] based on a lattice structure simulation model.

The discrepancy of benchmark results using different packing models indicates the need for research on packing schemes for stochastic media and their impact on the neutronic analysis. This is particularly true for VHTR designs, where the different methods for packing identical microspheres yield different statistical properties and give different simulation results. From an engineering point of view, the experimental result is the most important benchmark. In this sense, the study of stochastic packing of fuel particles is important for finding the most suitable model that matches the real

distribution of fuel particles in the stochastic media and also gives the closest results to experimental measurements if those data can be obtained.

The study of randomly packed microsphere is a very general broad topic covering many fields in science and engineering such as crystallography, biology, statistics, solid physics, and chemistry [36], going well beyond the field of nuclear engineering applications. In the dissertation, we only explored some basic properties and simple packing models closely related to VHTR neutronic analysis. The following is a general literature review conducted with the hope that it will be a good source for future research work in packing schemes for stochastic media.

In this chapter, different packing schemes, based on lattice structure, jiggling algorithms, and RSA structure, are examined. The latter two are referred to as stochastic distribution packing schemes. In each structure, two volume packing fraction (VPF) cases are investigated: 28.92% and 5.76%, corresponding to prismatic and pebble bed VHTRs.

The chord length PDF between two microspheres is obtained as a statistical measurement that shows the differences among different packing schemes. The impact of packing on the neutronic analysis is also studied in terms of infinite medium Dancoff factor calculations for a single fuel kernel. These benchmark results may be very useful for checking the computational accuracy of approximate models, such as chord length sampling [17,55], used to analyze VHTR configurations.

5.2 Review of Previous Work Related to Random Packing of Equal Spheres

5.2.1 Random packing and description of geometrical statistics

Research on the random packing of hard spheres was originally performed when people studied geometrical models to represent the structure of liquids [70,71,72,73,74,75]. Many important concepts were proposed in early years but are still significant today in research on stochastic media. The basic quantities that describe a random system include: average density (especially the upper limit in random close packing), the distribution of numbers of neighbors (or the average number of contacts) in random close/loose packings, radial distribution functions (now superseded by the term "nearest-neighbor function"), pair correlation function (it equals the nearest-neighbor function minus one), and the chord length probability density function. Detailed definitions of these distributions can be found in the early papers mentioned above and a recent book written by Torquato [36]. The early pioneer J.D. Bernal gave a classical lecture [76] summarizing the experimental and theoretical progress made through 1964, which drew people's attention to a new subject he called "statistical geometry". In his works, only the high-density state or random close-packing was thoroughly studied from a pure geometrical perspective. No physical or thermodynamic considerations were accounted for. Later, Finney [77] presented a polyhedral analysis of the random packing model using basic statistical descriptors and took a further step towards establishing the new science "statistical geometry". Subsequently, many researchers followed these early works to expand the basic ideas of stochastic modeling into many science and engineering fields, such as the modeling of the atomic arrangements for noncrystalline

metallic solids [78], amorphous metals [85], and stochastic fuel for nuclear reactor cores [15].

5.2.2 Computer simulation of random packing

Corresponding to the development of experimental work and geometrical statistical analysis on random media, computer simulation experienced a long development period and is playing an important role today in modeling and studying stochastic structures. Generally speaking, two types of random packing schemes exist: sequential deposition schemes and collective rearrangement schemes. In sequential deposition packing, each hard sphere is placed randomly in a container one at a time and all the previous spheres previously placed in the container will affect the placement of the new sphere, in addition to other constraints imposed by the size of the container or gravity, for example. According to the restrictions placed on the new sphere, several algorithms exist in the sequential deposition schemes and will be explained below. In collective rearrangement packing, the center points of all the spheres are generated randomly at the start of the process and then a collective rearrangement procedure is performed to eliminate overlapping among all the spheres generated initially and to satisfy other constraints as needed. Several algorithms exist which typically are different due to the different procedures to eliminate overlapping spheres, and these will be explained later.

In 1959, in one of the earliest applications, Bernal tried a Monte Carlo approach to model close-packed liquids created by compression from gas [70]. This was the first example of a collective rearrangement method. In 1967, Mason presented some statistical results from using this simulation approach [79]. The process to eliminate overlapping

was a little more complex, manipulating two overlapped spheres to move apart along the line between their centers or to increase the sphere size slightly after the elimination procedure. The elimination and size change procedures were alternately repeated until a high volume packing fraction was reached. Finney used the same algorithm to give more interesting results in 1976 [83]. In 1985, a new algorithm was proposed by Jodrey and Tory [84] based on the previous collective rearrangement process. The major change is that during each step only the worst overlap was removed between two spheres and a subtle radius shrinking process was indirectly applied to facilitate the removal of overlaps. Before that work, overlapping removal and radius change were separate steps. Two years later, Clarke and Wiley [85] published another collective rearrangement algorithm. In this algorithm, the moving direction of a sphere to eliminate overlapping was the vector sum of all the coordinates of spheres with which the moving sphere is overlapped, and a vibrating (jiggling) process was utilized to prevent convergence to a low-density packing. This new algorithm was successfully applied to equal and unequal spheres. Based on Clarke and Wiley's work, Murata et al.[15] employed a random vector synthesis method to calculate the moving direction of a sphere in removing the overlapping and successfully obtained a high packing density in modeling the spherical fuel particles in a high temperature gas-cooled reactor fuel.

For sequential deposition packing, several algorithms were proposed by many researchers as early as 1960. All the algorithms start with a seed cluster (the first deposited sphere or several spheres on the vertices of a polyhedron structure) and then the other spheres are brought in one at a time according to some criteria. In 1972, Bennett [80] studied two models of deposition depending on two criteria: the first is a "global"

criterion that a new sphere should be deposited at a site nearest to the original starting

seed cluster center and the second is a "local" criterion that the new sphere should be

deposited at a site which has the least distance to the three other contacted spheres. In

either criterion, three contacts were required for each new sphere. Meanwhile in another

paper, Visscher and Bolsterli [81] presented a different algorithm in which the additional

deposition was influenced by a vertical gravitational force. The new sphere position was

randomly selected at the top and dropped down following a vertical path to the stable

position, which has stable contacts with three other spheres already packed. Later this

method was called the "ballistic deposition model". In the same year, a very interesting

deterministic algorithm was given by Adams and Matheson [82] using a tetrahedral

structure to admit new spheres on vertices. Although the approach is deterministic, the

packing shows the same statistical properties as the close random packing. In 1992,

Jullien et al. [86] published a paper summarizing all the previous sequential deposition

models and gave a comparison among them in terms of several basic statistical quantities

such as density and radial distribution functions.

The above algorithms, categorized as either collective rearrangement or sequential

deposition, are mainly for random close packing, which means at very high packing

density up to 63%-64%. In some practical applications, random close packing is only the

first step, and then additional steps need to be taken to decrease the packing density, such

as done by Murata for modeling particle fuel in a VHTR [15]. For low packing density

systems, say less than 30%, can we directly use some algorithm to generate a random

system? The answer is definitely YES. As early as 1962, Bernal [76] introduced a method

to generate sequentially coordinates of sphere centers at random, but each new sphere

was prohibited from overlapping with others already generated. As he said, the method was a random model, but it was far from being a close packing. However, this gave a good indication that we may use it to generate low packing density random systems. Later people called this sphere packing process "Random Sequential Addition" (RSA). In 1966, Widom [24] compared the system generated using RSA with a system in thermodynamic equilibrium. The highest packing density ("jammed density") was given analytically. The RSA algorithm is still used widely because of its simplicity. It is worth mentioning that Brown [31] proposed a fast RSA algorithm that requires a computing time of $O[N]$, where N is the total number of spheres.

5.3 Impact of Random Packing on Benchmark Calculations

In VHTR analysis, random mixtures of identical spheres are encountered because the fuel particles are hard spheres and are randomly distributed in a graphite matrix. Many simulation packing methods have been proposed to model the arrangement of these fuel particles, including lattice and random structures. [11,12,20,21].

In the introduction to this chapter, we mentioned three major packing structures were used for the analysis of particle fuel: body-centered lattice structure, a "jiggled" lattice structure, and a random RSA structure. These models were compared using two quantities: the chord length PDF between two fuel particles and the infinite medium Dancoff factor for a fuel particle.

Among these three structures, we believe the jiggled model would be the one closest to the real structure if the fuel particle distribution is deemed homogeneous and isotropic in the graphite matrix background. For example, Murata [15] associated the modeling of fuel particles with the manufacturing process with two steps. The first step

was modeling a random close packing of graphite overcoated fuel particles, and the second step was to shrink the oversized fuel particles back to normal size by removing the graphite and letting it become part of the matrix. According to Murata, the resultant distribution was more homogeneous and more isotropic. A jiggled lattice structure can produce a similar distribution and to some extent mimics the manufacturing process. The detailed description is given in the following sections.

5.3.1 Alternative packing structures for stochastic mixtures of microspheres

Figure 5.1 illustrates the basic procedure used to realize different packing structures. A small cubic lattice element consisting of a microsphere fuel particle at the center was sized to preserve the packing fraction of fuel particles in the graphite matrix. About 20M fuel particles are modeled in the configuration. In order to realize a random distribution, each fuel particle is jiggled a little from its original position for each realization of the stochastic geometry. As shown in Figure 5.1, the random displacement is controlled by a series of local sampling processes, i.e. the position of the center of each fuel particle is uniformly sampled within a spherical region with radius R in each realization. The process sweeps over every fuel particle, and no overlapping is allowed. By adjusting R (typically a multiple of R) from small values to large values, the distribution of fuel particles will look more random and homogeneous. With increasing R, a fuel particle may cross the boundary of a lattice box.
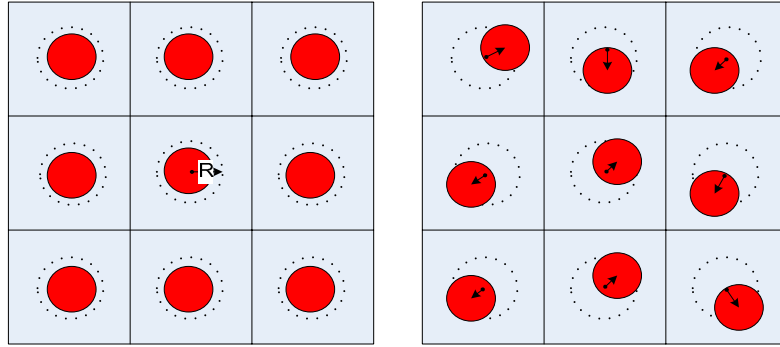
Figure 5.1 From lattice to jiggled lattice structure

Lattice Structure   Jiggling within $1.0*R_s$ RSA Structure
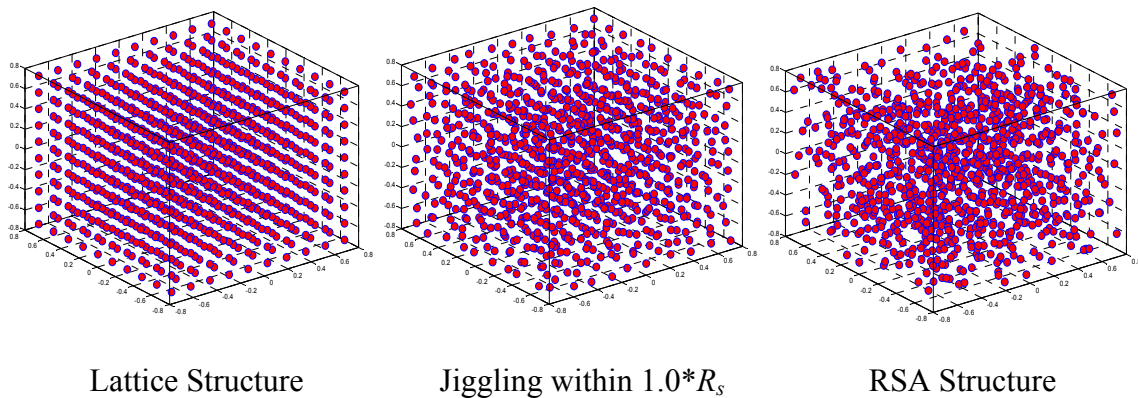
Figure 5.2 Microsphere distribution in different packing schemes

Figure 5.2 shows a direct visual comparison among lattice, jiggling and RSA structures in a 3D physical realization. It is clear from the Figure 5.2 that jiggling makes the distribution more homogeneous and isotropic than RSA. In particular, the RSA model results in clumping of the fuel particles while the jiggling process inhibits this from occurring.

Lattice, jiggled lattice, and RSA structures were compared by analyzing a fuel particle geometry including fuel kernel and coating regions taken from the NGNP report [2]. Two packing fractions were studied, 28.92% and 5.76%. A ray-tracing method was employed to calculate both the chord length PDFs and the infinite medium Dancoff factors for each of the structures. For the random structures (jiggled lattice and RSA), a

total of 100 realizations were generated, and the chord length PDF and Dancoff factor results were ensemble-averaged over the 100 realizations.

5.3.2 Chord length PDFs between microspheres

Figure 5.3 shows the PDFs of chord length between fuel particles at 28.92% and 5.76% packing fractions, corresponding to prismatic and pebble bed VHTRs.
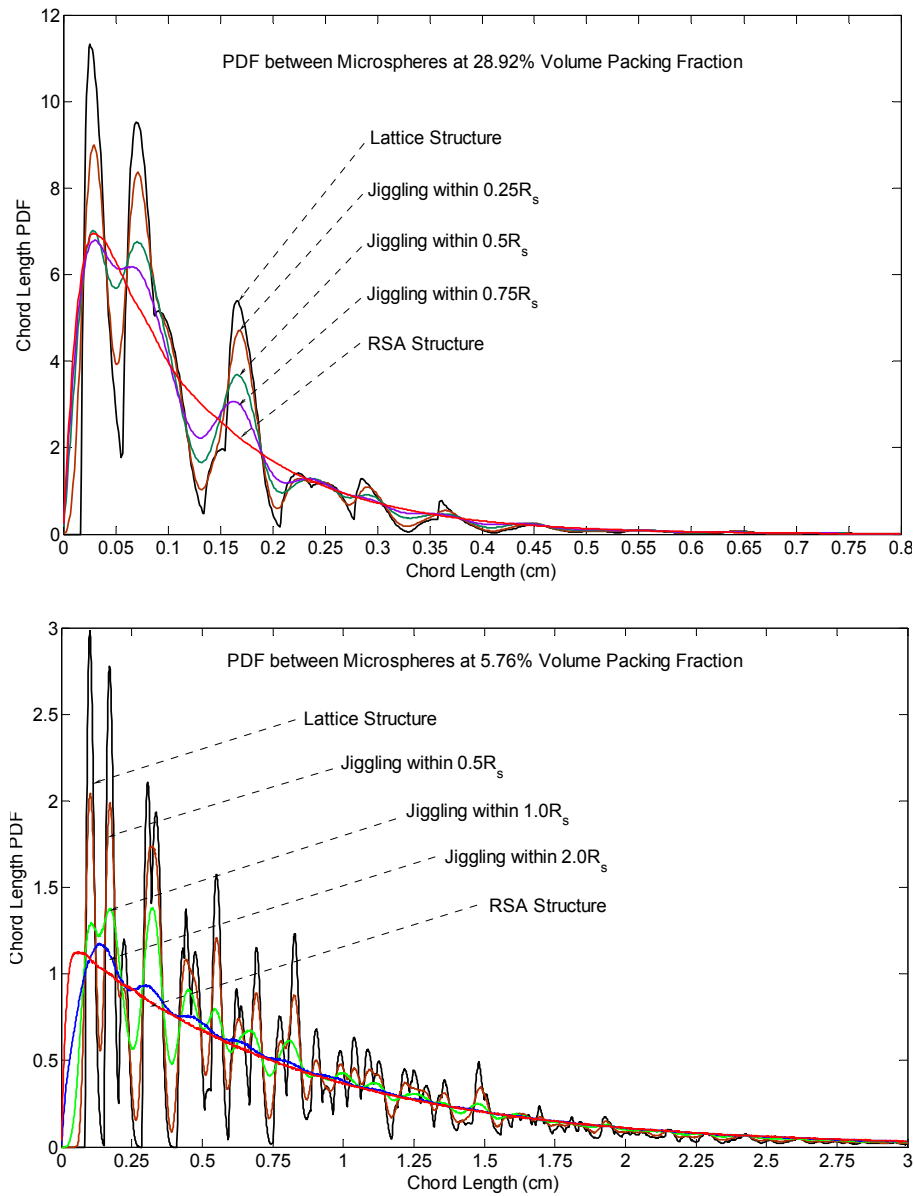
Figure 5.3 PDF of chord length between microspheres

It is interesting that all the curves behave like a damped oscillator except the RSA model. The lattice model has the most oscillatory curve and the oscillations are damped as the amount of jiggling increases, converging to the RSA curve in an oscillatory manner.

Another interesting phenomenon is that for increasing chord length, all the PDFs tend to the RSA curve. We have shown earlier [87] that the decaying part of the RSA curve is exponential, so we can conclude that for large chord lengths with packing fractions characteristic of VHTR particle fuel distributions, the PDF is an exponential function regardless of the packing scheme.

5.3.3 Infinite medium Dancoff factors for microspheres

Table 5.1 presents the resultant Dancoff factors for each of the three packing structures at the two packing fractions.

Table 5.1 Dancoff factors for different packing schemes

Packing Scheme		Dancoff Factor (1 σ)
5.76% VPF		
Lattice Structure		0.3299 (0.0001)
Jiggled Lattice Structure	$0.5R_s$	0.3324 (0.0001)
	$1.0R_s$	0.3363 (0.0001)
	$2.0R_s$	0.3375 (0.0001)
	$3.0R_s$	0.3386 (0.0001)
RSA Structure		0.3477 (0.0002)
28.92% VPF		
Lattice Structure		0.7314 (0.0001)
Jiggled Lattice Structure	$.25R_s$	0.7291 (0.0001)

	$.33R_s$	0.7284 (0.0001)
	$.40R_s$	0.7279 (0.0002)
	$.50R_s$	0.7275 (0.0001)
RSA Structure		0.7331 (0.0001)

The results show that the fuel particle arrangement has a significant effect on the neutronic analysis. For example, for 5.76% VPF, the Dancoff factor increases by 3% from a lattice to a highly jiggled lattice, but this is still 3% less than the RSA value. On the other hand, the opposite trend is observed for the 28.92% VPF case where the Dancoff factor decreases by about .5% with increasing jiggling in the lattice structure. Since the Dancoff factor has a strong effect on the resonance self-shielding, these changes will have a significant effect on k_{eff} for a VHTR configuration. This implies that the manufacturing process for packing the fuel particles into the fuel compact or fuel pebble has a strong effect on the neutronic analysis of the reactor. Modeling fuel particles in VHTR using a realistic packing scheme that represents the manufacturing process would yield more accurate neutronic analyses.

CHAPTER 6

Summary and Conclusions

6.1 Summary and Conclusions

For the analysis of VHTR systems, the well-known "double heterogeneity" and the stochastic distribution of fuel microspheres present substantial challenges to the conventional neutronic analysis methods. In this dissertation, these challenges are addressed by developing a methodology for analyzing microspheres that will be accurate enough in both static and time-dependent configurations and yet efficient enough to be used for routine analyses. This effort includes creation of a new physical model, development of a simulation algorithm, and application to real reactor configurations with comparison to benchmark results.

The thesis starts with a general neutronic analysis for a prismatic type VHTR using the MCNP5 Monte Carlo code and the coupled depletion code ORIGEN (Monteburns). The explicit modeling of VHTR configurations with these tools has been performed for configurations ranging from a microsphere cell to a fuel compact cell to full core. The following conclusions are made:

(1) The effect of the double heterogeneity needs to be accounted for by explicitly modeling the fuel microspheres.

(2) It is acceptable to model the particle fuel as a lattice of microsphere cells that preserves the packing fraction. Moreover, one can place the microspheres at the center of the cubical cells with acceptable results.

(3) Satisfactory results are obtained by using a two-region model to represent the six physical regions in the microsphere cell.

(4) It is important (and straightforward) to avoid clipped cells for both the fuel compact calculations and full-core calculations.

(5) The random distribution of fuel particles has a small effect on the criticality for full core calculations ($\sim 0.15\%$ Δk) with packing fractions characteristic of prismatic VHTRs (28.92%) hence the impact of different random packing schemes is small. The consequence of this is that the microspheres can be modeled on a lattice with acceptable results. In pebble-bed reactors, however, the low packing fraction ($\sim 5.76\%$) will result in the random packing scheme having a larger impact on the results. In any event, it is essential to model the stochastic distribution of fuel particles to obtain an accurate neutronic analysis of a VHTR.

(6) The analysis of the VHTR with full heterogeneous geometry with MCNP5 is computationally expensive. Even with a two-region microsphere model, a full-core MCNP5 calculation is time-consuming. If depletion is added, the computational demand increases rapidly, and traditional Monte Carlo methods are not practical for routine analysis. To address this computational challenge, new models and algorithms need to be developed for VHTR neutronic analysis.

As a result, an alternative method, chord length sampling (CLS), was examined to reduce the computational burden associated with analog Monte Carlo simulation, yet

retaining its accuracy. We have improved on the existing CLS method, developed for 1D and 2D geometry, and have used it to analyze stochastic media representative of VHTR cells: a fuel compact cell and a fuel pebble cell. These analyses include general neutron transport analyses as well as the calculation of Dancoff factors.

The first step was to obtain a chord length PDF for a stochastic medium. Based on the assumption that the PDF is an exponential function, a theoretical chord length PDF was derived and validated by comparison with direct Monte Carlo simulation results at different packing fractions. This chord length PDF was then used to analyze a number of stochastic media (cube, sphere, and cylinder) that were constructed using the RSA (Random Sequential Addition) algorithm. The results are promising and suggest that the theoretical chord length PDF can be used instead of a full Monte Carlo random walk simulation in the stochastic medium, saving orders of magnitude in computational time (and memory demand) to perform the simulation. The results also indicate that the improved CLS method can be used for realistic VHTR configurations for either pebble bed or prismatic reactors.

A similar methodology was developed by Murata [15,16] but his work was based on an empirical distribution of microspheres found by a sphere packing algorithm that was designed to mimic the manufacturing process for TRISO fuel. We have used a theoretical PDF for a stochastic medium.

The Dancoff factor plays an important role in computing accurate resonance integrals for nuclear reactor lattices, hence has a large impact on the generation of few-group cross sections for routine neutronic analysis of reactors. In this thesis, a new formulation of the Dancoff factor is derived by introducing the chord length PDF. This

led to relatively simple expressions for both infinite medium and finite medium Dancoff factors. Using the new expressions, the calculation of Dancoff factors for microsphere fuel particles randomly distributed in prismatic and pebble-bed VHTRs is studied. Two fuel particle models are developed and closed form Dancoff factor expressions for both models are derived based on the assumption that the chord length PDF is exponential, which is the basis for our chord length sampling method. The numerical results from the formulas are compared with Monte Carlo simulation results, and excellent agreement is obtained for a range of parameter values.

When analyzing fuel particles in VHTR, it is found that different packing schemes yield different statistical properties, such as the chord length PDF, and different neutronic behavior in terms of the Dancoff factor. This suggests that accounting for the manufacturing process when modeling the fuel particle distribution in a VHTR would increase the accuracy of the neutronic results. One approach that may model the manufacturing process is the jiggled lattice model presented in the last part of the thesis, which has been compared with both lattice and RSA models. The results show that the jiggled lattice model gives a better visual distribution, i.e. more homogeneous and isotropic than either lattice or RSA models. Moreover, the jiggled lattice algorithm is simpler and uses less machine memory and CPU time than RSA.

6.2 Suggestions for Future Work

Several aspects of this thesis work still need further investigations and are mentioned below:

(1)   A simple iteration scheme is suggested to obtain the effective packing fraction used in the theoretical chord length PDF when we use the CLS method to perform

the neutronic analysis of a finite medium. This scheme appears to be a promising method for correcting for boundary interference but is still not optimal for all VHTR configurations and packing fractions. Additional study is warranted for this method in the future.

(2)   Although the single-sphere model yields very good results for infinite-medium and finite-medium Dancoff factors for VHTR configurations, it does not account for the coating regions of the microsphere fuel particles. This indicates a potential line of inquiry to improve the existing dual-sphere model, which is physically more satisfying than the single-sphere model though it gives poorer results. The alternative is to find another model which satisfies the basic collision probability relationships and also accounts for the presence of the coating regions.

(3)   The jiggled lattice model suggests a simple way to model a more homogeneous and isotropic stochastic system. This gives the possibility to yield a fuel particle distribution in a VHTR that is close to the actual distribution obtained via the manufacturing process. The jiggled lattice model mimics to some extent the same steps as the fuel particle manufacturing process and is close to the scheme introduced by Murata [15]. In order to give the closest results to the actual fuel particle distribution, it would be beneficial to determine an appropriate lattice structure and an optimal displacement parameter that best reproduces the actual distribution obtained as a result of the manufacturing.

BIBLIOGRAPHY

1. A Technology Roadmap for Generation IV Nuclear Energy Systems, GIF-002-00, Generation IV International Form, (Dec. 2002). http://www.ne.doe.gov/genIV/documents/gen_iv_roadmap.pdf

2. P. E. MacDonald, et al., "NGNP Preliminary Point Design – Results of the Initial Neutronics and Thermal-Hydraulic Assessments During FY-03", INEEL/EXT-03-00870 Rev. 1, Idaho National Engineering and Environmental Laboratory (2003)

3. L. Massimo, "Physics of High-temperature Reactors," Pergamon Press, 1976

4. M.G. Stamatelatos and R.J. LaBauve, "Methods for Calculating Group Cross Sections for Doubly Heterogeneous Thermal Reactor Systems," LA-NUREG-6685-MS, 1977

5. P. Wälti, "Evaluation of Grain Shielding Factors for Coated Fuel Particles," *Nucl. Sci. Eng.*, **45**, pp.321-330, 1971

6. M.M. Levine, "Resonance Integral Calculations for 238U Lattices," *Nucl. Sci. Eng.*, **16**, pp.271-279, 1963

7. A. Sauer, "Thermal utilization in the square lattice cell," *J. Nucl. Energy*, **18**, pp.425, 1964

8. L.W. Nordheim, "A New Calculation of Resonance Integrals," *Nucl. Sci. Eng.*, **12**, pp.457-463, 1962

9. X-5 Monte Carlo Team, "MCNP – A General Monte Carlo N-Particle Transport Code, Version 5", LA-UR-03-1987, Los Alamos National Laboratory (2003)

10. F.C. Difilippo, "Monte Carlo Calculations of Pebble Bed Benchmark Configurations of the PROTEUS Facility," *Nucl. Sci. Eng.*, **143**, pp.240-253, 2003

11. R. Plukiene and D. Ridikas, "Modeling of HTRs with Monte Carlo: from a homogeneous to an exact heterogeneous core with microparticles," *Annals of Nuclear Energy,* **30**, pp.1573-1585, 2003

12. W. Ji, J.L. Conlin, W.R. Martin, J.C. Lee and F.B. Brown, "Explicit Modeling of Particle Fuel for the Very-High Temperature Gas-Cooled Reactor," *Trans. Am. Nucl. Soc.,* **92**, pp.236-238, 2005

13. J.R. Johnson, J.R. Lebenhaft, and M.J. Driscoll, "Burnup Reactivity and Isotopics of an HTGR Fuel Pebble," *Trans. Am. Nucl. Soc.* **85**, pp.273-274, 2001

14. T. Mori, K. Okumura, and Y. Nagaya, "Status of JAERI's Monte Carlo Code MVP for Neutron and Photo Transport Problems," *Proc. Monte Carlo 2000 Conference*, Lisbon, pp.625-630, 2000

15. I. Murata, T. Mori, and M. Nakagawa, "Continuous Energy Monte Carlo Calculations of Randomly Distributed Spherical Fuels in High-Temperature Gas-Cooled Reactors Based on a Statistical Geometry Model," *Nucl. Sci. Eng.* **123**, pp.96-109, 1996

16. I. Murata, et al., "New Sampling Method in Continuous Energy Monte Carlo Calculation for Pebble Bed Reactors," *J. Nucl. Sci. Tech.* **34**, pp.734-744, 1997

17. T. Donovan and Y. Danon, "Application of Monte Carlo Chord-Length Sampling Algorithms to Transport Through a Two-Dimensional Binary Statistical Mixture," *Nucl. Sci. Eng.* **143**, pp.226-239, 2003

18. T. Donova and Y. Danon, Y., "HTGR Unit Fuel Pebble k-infinity Results Using Chord Length Sampling," *Trans. Am. Nucl. Soc.* **89**, pp.37-39, 2003

19. M. Armishaw, N. Smith, and E. Shuttlesworth, E., "Particle Packing Considerations for Pebble Bed Fuel Systems," *Proc. ICNC 2003 Conference, JAERI-Conf-2003-019, Tokai-mura, Japan,* 2003

20. F.B. Brown and W.R. Martin, "Stochastic Geometry Capability in MCNP5 for the Analysis of Particle Fuel," *Annals of Nuclear Energy,* **31**, pp.2039-2047, 2004

21. F. B. Brown, W. R. Martin, W. Ji, J. L. Conlin, and J. C. Lee, "Stochastic Geometry and HTGR Modeling with MCNP5," *Proc. Monte Carlo 2005 Topical Meeting*, American Nuclear Society, Chattanooga, TN, April 17–21, 2005, on CD-ROM, American Nuclear Society, LaGrange Park, IL (2005)

22. T.K. Kim, T.A. Taiwo, R.N. Hill, W.S. Yang and F. Venneri, "A Feasibility Study of Reactor-based Deep-burn Concepts," ANL-AFCI-155, Argonne National Laboratory, 2005

23. E.E. Bende, "Plutonium Burning in a Pebble-bed Type High Temperature Nuclear Reactor," Ph.D. Thesis, Delft University of Technology, 1999

24. B. Widom, "Random Sequential Addition of Hard Spheres to a Volume," *J. Chem. Phys.*, **44**, pp.3888-3894 (1966)

25. W. Ji, J.L. Conlin, W.R. Martin, and J.C. Lee, "Reactor Physics Analysis of the VHTGR Core," *Trans. Am. Nucl. Soc.* **91**, pp. 556-558, (2004)

26. J. L. Conlin, W. Ji, J. C. Lee, and W. R. Martin, "Pseudo Material Construct for Coupled Neutronic-Thermal-Hydraulic Analysis of VHTGR," *Trans. Am. Nucl. Soc.* **92**, pp. 225-227, (2005)

27. G. Yesilyurt, W. Ji, S. Prasad, W.R. Martin, and J.C. Lee, "Coupled Nuclear-Thermal-Hydraulics Analysis for VHTR," *Trans. Am. Nucl. Soc.* **96**, pp. 580-581, (2005)

28. Chang H. Oh, et al., "Development of Safety Analysis Codes and Experimental Validation for a Very High Temperature Gas-Cooled Reactor," *INL/EXT-06-01362* Idaho National Engineering and Environmental Laboratory (2006)

29. W. Ji, J.L. Conlin, W.R. Martin, J.C. Lee and F.B. Brown, "Neutronic Analysis to Support Validation of Safety Analysis Codes for the VHTR," *Trans. Am. Nucl. Soc.,* **93**, pp.931-933 (2005)

30. G.B. Zimmerman and M.L. Adams, "Algorithms for Monte Carlo Particle Transport in Binary Statistical Mixtures," *Trans. Am. Nucl. Soc.,* **64**, pp.287-288 (1991)

31. F.B. Brown, "A Fast RSA Method for Fuel Particle Packing," *Trans. Am. Nucl. Soc.*, **94**, pp.571-573 (2006)

32. http://www.nndc.bnl.gov/exfor3/endf00.htm

33. G.L. Olson, D.S. Miller, E.W. Larsen, and J.E. Morel, "Chord length distribution in binary stochastic media in two and three dimensions", *J. Quant. Spectros. Rad. Transfer*, **143**, pp.226-239 (2005)

34. G.L. Olson, J.E. Morel, and E.W. Larsen, "Chord Length Distributions in Binary Stochastic Media in Two and Three Dimensions", *Trans. Am. Nucl. Soc.*, **89**, pp.307-309 (2003)

35. A. Cauchy, *Oeuvres Complètes*, Vol. 2, pp. 174 Gauthier-Villars, Paris, 1908

36. S. Torquato, "Random Heterogeneous Materials: Microstructure and Macroscopic Properties," *Interdisciplinary Applied Mathematics*, Volume 16, Springer-Verlag, New York, 2002

37. G.L. Olson, J.E. Morel, and E.W. Larsen, "Chord Length Distributions in Binary Stochastic Media in Two and Three Dimensions", *Trans. Am. Nucl. Soc.,* 8**9**, pp.307-309 (2003)

38. T.J. Donovan and Y. Danon, "Implementation of Chord Length Sampling for Transport Through a Binary Stochastic Mixture," *Proceedings of the American Nuclear Society Topical Meeting in Mathematics & Computations,* Gatlinburg, TN, April 2003

39. P.A.M. Dirac, "Approximate Rate of Neutron Multiplication for a Solid of Arbitrary Shape and Uniform Density," *Declassified British Report MS-D-5*, Part I, 1943

40. A.M. Weinberg and E.P. Wigner, "The physical theory of neutron chain reactors," pp. 775-776 (1958)

41. J.J. Duderstadt and L.J. Hamilton, "Nuclear reactor analysis," pp. 434-435 (1976)

42. S.M. Dancoff and M. Ginsburg, "Surface resonance absorption in a close-packed lattice," *CP-2157*, (1944)

43. G.I. Bell and S. Glasstone, "Nuclear reactor theory," pp. 122-125, 115-117(1979)

44. L.W. Nordheim, "The theory of resonance absorption," *Proc. Symp. Appl. Math.* **11**, pp.58 (1961)

45. W. Rothenstein, "Collision probabilities and resonance integrals for lattices," *Nucl. Sci. Eng.*, **7**, pp.162-171 (1960)

46. L.W. Nordheim, "A new calculation of resonance integrals," *Nucl. Sci. Eng.*, **12**, pp.457-463 (1962)

47. RSICC Computer Code Collection, 1999b. MICROX-2 – Code System to Create Broad-Group Cross Sections with Resonance Interference and Self-Shielding from Fine-Group and Pointwise Cross Sections. RSICC Code Package PSR-374, ORNL

48. E.E. Bende, A.H. Hogenbirk, J.L. Kloosterman and H. Van Dam, "Analytical Calculation of the Average Dancoff Factor for a Fuel Kernel in a Pebble Bed High-Temperature Reactor," *Nucl. Sci. Eng.* **133**, pp.147-162 (1999)

49. A. Talamo, "Analytical Calculation of the Average Dancoff Factor for Prismatic High-Temperature Reactors," *Nucl. Sci. Eng.* **156**, pp.343-356 (2007)

50. J.L. Kloosterman and A.M. Ougouag, "Comparison and Extension of Dancoff Factors for Pebble-Bed Reactors," *Nucl. Sci. Eng.* **157**, pp.16-29 (2007)

51. K.M. Case, F.DE Hoffmann and G. Placzek, "Introduction to the theory of neutron diffusion," Volume I, pp. 19-22 (1953)

52. G.L. Olson, D.S. Miller, E.W. Larsen, and J.E. Morel, "Chord length distribution in binary stochastic media in two and three dimensions", *J. Quant. Spectros. Rad. Transfer*, **143**, pp.226-239 (2005)

53. A. Sauer, "Approximate Escape Probabilities," *Nucl. Sci. Eng.*, **16**, pp.329-335 (1963)

54. A. Cauchy, *Oeuvres Complètes*, Vol. 2, pp. 174 Gauthier-Villars, Paris (1908)

55. W. Ji and W.R. Martin, "Monte Carlo Simulation of VHTR Particle Fuel with Chord Length Sampling," *Proceedings of M&C+SNA2007*, Monterey, California, April 15-19 (2007)

56. N.R. Corngold, "On the Collision Probability for the Infinite Cylinder,", *Annals of Nuclear Energy*, **29**, pp.1151-1155 (2002)

57. A.M. Kellerer, "Considerations on the Random Traveral of Convex Bodies and Solutions for General Cylinders," *Radiation Research*, Vol. **47**, No. **2**, pp. 359-376 (1971)

58. U. Mäder, "Chord Length Distribution for Circular Cylinders," *Radiation Research*, Vol. **82**, No. **3**, pp. 454-466 (1980)

59. I. Carlvik, "Collision Probabilities for Finite Cylinders and Cuboids," *Nucl. Sci. Eng.*, **30**, pp.150-151 (1970)

60. G. Marleau, R. Roy and A. Hébert, "Analytic Reductions for Transmission and Leakage Probabilities in Finite Tubes and Hexahedra," *Nucl. Sci. Eng.*, **104**, pp.209-216 (1990)

61. Y.A. Chao, M.B. Yarbrough and A.S. Martinez, "Approximations to Neutron Escape Probability and Dancoff Correction," *Nucl. Sci. Eng.*, **78**, pp.89-91 (1981)

62. J.A. Thie, "A Simple Analytical Formulation of the Dancoff Correction," *Nucl. Sci. Eng.*, **5**, pp.75-77 (1959)

63. Y. Fukai, "New Analytical Formula for Dancoff Correction for Cylindrical Fuel Lattices," *Nucl. Sci. Eng.*, **9**, pp.370-376 (1961)

64. I. Carlvik, "The Dancoff Correction in Square and Hexagonal Lattices," *Nucl. Sci. Eng.*, **29**, pp.325-336 (1967)

65. S. Fehér, J.E. Hoogenboom, P.F.A. de Leege and J. Valkó, "Monte Carlo Calculation of Dancoff Factors in Irregular Geometries," *Nucl. Sci. Eng.* **117**, pp.227-238 (1994)

66. R.K. Lane, L.W. Nordheim, and J.B. Samson, "Resonance Absorption in Materials with Grain Structure," *Nucl. Sci. Eng.*, **14**, pp.390-396 (1962)

67. L.W. Nordheim, "Resonance Absorption in Materials with Grain Structure (Addendum)," *Nucl. Sci. Eng.*, **16**, pp.337-338 (1963)

68. R.A. Lewis and T.J. Connolly, "Resonance Absorption in Particles," *Nucl. Sci. Eng.*, **24**, pp.18-25 (1966)

69. G.I. Bell, "A Simple Treatment for Effective Resonance Absorption Cross Sections in Dense Lattices," *Nucl. Sci. Eng.*, **5**, pp.138-139 (1959)

70. J.D. Bernal, "Geometrical Approach to the Structure of Liquids," *Nature*, **183**, pp.141-147 (1959)

71. J.D. Bernal, "Geometry of the Structure of Monatomic Liquids," *Nature*, **185**, pp.68-70 (1960)

72. G.D. Scott, "Packing of Spheres," *Nature*, **188**, pp.908-910 (1960)

73. J.D. Bernal, "Co-ordination of Randomly Packed Spheres," *Nature*, **188**, pp.910-911 (1960)

74. G.D. Scott, J.D. Bernal, J. Mason and K.R. Knight, "Radial Distribution of the Random Close Packing of Equal Spheres," *Nature*, **194**, pp.956-958 (1962)

75. G.D. Scott and D.M. Kilgour, "The density of random close packing of spheres," *Brit. J. Appl, Phys.*, **2**, pp. 863-866 (1969)

76. J.D. Bernal, "The Bakerian Lecture, 1962. The Structure of Liquids," *Proceedings of the Royal Society of London. Series A, Mathematical and Physical Science*, **280**, pp.299-322 (1964)

77. J.L. Finney, "Random Packings and the Structure of Simple Liquids. I. The Geometry of Random Close Packing," *Proceedings of the Royal Society of London. Series A, Mathematical and Physical Science*, **319**, pp.479-493 (1970)

78. G.S. CARGILL, "Dense Random Packing of Hard Spheres as a Structural Model for Noncrystalline Metallic Solids," *J. Appl. Phys.*, **41**, pp.2248 (1970)

79. G. Mason, R.H. Beresford, J. Walkley, et al., "General Discussion,", *Discussions of the Faraday Society*, **43**, pp.75-88 (1967)

80. C.H. Bennett, "Serially Deposited Amorphous Aggregates of Hard Spheres," *J. Appl. Phys.,* **43**, pp.2727-2734 (1972)

81. W.M. Visscher and M. Bolsterli, "Random Packing of Equal and Unequal Spheres in Two and Three Dimensions," *Nature*, **239**, pp.504-507 (1972)

82. D.J. Adams and A.J. Matheson, "Computation of Dense Random Packings of Hard Spheres," *J. Chem. Phys.*, **56**, pp.1989-1994 (1972)

83. J.L. Finney, "Fine Structure in Randomly Packed, Dense Clusters of Hard Spheres," *Materials Science and Engineering*, **23**, pp.199-205 (1976)

84. W.S. Jodrey and E.M. Tory, "Computer simulation of close random packing of equal spheres," *Phys. Rev. A*, **32**, pp.2347-2351 (1985)

85. A.S. Clarke and J.D. Wiley, "Numerical simulation of the dense random packing of a binary mixture of hard spheres: Amorphous metals," *Phys. Rev. B*, **35**, pp.7350-7356 (1987)

86. R. Jullien, A. Pavlovitch and P. Meakin, "Random packings of spheres built with sequential models," *J. Phys. A: Math. Gen.*, **25**, pp.4103-4113 (1992)

87. W. Ji and W.R. Martin, "Determination of Chord Length Distributions in Stochastic Media Composed of Dispersed Microspheres," *Trans. Am. Nuc. Soc.,* **96**, pp.467-469 (2007)

88. A. Talamo, W. Gudowski, and F. Venneri, "The burnup capabilities of the Deep Burn Modular Helium Reactor analyzed by the Monte Carlo Continuous Energy Code MCB," *Annals of Nuclear Energy*, **31**, pp. 173-196 (2004)